

University of Central Florida

STARS

Electronic Theses and Dissertations

2008

Effect Of Composition, Morphology And Semiconducting Properties On The Efficiency Of $\text{CuIn}_{1-x}\text{Ga}_x\text{Se}_2\text{-yS}_y$ Thin-film Solar Cells Pre

Sachin Kulkarni
University of Central Florida



Part of the [Materials Science and Engineering Commons](#)

Find similar works at: <https://stars.library.ucf.edu/etd>

University of Central Florida Libraries <http://library.ucf.edu>

This Doctoral Dissertation (Open Access) is brought to you for free and open access by STARS. It has been accepted for inclusion in Electronic Theses and Dissertations by an authorized administrator of STARS. For more information, please contact STARS@ucf.edu.

STARS Citation

Kulkarni, Sachin, "Effect Of Composition, Morphology And Semiconducting Properties On The Efficiency Of $\text{CuIn}_{1-x}\text{Ga}_x\text{Se}_2\text{-yS}_y$ Thin-film Solar Cells Pre" (2008). *Electronic Theses and Dissertations*. 3679.
<https://stars.library.ucf.edu/etd/3679>

EFFECT OF COMPOSITION, MORPHOLOGY AND SEMICONDUCTING
PROPERTIES ON THE EFFICIENCY OF $\text{CuIn}_{1-x}\text{Ga}_x\text{Se}_{2-y}\text{S}_y$ THIN-FILM SOLAR
CELLS PREPARED BY RAPID THERMAL PROCESSING

by

SACHIN S. KULKARNI
B.S. University of Pune, 1998
M.S. University of Central Florida, 2003

A dissertation submitted in partial fulfillment of the requirements
for the degree of Doctor of Philosophy
in the Department of Mechanical Materials and Aerospace Engineering
in the College of Engineering and Computer Science
at the University of Central Florida
Orlando, Florida

Fall Term
2008

Major Professor: Neelkanth G. Dhere

© 2008 Sachin S. Kulkarni

ABSTRACT

A rapid thermal processing (RTP) reactor for the preparation of graded $\text{CuIn}_{1-x}\text{Ga}_x\text{Se}_{2-y}\text{S}_y$ (CIGSeS) thin-film solar cells has been designed, assembled and is being used at the Photovoltaic Materials Laboratory of the Florida Solar Energy Center. CIGSeS films having the optimum composition, morphology, and semiconducting properties were prepared using RTP. Initially films having various Cu/(In+Ga) ratios were prepared. In the next step selenium incorporation in these films was optimized, followed by sulfur incorporation in the surface to increase the bandgap at the surface. The compositional gradient of sulfur was fine-tuned so as to increase the conversion efficiency. Materials properties of these films were characterized by optical microscopy, SEM, AFM, EDS, XRD, GIXRD, AES, and EPMA. The completed cells were extensively studied by electrical characterization. Current-voltage (I-V), external and internal quantum efficiency (EQE and IQE), capacitance-voltage (C-V), and light beam induced current (LBIC) analysis were carried out. Current Density (J)-Voltage (V) curves were obtained at different temperatures. The temperature dependence of the open circuit voltage and fill factor has been estimated. The bandgap value calculated from the intercept of the linear extrapolation was $\sim 1.1\text{-}1.2$ eV. Capacitance-voltage analysis gave a carrier density of $\sim 4.0 \times 10^{15} \text{ cm}^{-3}$. Semiconductor properties analysis of $\text{CuIn}_{1-x}\text{Ga}_x\text{Se}_{2-y}\text{S}_y$ (CIGSeS) thin-film solar cells has been carried out. The values of various PV parameters determined using this analysis were as follows: shunt resistance (R_p) of $\sim 510 \text{ } \Omega\text{-cm}^2$ under illumination and $\sim 1300 \text{ } \Omega\text{-cm}^2$ in dark, series resistance (R_s) of $\sim 0.8 \text{ } \Omega\text{-cm}^2$ under illumination and $\sim 1.7 \text{ } \Omega\text{-cm}^2$ in dark, diode quality factor (A) of 1.87, and reverse

saturation current density (J_0) of $1.5 \times 10^{-7} \text{A cm}^{-2}$. The efficiency of 12.78% obtained during this research is the highest efficiency obtained by any University or National Lab for copper chalcopyrite solar cells prepared by RTP.

CIGS2 cells have a better match to the solar spectrum due to their comparatively higher band-gap as compared to CIGS cells. However, they are presently limited to efficiencies below 13% which is considerably lower than that of CIGS cells of 19.9%. One of the reasons for this lower efficiency is the conduction band offset between the CIGS2 absorber layer and the CdS heterojunction partner layer. The band offset value between CIGS2 and CdS was estimated by a combination of ultraviolet photoelectron spectroscopy (UPS) and Inverse Photoemission Spectroscopy (IPES) to be -0.45 eV, i.e. a cliff is present between these two layers, enhancing the recombination at the junction, this limits the efficiency of CIGS2 wide-gap chalcopyrite solar cells.

ACKNOWLEDGMENTS

I would like to take this opportunity to express my deepest gratitude towards Dr. Neelkanth G. Dhere, for giving me this opportunity to work on the exciting topic of research and development of CIGSeS solar cells. I enjoyed working under his supervision and appreciate his constant guidance and encouragement. I would like to thank Dr. C. Suryanarayana, Dr. Aravinda Kar, Dr. Helge Heinrich, and Dr. Clemens Heske for serving on my final examination committee and for their invaluable suggestions. This research work was supported by National Renewable Energy Laboratory (NREL). I would like to thank the following people for their assistance during this research: Dr. Helio Moutinho, Bobby To, Keith Emery from National Renewable Energy Laboratory. Special words of thanks go to my colleagues Mr. Shirish Pethe, Mr. Vinay Hadagali, Mr. Parag Vasekar, Mr. Bhaskar Kumar, Mr. Ashwani Kaul, Ms. Jyoti Shirolkar, Mr. Upendra Avachat, Mr. Dhaval Shah, and all other people at the Florida Solar Energy Center (FSEC), my senior colleagues Dr. Anant Jahagirdar, Dr. Ankur Kadam, and my earlier lab mates Mr. Mandar B. Pandit, Mr. Sanjay Chavan, Mr. Vivek S. Gade, Mr. Sachin M. Bet, Mr. Anil U. Pai and my friends Dr. Sameer A. Deshpande, Dr. Chandrasen R. Rathod, Dr. Vinu Balakrishnan and others at the University of Central Florida, Mr. Ganzlym Koshiyev and Dr. Jim Sites at the Colorado State University for carrying out cell measurement and analysis, Dr. Clovis Linkous earlier at FSEC for his guidance and help during the research. I would like to acknowledge constant encouragement, support and love from late Dr. Mrs. Sucharita N. Dhere. I have enjoyed working at PV Materials Laboratory of the Florida Solar Energy Center. Finally I would

like to thank my parents, my wife Asawari and in-laws and sister Smita for their love, understanding and support.

TABLE OF CONTENTS

LIST OF FIGURES	x
LIST OF TABLES	xiv
LIST OF ACRONYMS/ABBREVIATIONS	xv
CHAPTER 1 INTRODUCTION	1
1.1 Overview of photovoltaics.....	3
1.2 Basics and operation of a solar cell	5
1.3 Physics of Solar cells	6
1.3.1 Band structure in semiconductors.....	7
1.3.2 P-N Junction (Homojunction).....	14
1.3.3 P-N Junction (Heterojunction).....	18
1.3.4 Current –voltage relationship.....	21
1.3.5 Device parameters and quantum efficiency characteristics	27
CHAPTER 2 CIGS THIN-FILM SOLAR CELLS MATERIALS REVIEW	31
2.1 Thin film solar cells:.....	31
2.2 Copper Indium Gallium Diselenide ($\text{CuIn}_{1-x}\text{Ga}_x\text{Se}_2$).....	34
2.2.1 Crystal Structure	37
2.2.2 Phase diagram	39
2.2.3 Intrinsic defect doping of CIGS.....	42
2.2.4 Microstructure of CIGS thin-films.....	44
2.2.5 Bandgap engineering by Ga addition and sulfurization.....	48
2.2.6 Effect of Na addition.....	49

2.3 Heterojunction Partner layer – Cadmium sulfide (CdS).....	51
2.4 Transparent conducting oxide window bilayer– intrinsic ZnO and Zinc oxide doped with aluminum (ZnO:Al).....	52
2.5 Rapid Thermal Processing.....	54
CHAPTER 3 EXPERIMENTAL TECHNIQUE.....	59
3.1 Rapid Thermal Processing (RTP).....	59
3.1.1 Rapid Thermal Processing set-up	59
3.1.2 Flange fabrication	62
3.1.3 Vacuum and gas filling.....	62
3.1.4 Temperature measurements and finalizing RTP ramp-up cycle.....	62
3.1.5 Temperature uniformity during RTP run.....	64
3.2 CIGSeS Solar cell preparation by RTP	65
3.2.1 NaF sequence.....	65
3.2.2 Deposition of Copper gallium and indium metallic precursors.....	65
3.2.3 Optimization of selenium quantity.....	65
3.2.4 CdS deposition.....	66
3.2.5 Front contact bilayer deposition.....	67
3.2.6 Antireflection coating process	68
3.3 CIGSeS thin film solar cells testing and characterization	68
3.3.1 I-V testing	68
3.3.2 Materials and Electrical Characterization.....	69
3.3.3 Diode parameters analysis	69
3.4 Experimental work for CIGS2 cells band-offset measurement.....	70

CHAPTER 4 RESULTS AND DISCUSSION.....	72
4.1 Preparation of CIGSeS thin films of the required composition and semiconducting properties.	72
4.1.1 Deposition of DC magnetron sputtered copper-gallium and indium metallic precursor films having required thickness and Cu/(In+Ga) ratio	72
4.1.2 Device quality CIGS film formation by RTP	72
4.1.3 Sulfur incorporation in CIGS films by RTP to improve the semiconducting properties and device performance.	79
4.1.4 Preparation of graded CIGSeS absorber films by selenization/sulfurization in RTP.	82
4.1.5 Fine tuning the graded CIGSeS absorber film properties for improving the optoelectronic device performance	93
4.2 Electrical characterization of CIGSeS thin films.....	102
4.3 Performance analysis based on Semiconductor Properties:	115
4.4 CIGS2 solar cells band-offset measurements	118
4.4.1 AES Analysis.....	120
4.4.2 X-ray Photoelectron Spectroscopy (XPS) analysis using Mg K _α radiation...	122
4.4.3 Band offset measurements	124
CHAPTER 5 SUMMARY AND CONCLUSIONS.....	127
REFERENCES	130

LIST OF FIGURES

Figure 1: Band structure, filled energy levels form valence band while the allowed unfilled energy levels form the conduction band.....	9
Figure 2: Carrier occupancy in intrinsic semiconductor.....	12
Figure 3: Electrons occupancy in n-type semiconductor.....	13
Figure 4: Holes occupancy in p-type semiconductor.....	13
Figure 5: Built in potential when n and p type semiconductor are brought in intimate contact.....	16
Figure 6: Heterojunction band diagram of ZnO/CdS/CIGS thin-film solar cell	18
Figure 7: Distribution of excess minority carriers in forward bias condition.....	22
Figure 8: I-V characteristic of solar cell in dark and under illumination drawn in forth quadrant.....	25
Figure 9: (a) Effect of series resistance (R_s) on I-V curve (b) Effect of shunt resistance (R_p) on I-V curve.	26
Figure 10: External quantum efficiency curve and involved loss mechanisms.....	30
Figure 11: Dependence of the absorption coefficient on photon energy	31
Figure 12: (a) CuInSe ₂ chalcopyrite structure showing the (112) plane (b) Binary equivalent ZnS crystal structure.....	38
Figure 13: Ternary elemental composition diagram of Cu-In-Se [45].	41
Figure 14: Pseudo-binary phase diagram along the tie line between Cu ₂ Se and In ₂ Se ₃ represented in terms of Cu atomic % [45].	41
Figure 15: Pseudo-binary phase diagram along the tie line between Cu ₂ Se and In ₂ Se ₃ showing the α phase region widening due to Ga and Na addition.....	50

Figure 16: Generic RTP system.....	55
Figure 17: RTP System Configuration	60
Figure 18: RTP Schematic	60
Figure 19: RTP Setup.....	61
Figure 20: RTP setup during actual run.....	61
Figure 21: Chemical Bath Deposition setup	67
Figure 22: EDS data of CIGS film.....	73
Figure 23: EDS spectra of selenium poor CIGS sample.....	75
Figure 24: SEM of selenium poor CIGS film.....	75
Figure 25: SEM of selenium poor CIGS film.....	76
Figure 26: EDS spectra of CIGS film.....	77
Figure 27: EDS spectra of CIGS film.....	78
Figure 28: XRD pattern of CIGS	78
Figure 29: I-V characteristics for CIGSeS solar cell processed by RTP	80
Figure 30: AES depth profile of CIGSeS film.....	81
Figure 31: XRD pattern of CIGS showing (112) peak at 2θ angle 27.44 degrees.....	82
Figure 32: SEM image of a near-stoichiometric, KCN etched CIGSeS thin film at 5500X	84
Figure 33: Cross sectional SEM image of a near stoichiometric, etched CIGSeS thin film at 16000X.....	84
Figure 34: AFM three dimensional profile of CIGSeS sample fabricated by RTP.	85
Figure 35: AFM surface image of the surface of CIGSeS sample fabricated by RTP.	85
Figure 36: Current-Voltage characteristics of CIGSeS solar cell prepared by RTP.....	86

Figure 37: IV Characteristics of cell 10E#1	87
Figure 38: QE analysis of cell 10E	88
Figure 39: IV Characteristics of cell 14B#3	90
Figure 40: QE analysis of cell 14B.....	91
Figure 41: AES depth profile of near-stoichiometric, etched CIGSeS thin film.....	91
Figure 42: EDS spectra of CIGSeS thin film surface at 20KV.....	94
Figure 43: AES depth profile of a CIGSeS film.....	95
Figure 44: XRD of selenized/sulfurized film.....	96
Figure 45: XRD of selenized (CIGS) film.....	96
Figure 46: XRD pattern of CIGSeS showing (112) peak at 2θ angle 26.94 degrees.....	98
Figure 47: XRD pattern of CIGSeS showing (112) peak at 2θ angle 26.94 degrees.....	98
Figure 48: IV Characteristics of cell 12E	99
Figure 49: QE analysis of cell 12E	99
Figure 50: External QE analysis	102
Figure 51: C-V Plot for RTP 12E	103
Figure 52: LBIC photoresponse map of non-shunted cell: RTP 12E-2.....	105
Figure 53: LBIC photoresponse map of shunted cell: RTP 12E-7	105
Figure 54: LBIC photoresponse map of non-shunted cell: RTP 12E-2.....	106
Figure 55: Dark and light JV characteristics.....	107
Figure 56: Temperature scan	108
Figure 57: Dependence of the open circuit voltage on temperature	108
Figure 58: External Quantum efficiency –solid line, reflection – dashed line	109
Figure 59: Dependence of the fill factor (FF) on temperature.....	110

Figure 60: Back contact barrier height for cells prepared by RTP	111
Figure 61: Semi log version of Back contact barrier height for cells prepared by RTP.	112
Figure 62: Capacitance voltage measurement and analysis.....	113
Figure 63: Fermi level relative to the valence band as function of distance from the p-n junction	114
Figure 64: Schematic band diagram of CIGSeS thin-film solar cell	114
Figure 65: Variation of light and dark current densities with voltage	116
Figure 66: dJ/dV versus voltage characteristics.....	117
Figure 67: Variation of dV/dJ with $1/[J+J_{sc}]$	117
Figure 68: Variation of diode quality factor, A and reverse saturation current density, J_0 with the dark current density, J	118
Figure 69: Surface survey showing presence of Cd, S, Mo, C and O.	120
Figure 70: Cadmium depth profile by AES.	121
Figure 71: Variation of indium and gallium along the depth.....	121
Figure 72: C and K peaks for varied thickness of CdS.....	123
Figure 73: Schematic diagram of the band alignment at the CdS/CIGS2 interface.	126

LIST OF TABLES

Table 1: Inks colors and temperatures	63
Table 2: Device parameters for the cell processed by RTP	80
Table 3: I-V data of CIGSeS absorber from RTP process.....	86
Table 4: Improvement in current-voltage characteristics for CIGSeS thin-film solar cells	101

LIST OF ACRONYMS/ABBREVIATIONS

ACRONYM	Definition of Acronym
AES	Auger Electron Spectroscopy
$^{\circ}\text{C}$	Degree Celsius
CIS	Copper indium diselenide (CuInSe_2)
CIGS	Copper indium gallium diselenide ($\text{CuIn}_{1-x}\text{Ga}_x\text{Se}_2$)
CIGSeS	Copper indium gallium selenide sulfide ($\text{CuIn}_{1-x}\text{Ga}_x\text{Se}_{2-y}\text{S}_y$)
CIGS2	Copper indium gallium disulfide
CdS	Cadmium sulfide
Cu	Copper
EDS	Energy Dispersive Spectroscopy
EPMA	Electron Probe Micro Analysis
eV	electron volts
FCC	Face centered cubic
FF	Fill Factor
Ga	Gallium
In	indium
i:ZnO	intrinsic zinc oxide
J_{sc}	Short circuit current
kV	kilo volts
Mo	molybdenum
nm	nanometer (10^{-9} meter)

R_p	Shunt resistance
R_s	Series resistance
S	Sulfur
Se	Selenium
SEM	Scanning Electron Microscopy
SLG	Sodalime glass
V_{oc}	Open circuit voltage
X	times
XRD	X-ray diffraction
ZnO:Al	Aluminum doped zinc oxide
ZnS	zinc sulfide
μm	micrometer (10^{-6} meter)
η	Photovoltaic conversion efficiency

CHAPTER 1 INTRODUCTION

Photosynthesis utilizes sunlight to biochemically fix carbon dioxide in the growth of plants. However, there are other ways in which sunlight can interact with matter, from simply heating it to releasing electrons from its atomic structure. When light of sufficient energy is absorbed in certain class of materials known as semiconductors, it can create electron-hole pairs. These electron hole pairs are separated in a solar cell. The electrons, seeking charge neutrality, travel through external circuit and do some useful work for us. This phenomenon is known as photovoltaics.

The purpose of this chapter is to introduce the concept of photovoltaics, discuss the underlying physics. Purpose of the second chapter is to review the present status of thin-film photovoltaics. Photovoltaics (PV), direct conversion of sunlight into electricity- is a solar technology with the potential to supply essentially all the energy requirement. Its first uses have been small and remote, as remote as the outer space, however, now PV is becoming more and more common on Earth as PV costs are plummeting. PV is now being recognized as the preferred method of producing electricity [1].

PV depends on solar cells, which are layered devices designed to turn sunlight into electricity. Leave them outside, and they will make electricity as long as the sun shines. Solar cells have been around since the 1950s; however, the first rush of enthusiasm for developing them for energy conversion on large scale occurred with the oil crisis of the mid-1970s. Public interest in PV soared and government programs began. Since then PV has matured and is now on the verge of being a major contributor to world electricity.

The principles behind PV are not a recent discovery. The French scientist Edmund Becquerel discovered the PV effect in 1839. He experimented by placing two electrodes in a beaker full of fluid. A spontaneous current flowed when the beaker was exposed to sunlight. This current may have seemed mysterious to him at that time. In fact, as scientists know now, PV is a complex, quantum-mechanical phenomenon. PV languished while the theoretical framework for explaining it was developed. For much of the 19th century, the PV effect was almost ignored. In 1873, effect of light sensitivity of selenium was discovered that became the basis of selenium light meters for photography. However, these selenium cells were not very effective in converting light into electricity. The best they could do was to transform ~1% of the incoming sunlight into useable electricity. This fractional amount, called the cells efficiency was far too low to be economical, considering manufacturing cost of the cell [1].

In Bell labs during 1950s ~4% efficient silicon solar cells were developed, giving rise to development efforts since then. The next significant influence on the evolution of PV was the energy crisis of the 1970s. After this the public interest in PV was also very high. Sometimes, high public expectations have actually helped PV triggering greater efforts to be made, but unrealistic expectations have also hurt PV, when the enthusiasm has been replaced by disappointment. In early days solar cell manufacturing was born out of the need to supply the space program [1].

The world's energy requirement is continually rising. This challenge can be met only by economical processes. With concerns expressed over the lasting of oil, renewable energy sources are attracting great attention. Among the available renewable energy sources, photovoltaics show high potential to meet this challenge. The main goal for the

photovoltaic industry is to reduce the cost of PV systems to below \$1/peak watt so as to make the technology economically viable and widely acceptable. Keeping this goal in mind the research activities are focused on developing highly efficient materials capable of being produced through an economical process. $\text{CuIn}_{1-x}\text{Ga}_x\text{Se}_{2-y}\text{S}_y$ is one such material that is highly efficient and can be deposited as thin-films on large areas. Sputtering is the technique capable of providing high production rates and high yield. The research presented here is a small step towards attaining the long-term goal of producing terrawatt hour energy level by photovoltaics. All the experiments were carried out on substrate size of 10 cm x 10 cm which could very well form a mini-module. Working on large-area substrates bridges the gap between the laboratory and the industrial results. The problems and their remedies in the laboratory settings would be directly applicable to the industrial shop floor issues. Before going into the experimental and the technical discussion related to the preparation of CIGSeS thin-film solar cell a brief introduction to the physics of solar cells is given. Chapter one starts with developing an understanding for bandgap formation and goes up to the current generation using p-n junction devices. Chapter 2 presents fundamental understanding of the material that goes in to form a complete CIGSeS/CdS thin-film solar cell. Chapter three presents the experimental work, for the preparation of CIGSeS thin-film solar cells by rapid thermal processing. In chapter four, results and discussions are presented; followed by summary and conclusions in chapter five.

1.1 Overview of photovoltaics

Requirements for the ideal solar cell material are:

1. Bandgap between 1.1 and 1.7 eV.

2. Direct band structure.
3. Consisting of readily available, non toxic materials.
4. Easy, reproducible deposition technique, suitable for large area production.
5. Good photovoltaic conversion efficiency.
6. Long-term stability.

At present silicon is main choice as the material for solar cells and will continue to be so in the near future. At present, silicon solar cells and modules do have ~90% share of the total PV cell and module market. Solar cell technology can be divided into two categories: conventional silicon i.e. crystalline silicon, and thin-films. Crystalline silicon (c-Si) solar cells are also known as first generation solar cell technology. Crystalline silicon is an indirect bandgap semiconductor with a bandgap of 1.12 eV. Being an indirect bandgap semiconductor, a minimum thickness of 100 μm is required for the maximum absorption of the solar spectrum. Si technology flourished very fast since considerable information was available from the microelectronic industry. Silica is available in vast amounts, however, the process to produce device-quality grade Si is costly. Laboratory efficiency of 24.7% [2] has been achieved so far on a small area cell while the highest reported module efficiency has been 22.7%. Present-day crystalline-Si technology is approaching its lower limit in terms of production costs. However, to meet the energy requirement of the future a new technology has to be developed. Thin-film technology with reduced material requirements and high-yield techniques would be a viable option for PV manufacturing. Thin-film solar cells are referred to as second generation solar cells. From the various materials under consideration, only four thin-film technologies namely hydrogenated amorphous silicon (a-Si:H) and polycrystalline

heterojunction systems of CdS/Cu₂S, CdS/CdTe and CdS/CuInSe₂, have entered commercial large scale production. At present, the a-Si:H and CdTe technologies are contributing to the world PV market. Activities in the CdS/Cu₂S stopped at the beginning of the eighties due to stability issues and a-Si:H became the frontrunner in the thin-film technology. The highest potential with regards to cost reduction and high efficiencies is provided by the heterojunction solar cell based on CdTe and CuInSe₂ absorbers. Both materials have proven their potential over the ~35 years of world-wide research and development. The highest reported cell and module efficiencies for CdTe are 16.5% [3] and 10.7 [4] respectively. The highest reported cell and module efficiencies for CuInSe₂ are 19.9% [5] and 13.4 [4] respectively. Third generation solar cells e.g. quantum well and quantum dot solar cells are being studied because of their promise for higher efficiency [6]. They work on the concept of creating multiple bandgaps in a single junction cell. Organic solar cells are another category that is being developed. At present, these cells are not highly efficient. There are also concerns about their reliability and durability. However, when the efficiency and reliability problems are overcome, they could become the cheapest of all the existing technologies.

1.2 Basics and operation of a solar cell

A solar cell is a p-n junction diode capable of producing electricity when light is incident on it. This makes it the most important renewable energy source capable of harvesting the abundantly available sunlight to solve the world energy crisis. Semiconductors of p and n type are obtained by doping with impurities such as boron and phosphorous respectively in silicon or by naturally occurring point defects such as vacancies, interstitials and antisites as in copper indium diselenide thin-film solar cells. The majority carriers in p-

type semiconductor are holes while the majority carriers in n-type semiconductor are electrons. When p and n-type semiconductors are joined together, the free electrons from n-type migrate over the metallurgical junction, recombine with the holes in the p-type semiconductor and a region free of mobile charge carriers called a depletion region is generated.

1.3 Physics of Solar cells

Air mass (AM) is the measure of how absorption in the atmosphere affects the spectral content and intensity of the solar radiation entering the earth. In space the radiation intensity or the solar constant is 1.353 kW/m^2 and is referred to as AM 0. The absorption of the spectrum increases with the increase in the thickness of the atmospheric layer. For the thickness l_0 of the atmosphere, the path length l through the atmosphere for radiation from the sun incident at an angle θ relative to the normal to the earth's surface is given by

$$l = l_0 / \cos \theta,$$

Where, θ = angle of incidence, $\theta = 0$ if sun is exactly overhead.

The ratio l/l_0 is called air mass coefficient. The performance of solar cells is evaluated at AM 1.5 condition corresponding to the solar constant of 1 kW/m^2 . The solar constant on the earth's surface is always lower than that in space due to the spectrum absorption by the atmosphere. This absorption is almost entirely caused by gases of low concentration in the infra red region of the solar spectrum, by water vapor (H_2O), carbon dioxide (CO_2), laughing-gas (N_2O), methane (CH_4), fluorinated hydrocarbon, as well as by dust and by ozone and oxygen in the ultraviolet region of the spectrum. A simple way of representing Air Mass value at different earth locations is given by the simple equation [9],

$$AM = (1+(S/H)^2)^{1/2}$$

Where, S = Length of the shadow cast by an object of height H at that location.

1.3.1 Band structure in semiconductors

An atom of a solid is electrically neutral. The positive charge of a nucleus is compensated by negatively charged electrons. The electrons are acted upon by a Coulomb potential exerted by the nucleus, rendering electrons to possess certain allowed energies. Electron of a free atom can occupy one of the series of energy levels below $E = 0$, given by the approximation [7]

$$E_n = \frac{-Z^2 m_o q^4}{8\epsilon_o^2 h^2 n^2} \dots\dots\dots (1)$$

Where,

q - Charge of electron;

Z – Atomic number;

m_o - mass of free electron;

ϵ_o – permittivity of free space or dielectric constant;

h – Plank’s constant; and

n – Positive integer representing energy levels.

At equilibrium not all the electrons fill the lowest energy level. According to Pauli’s exclusion principle each energy level can have a maximum of two electrons with opposite spins. These energy levels are further compounded in shells governed by quantum numbers given by quantum mechanic theory.

When atoms are isolated from each other the electron in individual atoms occupies the energy level given by equation 1. However, as the atoms start coming close to each other the atomic core of the first atom exerts a force on the electron of the second atom disturbing the potential and consequently the energy levels of the electron. The effect is of prime importance for the highest occupied energy levels that is for valence electrons. According to Pauli's exclusion principle, each energy level, E_n , of an atom contains two electrons. When two similar atoms are brought together the energy level, E_n , cannot accommodate 4 electrons as it violates Pauli's exclusion principle. As a result of this interaction the energy level, E_n , is disturbed and splits into two slightly separated energy levels. As the atoms come closer the perturbation and also the splitting increases. If N numbers of atoms interact then the original energy level E_n is split into N different allowed energy levels accommodating $2N$ electrons. When the atomic spacing equals the crystal lattice spacing, the regions of allowed energy level are typically separated by a forbidden energy gap in which electrons cannot exist.

Henceforth in the discussion the band structure will be represented in single lines indicating valence band maxima and conduction band minima separated by band-gap. In an intrinsic semiconductor at absolute zero temperature, the valence band is completely filled while the conduction band is completely empty. Figure 1 shows schematic of band structure of a semiconductor.

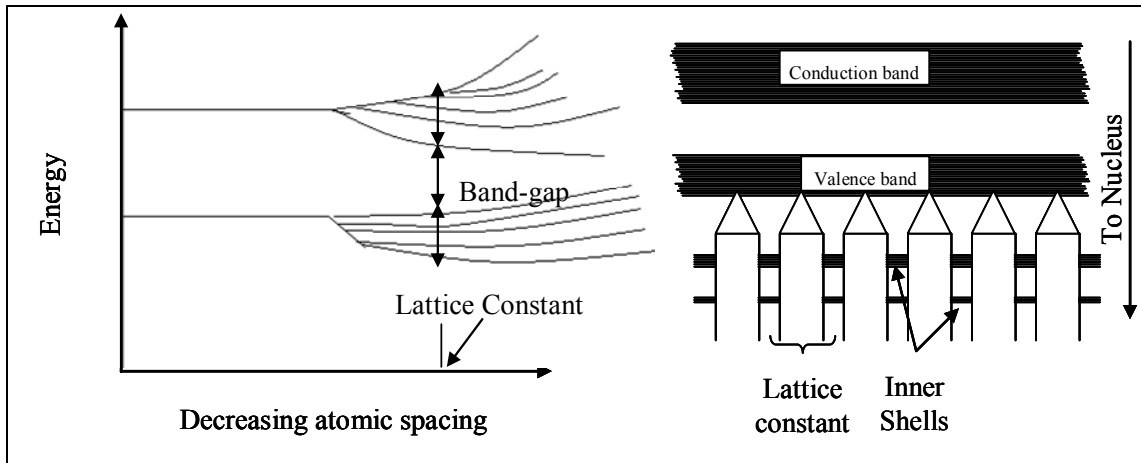


Figure 1: Band structure, filled energy levels form valence band while the allowed unfilled energy levels form the conduction band

As the temperature increases, some of the electrons gain enough energy to jump over the forbidden gap and reach the conduction band. The effect of temperature on the occupancy of electrons in an energy level is given by the Fermi Dirac distribution function given by the equation [7].

$$f(E) = \frac{1}{e^{\frac{E-E_f}{kT}} + 1} \dots\dots\dots (2)$$

Where,

$f(E)$ = Fermi Dirac function determining the probability of electron occupancy at energy level 'E' at temperature T in Kelvin;

k is Boltzmann constant (8.62×10^{-5} eV/K);

E_F is Fermi energy.

It is also defined as the energy level where the probability of charge carrier occupancy is 50 %. At absolute zero temperature Fermi energy is the highest filled energy level. For an

intrinsic semiconductor, the Fermi level is at the center of the forbidden gap. Doping a semiconductor with an n-type impurity results in free electrons that introduce an additional energy level within the forbidden gap close to the conduction band. Addition of phosphorus (donor impurity) in silicon results in an energy level called donor level (E_d) that is 0.045 eV below the conduction band. Thermal energy at room temperature (kT) is equal to 0.026 eV. Due to the Gaussian distribution of energy, several electrons have energies higher than 0.045 eV sufficient to ionize the donors resulting in free electrons donated to the conduction band and ionized impurity level in the forbidden band. Similarly, acceptor impurities are ionized, and create an ionized impurity level in the forbidden band. At high energy levels such that $E - E_F \gg kT$. Due to this $\exp(E - E_F) \gg 1$ i.e. Fermi function tends to Boltzmann function [7].

$$f(E) = e^{-(E-E_f)/kT} \dots\dots\dots (3)$$

The density of allowed states is zero in the forbidden gap while it is non zero in the allowed energy bands. Density of states can be calculated by solving the time-independent Schrödinger equation. All the complexity of the periodic potentials of the component atoms has been incorporated into the effective mass.

The density of states at energy E near the conduction band edge is given by [9].

$$g_c(E) = \frac{m_n^* \sqrt{2m_n^*(E - E_c)}}{\pi^2 h^3} cm^{-3} eV^{-1} \dots\dots\dots (4)$$

Similarly density of states at energy E near the valence band edge is given by [9].

$$g_v(E) = \frac{m_p^* \sqrt{2m_p^*(E_v - E)}}{\pi^2 \hbar^3} cm^{-3} eV^{-1} \dots\dots\dots (5)$$

Where,

m_n^* : Effective mass of electron;

m_p^* : Effective mass of hole;

E_c : Conduction band minima;

E_v : Valence band maxima.

Now, the carrier concentration at any energy level is the product of probability of occupancy and the number of available states. Therefore, electron concentration in the conduction band in the energy increment of dE can be written as [7][7].

$$n_o = \int_{E_c}^{\infty} g_c(E) f(E) dE \dots\dots\dots (6)$$

On substituting with respective equations and solving the integral, to get [7].

$$n_o = N_c e^{(E_f - E_c) / kT} \dots\dots\dots (7)$$

Where,

$$N_c = 2 \left(\frac{2\pi m_n^* kT}{h^2} \right)^{3/2} \dots\dots\dots (8)$$

N_c is a constant at fixed T known as effective density of states in the conduction band.

Similarly, hole concentration in valence band can be calculated by [7][7].

$$p_o = \int_{-\infty}^{E_v} g_v(E)[1 - f(E)]dE \dots\dots\dots (9)$$

$$p_o = N_v e^{(E_v - E_f)/kT} \dots\dots\dots (10)$$

$$N_v = 2 \left(\frac{2\pi m_p^* kT}{h^2} \right)^{3/2} \dots\dots\dots (11)$$

N_v is a constant at fixed T known as effective density of states in the valence band

The entire argument can be schematically represented for an intrinsic, n-type and p-type semiconductor as shown in Figures 2, 3 and 4 respectively.

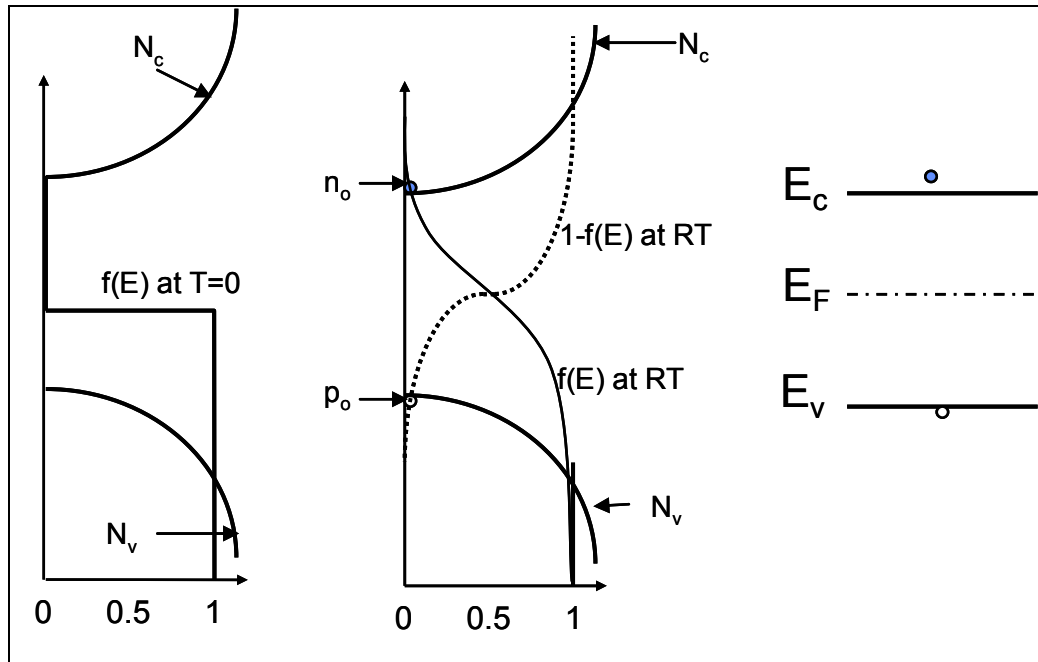


Figure 2: Carrier occupancy in intrinsic semiconductor

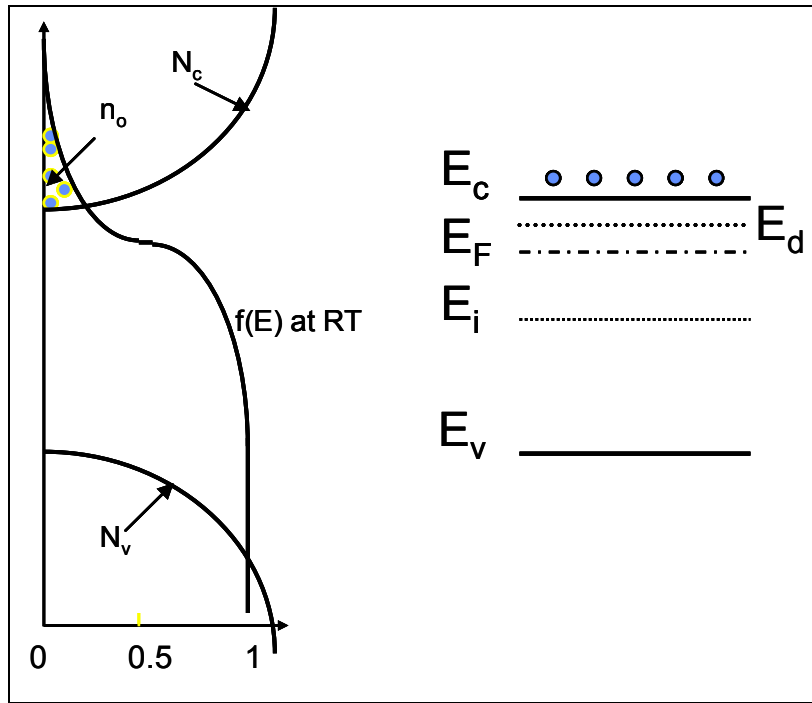


Figure 3: Electrons occupancy in n-type semiconductor

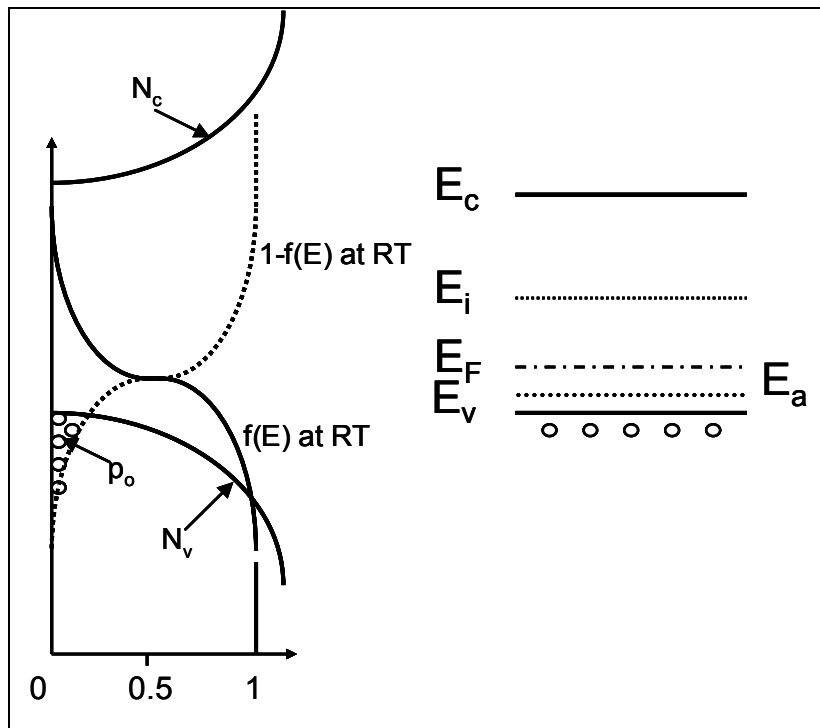


Figure 4: Holes occupancy in p-type semiconductor

1.3.2 P-N Junction (Homojunction)

When a doped n-type region is formed or grown on a p-type region of the same material a junction is formed between them, it is known as a homojunction. The formation of an electric field when p and n type semiconductors are brought together to form a junction is at the heart of operation of a p-n junction. When n-type and p-type semiconductors are brought in intimate contact with each other, the free carriers can move across to the oppositely doped material, leaving behind uncompensated dopant atoms. The positive ions on the n-type semiconductor and negative ions on the p-type semiconductor near the junction result in an electric field built-up resisting the flow of these carriers and a new equilibrium is established. This field creates a potential barrier between the two semiconductors as shown in Figure 5. This region of absence of charge carriers is called depletion region as mentioned earlier. When equilibrium is reached, the magnitude of the field is such that the tendency of electrons to drift from the n-type region into the p-type region is exactly balanced by the tendency of electrons to drift in the opposite direction under the influence of the built-in field. At equilibrium the Fermi level is constant throughout the entire system. For homojunction diodes the magnitude of the potential barrier associated with the built-in field can be found by considering the difference in the Fermi levels of the initially separated materials.

At equilibrium electrons and holes currents are zero. Under this condition, the electric field (E) generated by diffusion of charge carriers is given by the following relation. It can be noted that the electric field is maximum at the junction [9].

$$E = -\frac{kT}{qn} \frac{dn}{dx} \dots\dots\dots (12)$$

Where,

k is the Boltzmann constant;

T is the temperature in Kelvin;

q is the charge of an electron;

n is free electron concentration in equilibrium;

dn/dx is change in electron concentration.

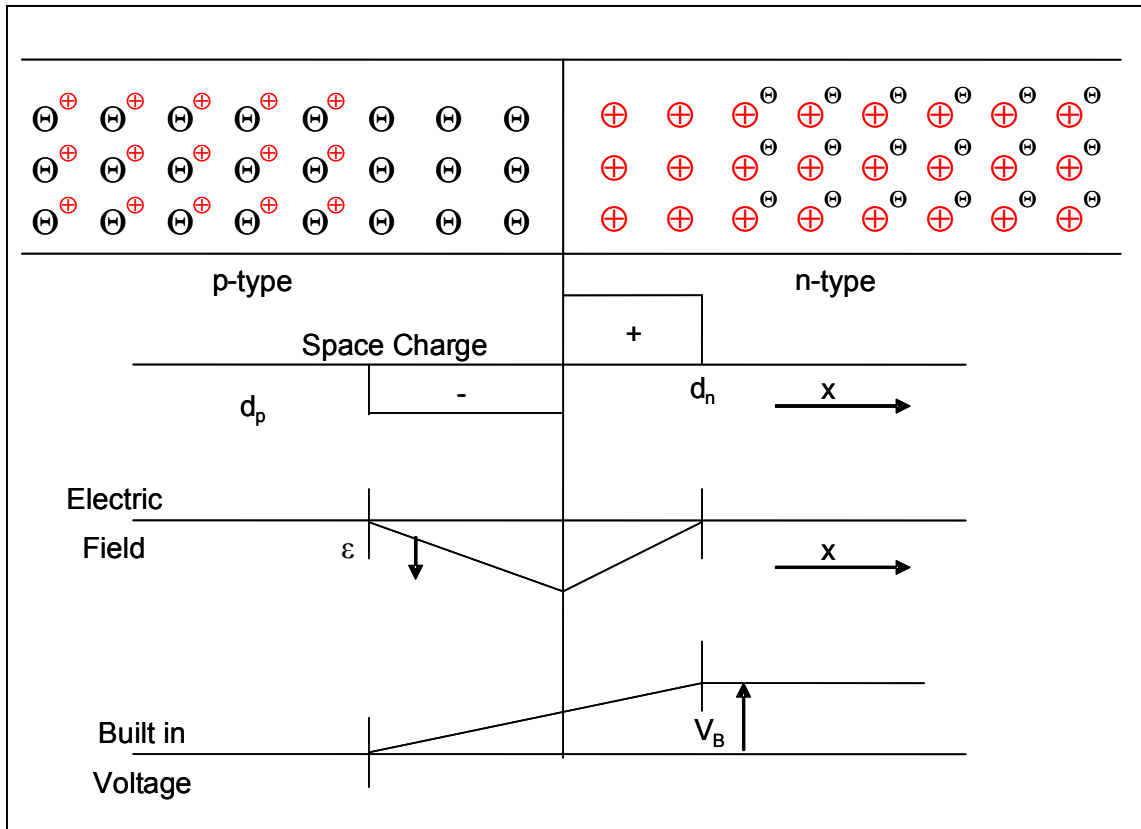


Figure 5: Built in potential when n and p type semiconductor are brought in intimate contact

The built-in voltage can be obtained by integrating the electric field from p-region to n-region [9][9].

$$V_B = \int_{p\text{-side}}^{n\text{-side}} E dx \dots\dots\dots (13)$$

On solving the integral,

$$V_B = \frac{kT}{q} \ln \frac{N_A N_D}{n_i^2} \dots\dots\dots (14)$$

Where,

N_A is acceptor concentration;

N_D is donor concentration;

n_i is intrinsic carrier concentration.

The width of depletion region is determined by impurity concentration and total voltage which is the sum of built-in voltage and applied voltage. At equilibrium the applied bias is zero and so the depletion width depends only on the built-in voltage.

Total depletion width is given by the relation [9].

$$d = d_n + d_p = \sqrt{\frac{2\epsilon_s V_B (N_A + N_D)}{q(N_A N_D)}} \dots\dots\dots (15)$$

Where,

d_n is depletion width in n-type material;

d_p is depletion width in p-type material;

ϵ_s is permittivity of the material.

Under non-equilibrium condition when voltage V is applied across the p-n junction the equation modifies as [9] [10].

$$d = \sqrt{\frac{2\epsilon_s(V_B - V_a)(N_A + N_D)}{q(N_A N_D)}} \dots\dots\dots (16)$$

The depletion width increases with the application of an external voltage (V_a) in reverse biased condition ($-V_a$) while it decreases in forward biased condition ($+V_a$).

1.3.3 P-N Junction (Heterojunction)

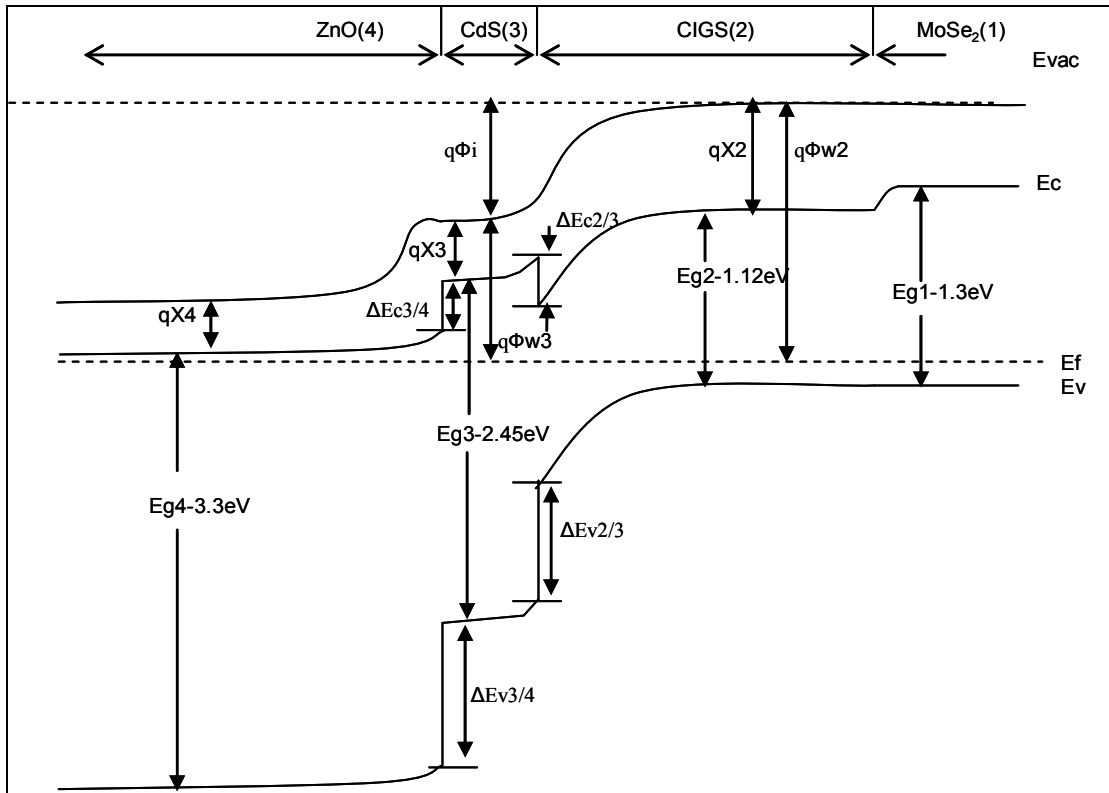


Figure 6: Heterojunction band diagram of ZnO/CdS/CIGS thin-film solar cell

Where,

The numbers 1, 2, 3 and 4 refers to MoSe₂, CIGS, CdS and ZnO respectively.

Eg1, Eg2, Eg3 and Eg4 – Bandgaps

qX2, qX3 and qX4 – electron affinities

$q\Phi_{w2}$, $q\Phi_{w3}$ – work function

$q\Phi_i$ – Built-in potential at p-n junction

$\Delta E_{c2/3}$ – Conduction band offset between CIGS and CdS

$\Delta E_{v2/3}$ –Valence band offset between CIGS and CdS

$\Delta E_{c3/4}$ – Conduction band offset between CdS and ZnO

$\Delta E_{v3/4}$ –Valence band offset between CdS and ZnO

The physics of a solar cell discussed so far was related to homojunction. When a junction is formed between two different semiconductors, it is known as heterojunction. CIGS/CdS is a heterojunction device; hence it is important to understand the additional features involved in the band diagram. To form a heterojunction, two semiconductors of different bandgaps are brought together such as p-type CIGS and n-type CdS as shown in Figure 6. In the case of heterojunction system, along with the bandgap, the electron affinities of the individual semiconductors are different due to the difference in their respective work functions. For vacuum level to remain continuous at the interface, a discontinuity must occur in the conduction band as well as valence band at the interface. The discontinuity in the conduction band at the interface can be written as,

$$\Delta E_{c2/3} = q\chi_2 - q\chi_3$$

Similarly, the discontinuity in the valence band at the interface can be written as

$$\Delta E_{v2/3} = q\Phi_{w2} - q\Phi_{w3}$$

The discontinuities at the interface affect the near-by space-charge regions. In the neutral region of each material away from the interface the separation between the conduction band edge and the Fermi level is determined by doping in that material [7].

$$E_{c3} - E_f = kT \ln \left(\frac{N_{c3}}{N_{D3}} \right) \dots\dots\dots (17)$$

Where, N_{c3} – density of states in conduction band of CdS, N_{D3} – donor dopant density [7[7]

$$E_{c2} - E_f = E_{g2} - (E_f - E_{v2}) = E_{g2} - kT \ln \left(\frac{N_{v2}}{N_{a2}} \right) \dots\dots\dots (18)$$

Where, N_{v2} - density of state in valence band of CIGS, N_{a2} - acceptor dopant density

Therefore, the total difference in the conduction band edge between the neutral regions in the two semiconductors does not depend on electron affinities and is given by [7[7].

$$E_{c2} - E_{c3} = E_{g2} - kT \ln \left(\frac{N_{c3}N_{v2}}{N_{D3}N_{a2}} \right) \dots\dots\dots (19)$$

Now to retain the same value of $E_{c2}-E_{c3}$ between the neutral regions with positive non-zero $\Delta E_{c2/3}$ at the interface, the total bending of the energy bands must increase by $\Delta E_{c2/3}$. The built-in potential also increases with positive $\Delta E_{c2/3}$ as the individual work function Φ_{w2} and Φ_{w3} changes. The greater bending of the energy bands with different

electron affinities implies higher built in potential and hence higher open circuit voltage (V_{oc}).

1.3.4 Current –voltage relationship

A solar cell under no illumination is a simple p-n junction diode. When forward bias is applied to the diode, excess electrons are injected in the p region while excess holes are injected in the n region. This results in a reduction of the potential barrier across the junction making it possible for more charge carriers to cross over to opposite regions and recombine [10[7].

$$n_p = n_{po} e^{qV_a/kT} \dots\dots\dots (20)$$

$$p_n = p_{no} e^{qV_a/kT} \dots\dots\dots (21)$$

Where,

n_p is the injected minority carrier concentration in p region;

n_{po} is the minority carrier concentration in thermal equilibrium at the edge of the depletion region;

p_n is the injected minority carrier concentration in n region;

p_{no} is the minority carrier concentration in at the edge of the thermal equilibrium.

The excess minority carrier concentration decreases exponentially with the distance away from the junction as shown in Figure 7. The decay depends on both the diffusion constant and lifetime [10].

$$\hat{n} = \hat{n}_o e^{-x/\sqrt{D_n\tau_n}} \dots\dots\dots (22)$$

$$\hat{p} = \hat{p}_o e^{-x/\sqrt{D_p\tau_p}} \dots\dots\dots (23)$$

Where,

D_n and D_p are the diffusion constants for electron and hole minority carriers respectively;

τ_n and τ_p are the lifetime of electron and hole minority carriers respectively;

\hat{n} is the injected electron carrier concentration in p-region;

\hat{n}_o is the injected electron carrier concentration at depletion width edge;

\hat{p} is the injected hole carrier concentration in n-region;

\hat{p}_o is the injected hole carrier concentration at depletion width edge as shown in

Figure 7.

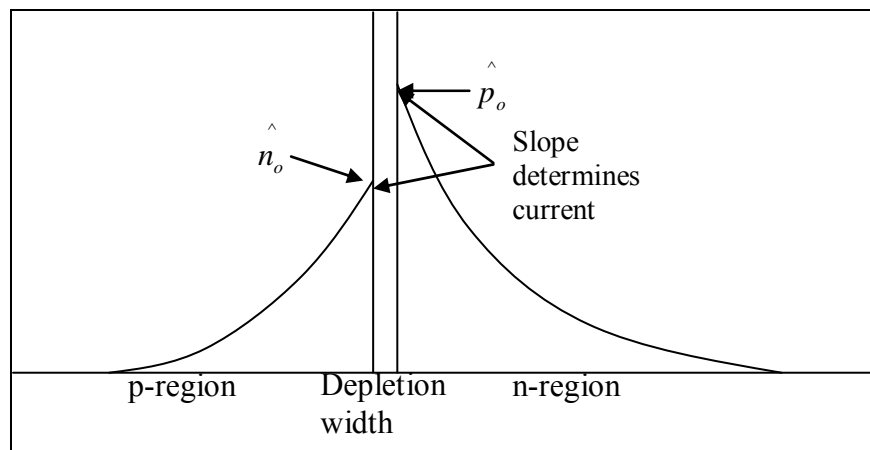


Figure 7: Distribution of excess minority carriers in forward bias condition

The current flowing is sum of the hole and electron currents at any point. However, it is convenient to take the sum at the junction, where the currents are known. The slope of the curve determines the current contribution by each minority charge carrier. The hole current at the junction is given by [10]

$$I_p = qA \sqrt{\frac{D_p}{\tau_p}} \hat{p}_o \dots\dots\dots (24)$$

Where, A is the junction area

The electron current at the junction is given by [10]

$$I_n = qA \sqrt{\frac{D_n}{\tau_n}} \hat{n}_o \dots\dots\dots (25)$$

The total current is the sum of hole and electron currents [10].

$$I = I_p + I_n = qA \left(\sqrt{\frac{D_p}{\tau_p}} \hat{p}_o + \sqrt{\frac{D_n}{\tau_n}} \hat{n}_o \right) \dots\dots\dots (26)$$

It is known that $n_p = n_{po} + \hat{n}_o$ and also $p_n = p_{no} + \hat{p}_o$

$$n_{po} = n_i^2 / N_A \dots\dots\dots (27)$$

$$p_{no} = n_i^2 / N_D \dots\dots\dots (28)$$

Where,

n_i is the intrinsic carrier concentration

Therefore,

$$\hat{n}_o = n_{po} \left(e^{qV_a / kT} - 1 \right) \approx \frac{n_i^2}{N_A} \left(e^{qV_a / kT} - 1 \right) \dots\dots\dots (29)$$

$$\hat{p}_o = p_{no} \left(e^{qV_a / kT} - 1 \right) \approx \frac{n_i^2}{N_D} \left(e^{qV_a / kT} - 1 \right) \dots\dots\dots (30)$$

From equation 19, 20, 26, 27, 28 and 29, the total current can be written as [10]

$$I = qAn_i^2 \left(\sqrt{\frac{D_p}{\tau_p N_D}} + \sqrt{\frac{D_n}{\tau_n N_A}} \right) \left(e^{qV_a / kT} - 1 \right) \dots\dots\dots (31)$$

If the applied voltage is negative i.e. reverse biased condition, a current called reverse saturation current is obtained [8] [10]

$$I_o = -qAn_i^2 \left(\sqrt{\frac{D_p}{\tau_p N_D}} + \sqrt{\frac{D_n}{\tau_n N_A}} \right) \dots\dots\dots (32)$$

From relation 31 and 32,

$$I = I_o \left(e^{qV_a / kT} - 1 \right) \dots\dots\dots (33)$$

Under illuminated conditions there is an extra current due to a photogenerated current;

Therefore, the above equation changes to [10]

$$I = I_o \left(e^{qV_a / kT} - 1 \right) - I_L \dots\dots\dots (34)$$

Where,

I_L (shown as I_{sc}) is photogenerated current shown in Figure 88.

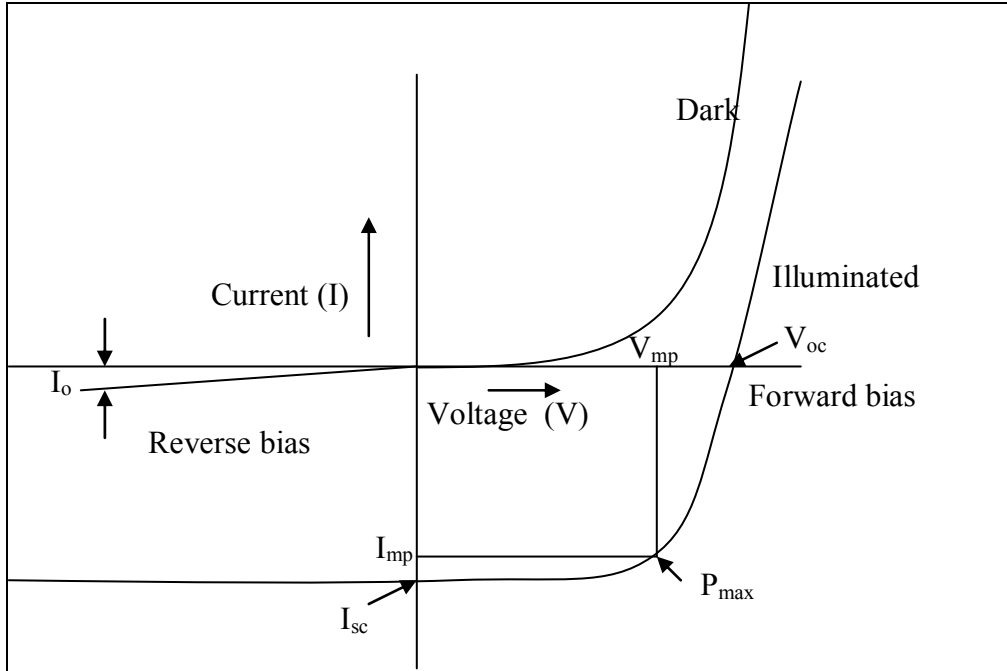
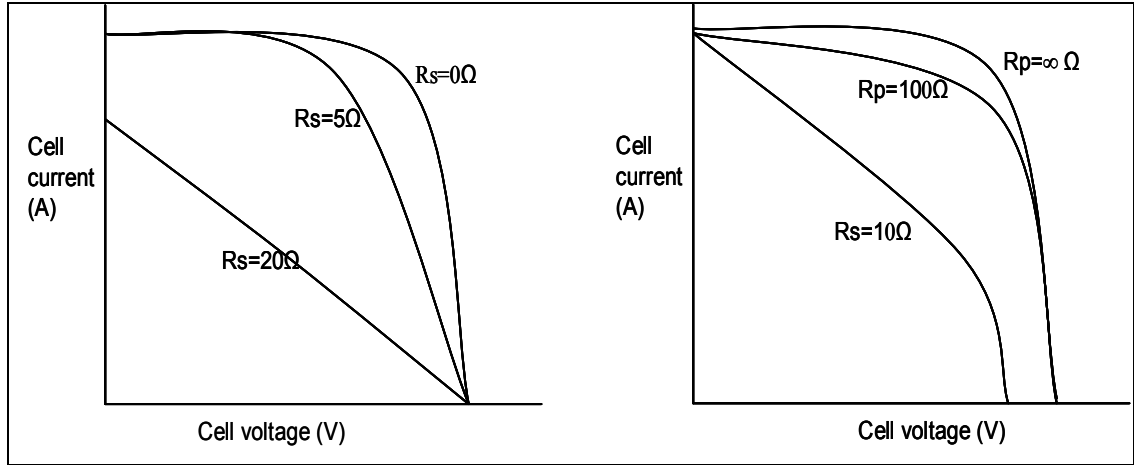


Figure 8: I-V characteristic of solar cell in dark and under illumination drawn in forth quadrant

When light is shone on a cell not connected to the external circuit, the generated free charge carriers flow across the built-in electric field and built up charge on the other side of the cell. The charge build up by free carriers continues to increase till it just balances the built-in field. At this stage the built-in field will not be able to separate charge carriers any more. The corresponding built up potential is called open circuit voltage (V_{oc}) and it is the maximum voltage a cell can provide. It is given by the relation [8]

$$V_{oc} = \frac{kT}{q} \ln\left(\frac{I_L}{I_o} + 1\right) \approx \frac{kT}{q} \ln \frac{I_L}{I_o} \dots\dots\dots (35)$$



(a)

(b)

Figure 9: (a) Effect of series resistance (R_s) on I-V curve (b) Effect of shunt resistance (R_p) on I-V curve.

With series and shunt resistance becoming effective the nature of the I-V curve changes as shown in the Figure 9. The modified I-V relationship is given by equation 36. Therefore, the data obtained from the I-V curve can be used to calculate series and shunt resistances [8].

$$\ln \left(I + \frac{I_L}{I_o} - \frac{V - IR_s}{I_o R_p} + 1 \right) = \frac{q(V - IR_s)}{kT} \dots\dots\dots 36$$

As the resistance reduces more current will flow and the voltage will reduce. At short circuit condition the current is maximum and the voltage is zero. This value of current is called short circuit current (I_{sc}) generally represented as short circuit current density (J_{sc}) and it is the maximum current density a cell can produce.

At the open circuit voltage (V_{oc}) and short circuit current density (J_{sc}), the power is zero. The maximum power is the optimum combination of voltage and current. Fill Factor (FF) is another important factor in efficiency measurement of solar cell. The fill factor is

defined as the ratio of peak power to the product of open circuit voltage and short circuit current density. It represents the squareness of the I-V curve at the maximum power point and is given by equation 37 [9]. A good cell should have a fill factor over 70%.

$$FF = \frac{V_{mp} I_{mp}}{V_{oc} I_{sc}} \dots\dots\dots 37$$

Where,

V_{mp} and I_{mp} are the voltage and current of the maximum power point Figure 8.

The photovoltaic conversion efficiency of a solar cell is given by the relation [9]

$$\eta = \frac{V_{oc} I_{sc} FF}{P_{in}} \dots\dots\dots 38$$

Where,

P_{in} is the incident power taken as 100 mW/cm² for a laboratory measurement corresponding to the AM 1.5 solar spectrum.

1.3.5 Device parameters and quantum efficiency characteristics

The device parameters on the basis of which an efficiency of a cell is defined are, short circuit current density (J_{sc}), open circuit voltage (V_{oc}) and fill factor (FF). These values solely depend on the material used and its quality. The factors on which short circuit current density (J_{sc}) depend are; 1) light absorption; it is the ability of a semiconductor to absorb sunlight, normally referred to as absorption coefficient (α). This value depends on the type of bandgap of the semiconductor. A direct bandgap semiconductor such as $CuIn_{1-x}Ga_xSe_2$ (CIGS) can effectively absorb 90% of the light within 1 μm thickness ($\alpha \sim 10^5$ cm). An indirect bandgap semiconductor such as silicon requires additional energy

provided by phonon in the form of lattice vibration to transfer an electron from the valence band to the conduction band, hence its $\alpha \sim 10^{-2}$ cm. Therefore, to effectively absorb 90% of the light, a thicker layer is required (~ 100 μm). 2) Drift and diffusion; Absorption of the photons depends on the direct/indirect bandgap of the material and the photon energy. Higher energy photons are absorbed near the surface while the lower energy photons are absorbed away from the surface and hence away from the electric field. Almost every electron-hole pair generated within the electric field region could be separated and can contribute to the current. The field-driven movement of the free carriers within the built in field is called drift. The charge carriers generated away from the electric field do not lose their energy instantly and fall back into the bound state. The amount of time for which they remain active is called their lifetime. If the charge carrier diffuses to the built-in field within the lifetime it can be propelled to the opposite side and can contribute to the current. The average distance a charge carrier can travel before getting recombined is called diffusion length. The diffusion length depends on the crystal quality of the material. Defects such as impurities resulting in interstitials or lattice strain, vacancies and grain boundaries can reduce the diffusion length. The open circuit voltage (V_{oc}) depends on the built-in voltage of the device. Recombination centers located within the field greatly reduce the open circuit voltage (V_{oc}). For a highly efficient cell the current lost by recombination should be minimum i.e. the shunt resistance should be as high as possible. For ideal cell the shunt resistance is infinity. In contrast to the recombination centers in the bulk, the recombination centers within the built-in electric field result in continuous recombination of charge carriers as a result of which the open circuit voltage (V_{oc}) is reduced [11]. Another mechanism of current loss and mostly the

voltage loss is series resistance. Series resistance losses occur because free carriers separated by the built-in fields have to travel some distance to reach a metal contact. At the back the cell, this distance may be purely vertical and quite small, may be less than a micron. But the front contact is usually a grid to avoid shadowing. To reach the grid fingers, carriers must move sideways along distances of several millimeters and in the process they can lose substantial energy to resistance. This resistance can be reduced by making the top layer from a semiconductor that is transparent to the visible spectrum as well as having a high density of free carriers i.e. a degenerate transparent conducting semiconductor. There are several semiconductors that can serve this purpose i.e. indium tin oxide (ITO) or aluminum doped zinc oxide (ZnO:Al). Such semiconductors are known as transparent conducting oxides as they are transparent to most of the visible spectrum and highly conducting due to their degeneracy.

All the factors mentioned above can be measured by current-voltage (I-V) and quantum efficiency (QE) measurements. QE is the measure of the effectiveness of a cell in converting light of various energies into electricity. If a cell shows very fine response to high-energy photons and poor response to low-energy photons in QE measurements then it means the charge carriers generated within the built-in electric field are effectively separated while the charge carriers generated away from the field in the bulk are undergoing recombination [11]. This indicates that the diffusion length has to be improved by improving the crystal quality of the absorber or the defects need to be passivated through some mechanism. QE measurements showing poor response to high energy and good response for lower energy indicates the presence of a layer opaque to high energies and transparent to low energies or reflects high-energy light preferentially.

Such a layer could be removed or altered to improve the performance. The cells with a mediocre QE response indicate several problems. The obvious ones are the losses due to the reflection of the incident spectrum or large recombination losses at the junction that are removing a large fraction of electrons independent of the energy of their original photons [11]. Quantum efficiency analysis can be carried out in two ways, external quantum efficiency when the light reflected from the cell surface is taken into account and internal quantum efficiency when the light reflected from the cell surface is not taken into account. Figure 10 shows the external quantum efficiency curve of a CIGS/ZnS(O,OH) cell. Different regions responsible for reducing the quantum efficiency and current density are shown.

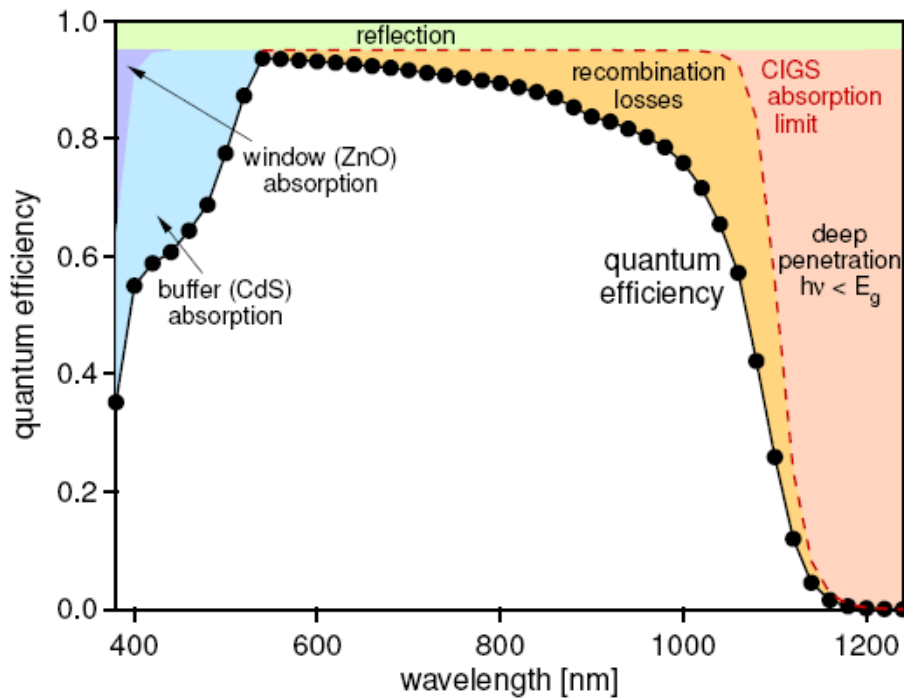


Figure 10: External quantum efficiency curve and involved loss mechanisms

CHAPTER 2 CIGS THIN-FILM SOLAR CELLS MATERIALS REVIEW

2.1 Thin film solar cells:

Thin-film solar cells having ~2-4 micron thick layers for light absorption instead of crystalline silicon having thickness in the range of ~180-300 microns are being developed with the aim of lowering the cost of PV manufacturing as compared to crystalline silicon. The thickness can be reduced to such an extent mainly because the light absorbing semiconductor has a direct bandgap, as opposed to silicon, which is an indirect bandgap semiconductor (Figure 11).

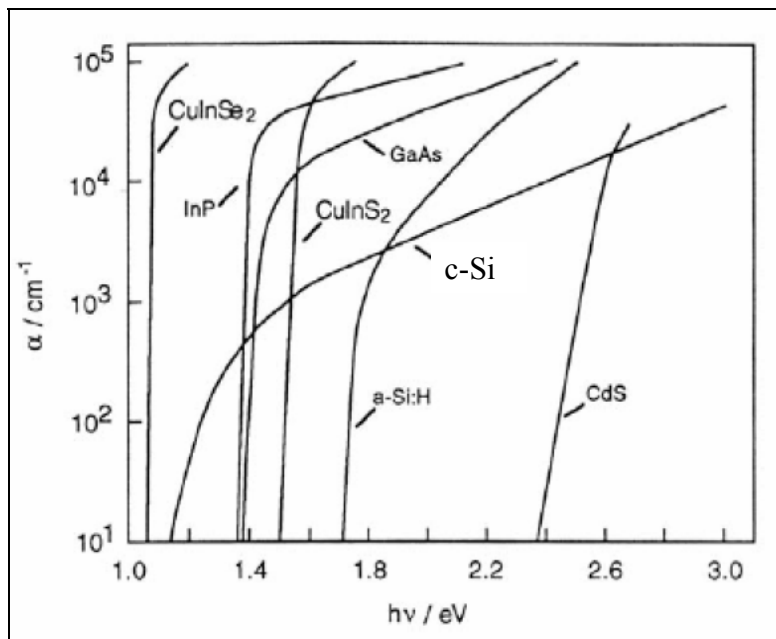


Figure 11: Dependence of the absorption coefficient on photon energy

The main features for the cost reduction are

1. Lower thickness requirement of active light absorbing semiconductor layers reduces material cost. Also the purity of the materials required is not as high as that of crystalline silicon. Relatively higher purity is essential in silicon as

electron-hole pairs are generated away from the built in electric field, and need to travel comparatively long distance; if impurities are present they reduce the diffusion length of these charge carriers. As opposed to this, in thin-film solar cells, most of the electron-hole pairs are generated in the vicinity of built-in electric field, and separated by drift rather than diffusion. Hence, relatively low purity materials can be used. [11]

2. As the layers are thin, processing can be faster reducing the capital cost. [11]
3. Processing of larger areas of the order of 1 m^2 is possible, instead of 100 cm^2 typical for a crystalline silicon solar cell. Due to monolithic integration by scribing the handling cost and time is reduced compared to silicon where each wafer has to be connected to the next wafer by soldering. [11]

At present, the following materials have been developed for use in the thin-film form for solar cells, hydrogenated amorphous silicon (a-Si:H), cadmium telluride (CdTe), copper indium diselenide (CuInSe_2) and its alloys with gallium and sulfur.

A thin film is a material created *ab initio* by the random nucleation and growth processes of individually condensing / reacting atomic / ionic /molecular species on a substrate. The structural, chemical, metallurgical and physical properties of such a material are strongly dependent on a large number of deposition parameters and may also be thickness dependent [4]. Thin-films may encompass a considerable thickness range, varying from a few nanometers to tens of micrometers and thus are best defined in terms of the deposition processes rather than by thickness. A thin material (not a thin-film) may be obtained by a number of other methods (normally called thick-film techniques) such as by thinning a bulk material, or by depositing clusters of microscopic species in such

processes as screen-printing, electrophoresis, slurry spray, plasma gun, ablation, etc. A thick film can indeed be very thin, limited by the size of the depositing clusters, and its properties may also be sensitive to the various deposition parameters. Being simpler, cheaper and having relatively much larger throughput or rate of deposition, thick-film techniques are of considerable interest for viable thin-film solar cell technologies.

The atomistic, random nucleation and growth processes impart new and exotic properties to thin-film materials. These properties can be controlled and reproduced, provided a range of deposition parameters are monitored and controlled precisely. In the early history of thin-film technology it was called as ‘fifth state of matter’—to indicate highly variable properties as fundamentals of thin-film materials were just beginning to be understood [4].

The following features of thin-film processes are of interest for solar cell technologies.

1. A variety of physical, chemical, electrochemical, plasma based and hybrid techniques are available for depositing thin-films of given material of interest.
2. Microstructure of the films of most materials can be varied from one extreme of amorphous/nanocrystalline to highly oriented and/or epitaxial growth, depending on the technique, deposition parameters and substrate.
3. A wide choice of shapes, sizes, areas and substrates are available.
4. Because of relaxed solubility conditions and a relaxed phase diagram, doping and alloying with compatible as well as some incompatible materials can be obtained [4].
5. Surface and grain boundaries can be passivated with suitable techniques.
6. Various types of electronic junctions, single and tandem junctions, are feasible.

7. Graded bandgap, graded composition, graded lattice constants, etc., can be obtained.
8. In case of multicomponent materials, composition, and hence bandgap and other optoelectronic properties, can be graded in desired manner [4].
9. Surfaces and interfaces can be modified to provide an interlayer diffusion barrier and surface electric field.
10. Surfaces can be modified to achieve desired optical reflectance/transmission characteristics, and optical trapping effects.
11. Integration of unit processes for manufacturing solar cells and integration of individual solar cells to prepare a cell-circuit can be accomplished [4].

The ability to tailor numerous properties of thin-films required for an efficient solar cell demands complete understanding of the material produced with the help of a range of monitoring and analytical facilities because the high sensitivity of film properties to deposition parameters can produce a multitude of undesired results [4]. In order to repetitively obtain the requisite film properties, it is essential to understand the effect of deposition parameters on film properties.

2.2 Copper Indium Gallium Diselenide ($\text{CuIn}_{1-x}\text{Ga}_x\text{Se}_2$)

During the initial years of thin-film solar cells evolution, considerable efforts were made for research, development and commercialization of $\text{Cu}_2\text{S}/\text{CdS}$ cells. However, these efforts had to be abandoned as these cells had instability problems caused mainly by copper migration. This led to the evolution of CuInSe_2 thin-film solar cells. The presence of trivalent indium seems to bind the Cu tightly in the chalcopyrite lattice, suppressing the copper migration degradation mechanism that affects the $\text{Cu}_2\text{S}/\text{CdS}$ cell. Since then,

I-III-VI₂ compounds are proving to be promising materials to meet the world energy requirement. CuInSe₂ (CIS) and its alloys with Ga and S have shown highest conversion efficiency of 19.9% [5] and a reasonable stability. CIS has a direct bandgap of 1.02 ± 0.01 eV at room temperature with a temperature coefficient of $-2 \pm 1 \times 10^{-4}$ eV/K in the lower temperature regime [12]. The typical absorption coefficient is larger than $10^5/\text{cm}$ for 1.4 eV and higher photon energies [13]. The band gap of CIS can be increased continuously over a wide range up to 1.68 eV by increasingly substituting In by Ga where the band gap increases as a function of Ga content [14]. Similarly, the band gap can also be increased by substituting S for Se up to 2.4 eV. The excellent radiation hardness property makes CIGS a suitable material for space applications [15]. The interface of CIGS with back contact and CdS are found to be stable [16]. A wide variety of techniques has been used to fabricate CIS. These include three-source evaporation [17] [18], laser ablation [19] [20], flash evaporation [21] [22], vapor transport [23], spray pyrolysis [24] [25], sputtering [26], liquid phase epitaxy [27][28], electrodeposition [29] [30] screen printing [31] and selenization of metallic layers [32] [33] [34]. Among the various ways of preparing CIGSeS/CdS thin-film solar cells, coevaporation and sputtering techniques are the most promising. Sputtering is an established process for very high-throughput manufacturing. ARCO Solar, later Shell Solar pioneered, the work in CIS using the sputtering technique [11]. The two stage process developed by ARCO Solar consisted of sputtering of a copper and indium layers on Mo-coated sodalime glass as the first step. In the second step, the copper-indium layers were exposed to a diluted selenium-bearing gas such as hydrogen selenide (H₂Se) mixed with argon. The hydrogen selenide breaks down and leaves selenium, which reacts and mixes with the copper and

indium to produce high-quality CIS absorber layer. Sputtering technology has the added advantage of being easily scalable and adaptable to roll-to-roll production on flexible substrates. In the early 90's, a nontoxic selenization process was developed at the FSEC's PV Materials Lab to avoid use of extremely toxic H_2Se gas. The two stage selenization process involved deposition of a copper-indium layer with excess copper. The elemental stack was selenized by heating the substrate in the presence of selenium vapors obtained by thermally evaporating elemental selenium. Selenization of the copper-rich film helped improve the adhesion with the Mo back contact. Indium was deposited on the copper-rich film to make it copper-poor and re-selenized to produce an efficient thin-film CIS absorber [35]. The process was further modified by addition of gallium and optimizing the Ga content to achieve a cell efficiency of 9.02% [36]. As of now, CIGSeS absorbers are prepared by rapid thermal processing of metallic precursor film with elemental selenium and conventional furnace annealing in selenium vapor obtained from diethylselenide (DESe) or other organometallic precursors [37] [38]. Sulfurization of the selenized film to form CIGSeS and of metallic precursors to form $CuIn_{1-x}Ga_xS_2$ (CIGS2) is carried out in diluted H_2S gas [32]. As of now in FSEC's photovoltaic materials laboratory, an efficiency of 13.73% has been obtained on a CIGSeS absorber layer prepared using diethylselenide as a selenium source. At that time, this was the highest efficiency obtained by two-stage process [39]. Research activities in FSEC photovoltaic materials laboratory on CIGS2 thin-film solar cells resulted in an efficiency of 11.99%, with an open circuit voltage, V_{oc} value of 830 mV, highest V_{oc} value obtained so far on CIGS2 type thin-film solar cells [40].

Prerequisites for efficient thin-film photovoltaic absorber materials are: (i)

The possibility to grow single-phase material of good crystalline quality, i.e., in a multinary compound there should be some tolerance to stoichiometry deviations. (ii) Growth of the material in a substrate configuration implies that during the growth process an ohmic contact with the metal on the sodalime glass must be formed for the majority carriers which should also have favorable recombination properties for the minority carriers. In addition, this interface plays an important role as the seed for the growth of the polycrystalline film; (iii) The absorber film should be thick enough to absorb all sunlight with photon energy above the semiconductor band gap and, at the same time, the minority carrier diffusion length should be large enough to enable collection of all photogenerated charge carriers [41], (iv) Intergrain defects should be few and/or electronically inactive, (This restriction is eased if the grain size exceeds the film thickness by at least an order of magnitude, which is not the case in Cu(In,Ga)Se_2 thin films), (v) The grains should not contain a high concentration of electronically active (intragrain) defects, (vi) the absorber layer surface should not be too rough and the absorber layer should have as less macroscopic defects, e.g. pores as possible, (vii) After the growth of the absorber film, the film surface should enable the formation of a heterojunction without an unfavorable band offset between the absorber and the heterojunction partner in order not to impede the photovoltaic performance [41].

2.2.1 Crystal Structure

CuInSe_2 and CuGaSe_2 , the materials that form the alloy Cu(In,Ga)Se_2 , belong to the semiconductor I-III-VI₂ material family that crystallizes in the tetragonal chalcopyrite structure and is stable from room temperature up to 810°C [42]. The chalcopyrite structure of CIS is similar to the ZnS structure in which Zn atoms are replaced

alternatively by Cu (I) and In (III) atoms. Each Cu and In atom has four bonds with Se (VI) atom. In turn each Se atom has two bonds to Cu and two more to In. Since the strength of the I-VI and III-VI bonds are in general different, the ratio of lattice constants c/a is not exactly 2. The quantity $2-c/a$ (which is -0.01 in CuInSe_2 , $+0.04$ in CuGaSe_2) is a measure of the tetragonal distortion in chalcopyrites. The bandgap energies of I-III-VI₂ are considerably smaller than those of their binary analogues because the Cu 3d band, together with the Se 4p band, forms the uppermost valence band in the Cu-chalcopyrite, which is not the case in II-VI compounds. However, the system of Cu-chalcopyrite covers a wide bandgap of energies from 1.02 eV in CuInSe_2 up to 2.4 eV in CuGaS_2 , or even to 2.7 eV for CuAlS_2 covering most of the visible spectrum. Any desired alloy between these compounds can be produced, as there is no miscibility gap in the entire system.

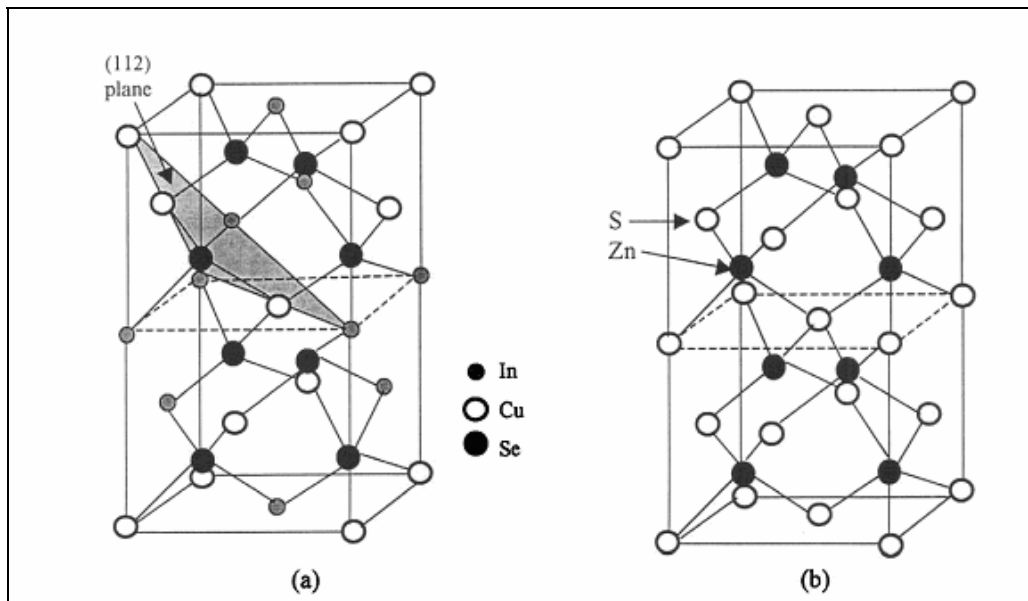


Figure 12: (a) CuInSe_2 chalcopyrite structure showing the (112) plane (b) Binary equivalent ZnS crystal structure

The CIS tetragonal structure shown in Figure 12, is similar to a stack of two FCC structures, where $c \sim 2a$. Since the FCC structure usually grows with closed packed (111) planes, CuInSe₂ will grow in (112) close packed plane. CuInSe₂ exhibits 142d symmetry, its atomic coordinates are as follows: four copper atoms at (0,0,0); ($\frac{1}{2}, \frac{1}{2}, \frac{1}{2}$); ($\frac{1}{2}, 0, \frac{3}{4}$); and ($0, \frac{1}{2}, \frac{1}{4}$); four indium atoms at (0,0, $\frac{1}{2}$); ($\frac{1}{2}, \frac{1}{2}, 0$); ($\frac{1}{2}, 0, \frac{1}{4}$); and ($0, \frac{1}{2}, \frac{3}{4}$); and eight selenium atoms at ($u, \frac{1}{4}, \frac{1}{8}$); ($-u, \frac{3}{4}, \frac{1}{8}$); ($\frac{3}{4}, u, \frac{7}{8}$); ($\frac{1}{4}, -u, \frac{7}{8}$); ($\frac{1}{2} + u, \frac{3}{4}, \frac{5}{8}$); ($\frac{1}{2} - u, \frac{1}{4}, \frac{5}{8}$); ($\frac{1}{4}, u + \frac{1}{2}, \frac{3}{8}$); and ($\frac{3}{4}, \frac{1}{2} - u, \frac{3}{8}$) where $u = c/a$. The lattice parameters for a CuIn_{1-x}Ga_xSe₂ film with Ga content, x of 0 is, $a = 0.578$ nm and $c = 1.162$ nm [43] and they decrease linearly with increase in x [43] [44].

2.2.2 Phase diagram

It is essential to obtain α phase in CIGSeS layers due to required photovoltaic characteristics of this phase. The phase diagram provides the alloy composition, the allowed deviation from stoichiometry and the process temperature for producing a good-quality absorber layer. Figure 13 shows a ternary elemental composition diagram of Cu, In and Se at room temperature. CIS absorber grown with excess supply of selenium has a composition on or near the tie line of Cu₂Se and In₂Se₃. It is interesting to note that the ordered defect compounds (ODC) such as CuIn₃Se₅, Cu₂In₄Se₇, and Cu₃In₅Se₉ lie on the same tie line and have the same chalcopyrite structure. The ordered defect compounds are formed by regular arrangements of point defects in the chalcopyrite crystal structure. This complex ternary diagram can be reduced to a simpler pseudo-binary phase diagram along the tie line between Cu₂Se and In₂Se₃ [45]. As seen from the phase diagram, the α -phase (CuInSe₂) lies in a very narrow range of 24 to 24.5% of copper at room temperature. At growth temperature between 500°C to 550°C, the α -phase exists in the range of 22 to 24.5

at% Cu. As per the phase diagram the cooling of slightly Cu-poor composition indicates the presence of additional β -phase (CuIn_3Se_5) also known as ordered defect compound. The ordered defect compound is built by ordered arrays of defect pairs of Cu vacancies and indium on copper anti-sites. Some groups have reported the formation and benefits of having such an ODC on top of the absorber layer [46]. This layer has a bandgap of 1.3 eV, which is higher than the bulk CIS bandgap of ~ 1 eV. Higher bandgap semiconductor at the metallurgical junction helps in increasing open circuit voltage (V_{oc}) [47]. When the absorber layer is grown in Cu-rich regime an additional phase, Cu_{2-x}Se is formed. This layer is metallic in nature and has to be removed before depositing the heterojunction partner. It has been found that the addition of a controlled amount of gallium or sodium widens the α -phase field making it possible to have single α -phase at room temperature in the range of 22 to 24.5 at% Cu. Another phase that occurs in the phase diagram is the δ -phase called sphalerite which is stable at high temperature. A congruent solid-solid phase transition occurs at 810°C between the disordered δ -phase and the ordered chalcopyrite α -phase. The reason to grow CuInSe_2 and its alloys with gallium and sulfur in a copper-poor regime is evident from the phase diagram (Figure 14) as the homogeneity of the α -phase extends over a range of composition towards copper poor compositions at the growth temperature while does not extend to the copper-rich side and not even the stoichiometric composition of 25 at % Cu [42].

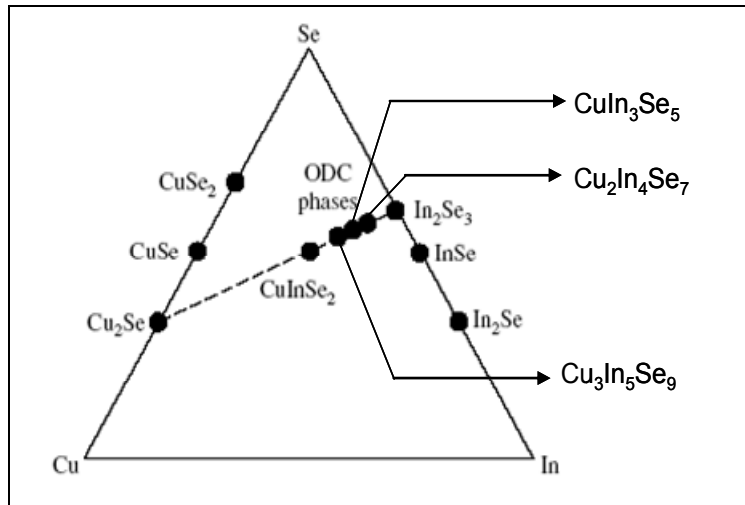


Figure 13: Ternary elemental composition diagram of Cu-In-Se [45].

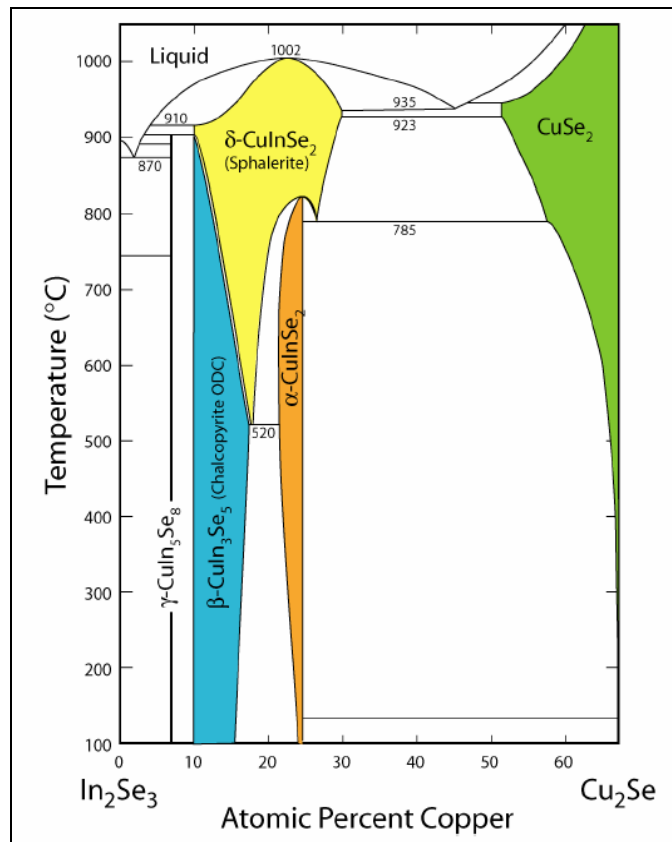


Figure 14: Pseudo-binary phase diagram along the tie line between Cu_2Se and In_2Se_3 represented in terms of Cu atomic % [45].

2.2.3 Intrinsic defect doping of CIGS

Small deviations from stoichiometry cause drastic changes in the electronic properties of binary compounds. The ternary compounds, in particular CuInSe_2 , are considerably more tolerant to stoichiometric deviations. The Cu content of device-quality CuInSe_2 or Cu(In,Ga)Se_2 absorbers varies typically between 22 and 24 at% Cu. Thus, these films are markedly Cu-poor but maintain excellent semiconducting properties. In terms of point defects, a non-stoichiometry of 1% would correspond to a defect concentration of roughly 10^{21} cm^{-3} . This is approximately five orders of magnitude higher than the acceptable density of recombination centers in a photovoltaic absorber material and still four orders of magnitude higher than the maximum net doping concentration of $\sim 10^{17} \text{ cm}^{-3}$ that has been indicated to be useful for the photovoltaic active part of a solar cell. The charge density in the space charge region of any photovoltaic device must not exceed $10^{17} - 10^{18} \text{ cm}^{-3}$. Otherwise tunneling enhanced recombination would significantly decrease the open circuit voltage of the solar cell. In fact, in Cu-chalcopyrite semiconductors this limit appears to be close to few times 10^{17} cm^{-3} . Cu(In,Ga)Se_2 absorber material in the highly efficient cells, has a net charge density of few times 10^{16} cm^{-3} [48].

Even if a degree of compensation of 99% is allowed, the respective densities of donors and acceptors would be only in the 10^{19} cm^{-3} range. Thus, the virtual number of defects related to off-stoichiometry has to be reduced to reasonable scale that is compatible with the good electronic quality required to build a photovoltaic device [48]. The most important characteristic of CIGS material is to accommodate a large compositional deviation without an appreciable change in the electronic properties. Highly efficient

solar cells can be fabricated with Cu/(In+Ga) ratio of 0.7 to slightly less than 1. This phenomenon can be explained on the basis of defect chemistry of CIS. It has been shown that the formation energy of defects such as copper vacancies V_{Cu} and defect complexes such as two copper vacancies in combination with indium on copper antisite ($2V_{Cu}+In_{Cu}$) is low [49]. V_{Cu} is a shallow acceptor that contributes to the p-type conductivity of CIGS. The $2V_{Cu}+In_{Cu}$ defect prevents degenerate doping in indium-rich material. Isolated In_{Cu} acts as a deep double donor while the combination with $2V_{Cu}$ has no deep level and is electrically neutral. At high concentrations of $2V_{Cu}+In_{Cu}$ complexes, their formation energy is further reduced. Thus the creation of such defect complexes can compensate for Cu-poor/In-rich composition of CIGS without adverse effects on the photovoltaic properties. Doping of the CIGS semiconductor is controlled by intrinsic defects. Samples with p-type conductivity are grown if the material is copper poor and annealed under high Se vapor pressure, whereas Cu-rich material with Se deficiency tends to be n-type [50] [51]. Thus Se vacancy (V_{Se}) is considered to be the dominant donor in n-type CIGS and also compensating donor in p-type CIGS while V_{Cu} is dominant acceptor in Cu-poor p-type material. Cu-poor material has In_{Cu} antisite donor defects along with V_{Cu} acceptors, resulting in heavily compensated p-type material limiting the acceptor density to non-degenerate levels. In the case of excess Cu, dominant defects are Cu_{In} antisite and In vacancy (V_{In}) acceptors, both of which contribute to a highly p-type material.

CIGS grain boundaries that are parallel to the current flow direction can be modified electronically by dopants such as oxygen, and by low-temperature post-processing heat treatments, without affecting the bulk chemistry. As a result, grain boundaries can be made electronically benign [52].

2.2.4 Microstructure of CIGS thin-films

The main factor that separates the polycrystalline thin films from their single crystal counterpart is the grain boundaries. Grain boundaries are formed when individual islands coalesce during growth of the films. Generally, the grain boundaries are regions of high density of defects and impurities segregated from the grains during growth. Grain size of the films is a function of deposition parameters and generally the conditions are chosen to maximize the grain size of the films. For single crystals, growth under thermal equilibrium conditions with very slow growth rates results in a mostly defect-free material. In case of polycrystalline materials, the economic considerations are important, dictating the use of inexpensive substrates, and deposition systems capable of high throughput. This compromise requires a balance between the cost and performance. Hence, the relevant factors and their impact on device performance need to be considered [53].

Even though III-V materials have been most successful for the epitaxially grown solar cells, best III-V polycrystalline devices using GaAs and InP have efficiencies lower than their single crystal counterparts. Grain boundaries are active in these devices and attempts to passivate grain boundaries have not been successful. The situation is different with II-VI compounds. Where, performance comparable to and even exceeding the single crystal counterparts has been obtained [53].

Problem of grain boundaries can be minimized when majority of the grains are columnar, having very few grain boundaries in the path of current flow. From the device performance point of view, the grain boundaries in these cells are electrically passivated and do not hinder the performance greatly.

The electrical activity at the grain boundaries is a controlling factor that determines the properties of the films. Grain boundaries can be separated in three classes:

- 1) Coherent twins – These have negligible electrical activity.
- 2) Low angle grain boundaries – include a net of edge dislocations accompanied by lattice strain fields. These show moderate electrical activity.

- 3) High-angle grain boundaries and incoherent twinning – These include high densities of dislocations which may extend considerably in the bulk of the grains, lattice strain and considerable impurity segregation. They also show considerable electrical activity. The dislocations present at such boundaries may produce states within the bandgap due to strain fields and the dangling bonds. The grain boundaries can be the region of depletion, inversion or accumulation depending on the nature of impurities and defects present at the boundary. This results in the formation of potential barriers at grain boundaries. The depletion is more probable for intrinsic, undoped grain boundaries. The intergrain potential barriers present obstacle to the carrier transport and can reduce the carrier mobility by orders of magnitude compared to the single crystal materials. Following are the ways to modify grain boundaries to reduce the recombination losses [53].

- 1) Neutralization of the electrical activity of the grain boundary states by addition of selective impurities.
- 2) Making the grain boundaries part of the junction by preferential diffusion doping of the grain boundary to the opposite type.

In polycrystalline thin film solar cells, so far, no special consideration is given to minimize the adverse effects of grain boundaries. However, there is evidence that some

of the processing steps and intrinsic material properties do help to reduce the activity at the grain boundaries [53].

The effect of grain boundary potential is maximum when the current has to traverse across the grain boundaries. In case of successful thin film solar cells, grains in the absorber grow in columnar fashion so that the current flow is parallel to the grain boundaries reducing the impact of grain boundaries on the current flow [53].

It is important to note that the typical grain size of CIGS films is a few microns, whereas, grain size in multicrystalline silicon solar cells is few centimeters. Thus, the grain boundary area in CIGS thin-film is $\sim 10^4$ times higher as compared to multicrystalline silicon. However, the efficiencies obtained using CIGS thin-films are approaching the efficiencies of crystalline silicon. It is very surprising that the CIGS thin-film solar cells are tolerant to grain boundaries to such an extent! As, it is generally believed that grain boundaries act as recombination centers and reduce the solar cell efficiency.

In all common semiconductors, the lowest energy surface is the “nonpolar surface” also denoted (110), which contains equal numbers of anions (As) and cations (Ga). However, it has been demonstrated that chalcopyrites are substantially different in this respect: the most stable surface is the “polar surface” also denoted (112) surface, which has either anions (Se) or cations (Copper (Cu)) termination, but not both. Quantum calculations on grain boundaries in CIGS, modeling them as “internal surfaces have shown that just like the surface, the grain boundary too has a special atomic structure that makes the polar surface energetically stable. This atomic structure consists of neutral array of Cu vacancies in the grain boundary.

Quantum calculations also show that an array of neutral Cu vacancies causes the valence-band maximum (VBM) to move down in energy. The VBM of bulk CuInSe₂ consists of Cu d orbitals which strongly interact with the Se p orbitals, forming both the bonding and antibonding states in the valence band. Therefore, the Cu, d–Se, p repulsion shifts the antibonding VBM upwards. Removal of Cu atoms from the grain boundary and surface region diminishes this repulsion, and thus lowers the VBM at the free CIGS surface and at the grain boundaries. Therefore, reconstruction of the grain boundary interface via Cu vacancies lowers VBM at the grain boundary, thereby repelling the holes from this region. The hole barrier arises due to the lack of d-electron states rather than from an electrostatic potential of charged defects. This causes holes to be repelled from the grain boundary region (where the VBM is low) into the grain-interior. Thus, photogenerated electron-hole pairs are dissociated at the grain boundary, with electrons penetrating the grain boundary, while holes are repelled in the grain boundary region (by ~300-400 meV). Consequently, despite the existence of numerous impurities and defects, there is no recombination at the grain boundaries of CIGS. This may be one of the effects that have allowed polycrystalline CIGS to outperform monocrystalline CIGS [54].

The existence of grain boundaries in polycrystalline materials cleans up the grain interior, because most defects are drawn into the grain boundaries, leaving the grain interior with lower concentration of impurities and defects. Now, in CIGS, there is minimal recombination at the grain boundaries (because of the hole repulsive character of grain boundaries) and little recombination in the grain interior (because of higher purity and lower concentration of defects). Thus, there is indication that polycrystalline CIGS could be intrinsically better than crystalline CIGS [54].

2.2.5 Bandgap engineering by Ga addition and sulfurization

Incorporation of Ga and S leads to an increase in the bandgap of CIS [14] by increasing the energy of the conduction band in the case of Ga [49] while main effect of sulfur is to reduce the valance band maximum energy [55].

The increase in bandgap with gallium content, x is governed by the relation

$$E_g \text{ (eV)} = 1.010 + 0.626 x - 0.167 x (1-x) \text{ [56].}$$

Whereas the increase in the bandgap with gallium content, x and sulfur content, y is governed by the relation,

$$E_g \text{ (eV)} = 1 + 0.13 x^2 + 0.08 x^2 y + 0.13 xy + 0.55x + 0.54 y \text{ [57]}$$

Gallium tends to diffuse towards the back contact and form $\text{CuIn}_{1-x}\text{Ga}_x\text{Se}_2$ having higher gallium content [52]. As gallium content increases in $\text{CuIn}_{1-x}\text{Ga}_x\text{Se}_2$, bandgap also increases as CGS is a wide bandgap semiconductor with a bandgap of 1.68 eV. The bandgap gradient created between gallium poor $\text{CuIn}_{1-x}\text{Ga}_x\text{Se}_2$ and gallium rich $\text{CuIn}_{1-x}\text{Ga}_x\text{Se}_2$ creates a back surface field (BSF) that acts as a mirror for the electrons moving towards the back contact. The BSF greatly suppresses the back contact recombination and increases the open circuit voltage [58]. Also the formation energy for a Ga_{Cu} defect is higher than the formation energy of In_{Cu} . This destabilizes the formation of defect pairs of $2\text{V}_{\text{Cu}}+\text{In}_{\text{Cu}}$ thereby reducing the tendency for the formation of ODC [59] and enhancing the α -CIGS region.

Sulfurization of metallic precursors is a well-developed process to produce a high-bandgap (1.55eV) absorber. The Hahn-Meitner-Institut of Germany has developed a similar process using elemental sulfur evaporation [60]. Sulfurization is considered as a bandgap engineering treatment for the selenide absorber. The open-circuit voltage, V_{oc}

mainly depends on the band gap in the space charge region. CIGS with Ga ~ 30 at% has a bandgap of 1.12 eV, this comparatively lower bandgap value, results in relatively lower open circuit voltage (V_{oc}). Sulfurization leads to the formation of CIGSeS or CIGS₂ layer at the interface. Having a wider bandgap of 1.55eV at the p-n junctions helps in increasing the open circuit voltage (V_{oc}). During the sulfurization treatment the sulfur atoms occupy already existing selenium vacancies or replace selenium because of the higher reactivity of sulfur compared to selenium, thereby reducing the compensating donors and also passivating the surface [61].

2.2.6 Effect of Na addition

The highest efficiencies of Cu(In,Ga)Se₂, thin-film solar cells have been obtained by using sodalime glass as substrate material. Sodalime glass contains significant amounts of sodium in the form of Na₂O. It has been shown that the presence of sodium during growth of the CIGS absorber layer is beneficial for the device performance. Among the available sodium containing precursor, NaF is non-hygroscopic, stable in air and evaporates congruently [62]. Selenization of the film containing sodium results in the formation of Na₂Se_x compounds that retard the growth of the CIGS phase, thereby incorporating relatively more selenium in the film [63]. Thus, the number of compensating donors are reduced by filling selenium vacancies, V_{se} and therefore, increasing the p-type conductivity. Sodium also replaces In_{Cu} antisite defects further reducing the compensating donors [64]. Apart from reducing the compensating donor sodium also replaces copper vacancies, thereby reducing the formation of ordered defect compound. Sodium and Gallium addition in CuInSe₂ increase the α -phase region as shown in Figure 15. Sodium has also been shown to passivate the surface and grain

boundaries by promoting incorporation of oxygen [65]. Sodium promotes of increase in grain size and preferred (112) orientation of CIGS films [62]. Although in some studies sodium did not affect the grain-size of the CIGS film or even reduced the grain size [66].The overall effect of sodium incorporation during grain growth is an increase in efficiency by enhancements of fill factor and open circuit voltage. Addition of sodium also results in Cu-poor film with higher charge carrier mobility. This helps in fabrication of higher efficiency cells without KCN treatment.

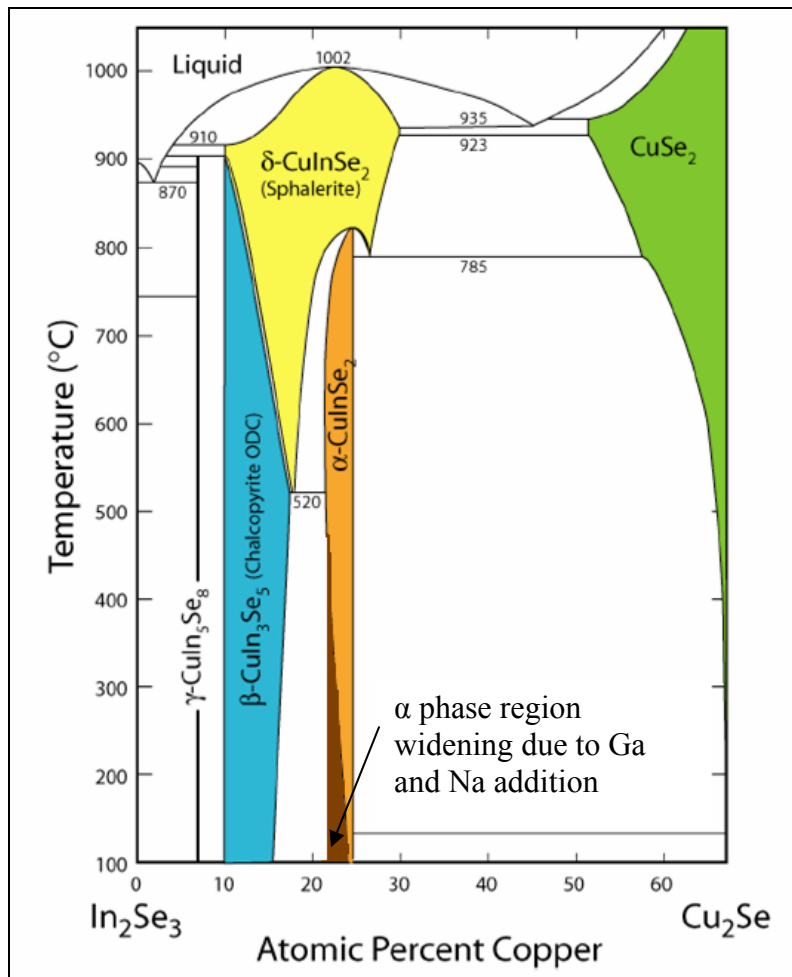
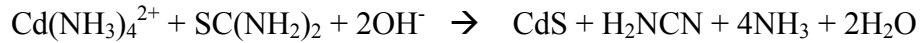


Figure 15: Pseudo-binary phase diagram along the tie line between Cu_2Se and In_2Se_3 showing the α phase region widening due to Ga and Na addition

2.3 Heterojunction Partner layer – Cadmium sulfide (CdS)

CdS is an n-type semiconductor. It is one of the most extensively investigated semiconductors in the thin-film form and a large variety of deposition techniques have been utilized to obtain device quality layers of CdS [67]. It is a heterojunction partner in CIGS solar cells with a bandgap of 2.45 eV. Cross section images of the CuInSe₂/CdS interface show that CdS can grow epitaxially on CIS [68]. It also serves as a window layer that allows the light to pass through it with relatively small absorption. Also, because the carrier density in CdS is much larger than in CIGS, the depletion field resides mostly in the CIGS layer where electron-hole pairs are generated.

CdS films are usually grown by chemical bath deposition (CBD). The crystal structure can be varied depending upon the deposition parameters [69]. CdS deposited by the CBD route has wurtzite crystal structure with the c axis perpendicular to the substrate plane. This film grows in a closed packed plane (0001) in the close-packed direction <0001>. A 500 Å film has yellow to orange color and when grown on CIGS a bluish to purple color is seen. The optical absorption edge of solution grown CdS films is the same as that of corresponding bulk material. Deposition of CdS heterojunction partner layer on the CIGS absorber is generally carried out in an alkaline aqueous solution of pH > 9, consisting of cadmium salt (CdSO₄), a complexing agent (NH₄OH) and a sulfur precursor thiourea, SC(NH₂)₂. The complexing agent slows down the reaction and prevents the formation of Cd(OH)₂. The concentration of thiourea is usually much higher than that of the metal precursor. The deposition is carried out in the temperature range of 60 to 80 °C where thiourea hydrolyzes and decomposes releasing S²⁻ ions. The net reaction for the formation of CdS is



There are several benefits of the CdS layer:

1. CBD deposition of CdS provides conformal coverage of the rough polycrystalline absorber surface.
2. The layer protects against damages and chemical reactions resulting from subsequent ZnO deposition process.
3. The chemical bath removes the natural oxide from the film surface thus, it re-establishes positively charged surface states and, as a consequence, the natural type inversion at the heterojunction partner/ absorber interface.
4. Cd also diffuses to a certain extent into the Cu-poor surface layer of the absorber material, where it possibly forms Cd_{Cu} donors, thus providing additional positive charges that enhance the type inversion of the heterojunction partner (CdS)/absorber interface [70].
5. From the electrical point of view, the CdS layer optimizes the band alignment of the device [71] and builds a sufficiently wide depletion layer that minimizes tunneling and establishes a higher contact potential that allows higher open circuit voltage [72].

2.4 Transparent conducting oxide window bilayer– intrinsic ZnO and Zinc oxide doped with aluminum (ZnO:Al)

A very thin layer (~50-90 nm) of highly resistive intrinsic ZnO (i:ZnO) is used to prevent the direct contact of transparent and conducting oxide (ZnO:Al) and CIGSeS absorber or even ZnO:Al and molybdenum back contact and thereby reduce the shunt paths. The thickness of i:ZnO is very critical. If the layer is thinner than the critical value, it may

lead to increase in leakage currents. An excessively thicker layer gradually reduces the current density due to an increase in series resistance. The coverage of the i:ZnO layer greatly influences the open circuit voltage, V_{oc} and the fill factor, FF [73]. ZnO is a low-cost and abundant material having a bandgap of 3.3 eV making it transparent to the visible spectra. It can be easily doped with group III elements such as Al, B [74] and Ga [75] for high conductivity. Therefore, ZnO:Al is frequently used as a transparent and conducting front contact in thin-film solar cells with CIGS absorber. ZnO:Al targets usually contain 2-wt% Al_2O_3 to make it highly conducting. It has hexagonal wurtzite structure with n-type conductivity.

Radio Frequency (RF) sputtering, with a frequency of 13.65 MHz is generally used for deposition of i:ZnO while RF or DC plasma can be used for the deposition of ZnO:Al. The electrical conductivity of pure ZnO is due to intrinsic defects, i.e. oxygen vacancies (V_O) and zinc interstitials (Zn_i) that act as shallow n type donors [76] [77]. Incorporation of electrically active defects in sputter-deposited ZnO layers depends critically on sputter deposition parameters such as pressure, gas flux, RF power and the distance between the target and the substrate. Oxygen depletion of the sputter plasma leads to the deposition of metallic zinc along with zinc oxide. In order to obtain transparent layers, oxygen is added to the sputter gas or the layers are deposited on heated substrates where the free zinc is re-evaporated. However, the use of excessive quantities oxygen or very high temperatures prevents the formation of the defect related donors and results in highly resistive layers [78]. Thus, the addition of oxygen must be controlled precisely [79].

In case of ZnO:Al it has been shown by Hall measurements that resistivity is influenced to a large extent by carrier density and only slightly by mobility; low resistivity

corresponds to higher carrier density and vice versa. Mobilities in the range of 10 to 30 cm^2/Vs are typical for RF sputtered ZnO doped with aluminum [79] [80]. Doping of ZnO is a critical process as excessive doping enhances the free carrier absorption preventing the low energy photon from contributing to the current. These transparent conducting oxides (TCO) are sequentially deposited on CdS film with initial layer of $\sim 500\text{-}900 \text{ \AA}$ of highly resistive intrinsic ZnO followed by $\sim 5000 \text{ \AA}$ of ZnO:Al.

2.5 Rapid Thermal Processing

Rapid thermal processing (RTP) originally developed for processing microelectronic devices has been investigated during the last decade for its potential in the production of solar cells. RTP provides a way to rapidly heat substrates to an elevated temperature to perform relatively short processes, typically less than 1-2 minutes long thus reducing the thermal budget. Over the years, RTP has become essential to the manufacturing of advanced semiconductors, where it is used for oxidation, annealing, silicide formation and deposition. A rapid thermal processing system heats the substrate singly, using radiant energy sources controlled by a pyrometer that measures the substrate temperature. Previous thermal processing was based on batch furnaces, where a large batch of substrates is heated in a tube. Batch furnaces are still widely used, but are more appropriate for relatively long processes of more than 10 minutes. RTP is a flexible technology that provides fast heating and cooling to process temperatures of $\sim 200\text{-}1300^\circ\text{C}$ with ramp rates of typically $20\text{-}250^\circ\text{C}/\text{sec}$, combined with excellent ambient control, allowing the creation of sophisticated multistage processes within one processing recipe. This capability to process at elevated temperatures for short time periods is crucial because advanced solar cell fabrication requires thermal budget minimization to restrict

dopant diffusion. Replacement of the slower batch processes with RTP also enables to greatly reduce manufacturing cycle time, an especially valuable benefit during yield ramps and where cycle-time minimization has economic value [81].

RTP systems use a variety of heating configurations, energy sources and temperature control methods. The most widespread approach involves heating the substrate using banks of tungsten-halogen lamps because these lamps provide a convenient, efficient and fast-reacting thermal source that can be easily controlled. In a typical RTP system (shown in Figure 16), the substrate is heated by two banks of linear lamps - one above and one below the substrate. The lamps are further subdivided into groups or zones that can be individually programmed with various powers to optimize temperature uniformity. In RTP, the energy sources face the substrate surfaces rather than heating its edge, as it happens in some batch furnaces. Thus, RTP systems can process large substrates without compromising process uniformity or ramp rates [81].

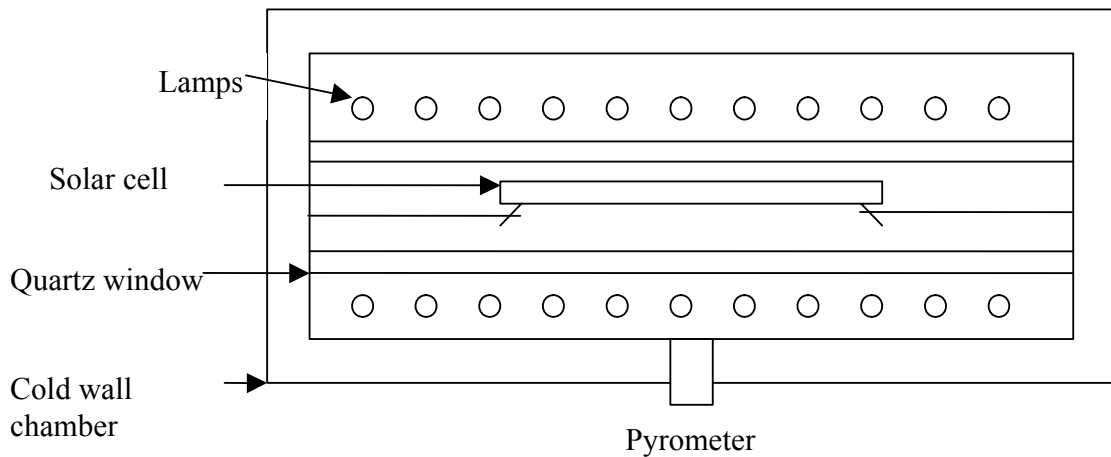


Figure 16: Generic RTP system

RTP has been developed for the microelectronics industry in order to obtain very narrow and thin device structures by minimizing the thermal budget that a single wafer

experiences during processing. Extremely steep temperature ramps are used to avoid any unwanted diffusion or oxidation during ramp up or ramp down. For the same reason processing times are kept extremely short. Thus RTP technique can be utilized to minimize the process time cycle thus eliminating a bottleneck in CIGS module fabrication. In silicon solar cells fabrication, the good controllability, repeatability and homogeneity of RTP has allowed fabricating solar cells with very shallow emitter regions (Rapid Thermal Diffusion) having extremely steep gradients in the phosphorus (P) concentrations. Furthermore, thin passivating high-temperature oxides (Rapid Thermal Oxidation) and short thermal anneals (Rapid Thermal Annealing) as for instance for the metal contacts (Rapid Thermal Multiprocessing) have been successfully applied in solar cell processing. Some approaches were able to obtain solar cells with conversion efficiencies close or equal to those for conventionally processed solar cells with similar device structures [82].

Today's state-of-the-art RTP systems can control the temperature distribution across the substrate surface with variation smaller than 2°C. However, device patterns on the substrate surface impose a limit. Because RTP systems heat the substrate with radiant energy, process temperature can be affected by its optical properties. Thus, device patterns can induce temperature non-uniformities. Different solutions can address the pattern effect, including dual-sided heating methods that reduce the lamp power incident to the patterned surface, and approaches that irradiate the patterned surface with a heat source close to the substrate temperature. Fortunately, the surface of the substrate having Cu-In-Ga metallic precursors and selenium layer on top has no patterns, thus having uniform optical properties and hence is appropriate for the application of RTP.

A RTP reactor for preparation of CIGSeS thin films on 4"x 4" substrates has been designed; its components have been built, and installed. And this RTP reactor is currently being used at the FSEC Photovoltaic Materials Lab.

The main process requirements for the CIGSeS formation are as follows:

- (i) High heating rates
- (ii) Homogeneous substrate temperature distribution (maximum tolerable thermal inhomogeneities of $\pm 10^\circ \text{C}$ to avoid substrate breakage)
- (iii) Control of selenium and H_2S partial pressures
- (iv) Corrosion resistivity of the reaction chamber and other components against the processing gases, especially against Se and H_2S vapor to ensure sufficiently long uptimes and low particulate concentrations even under mass production conditions [83]

The requirements of thermal homogeneity even at high ramp rates is complicated by the one side precursor coating on the sodalime glass substrate, because in terms of radiative heat transfer, the single side coated sodalime glass substrate is strongly asymmetrical. The coated sodalime glass panel has to be arranged in between two independently adjustable and controllable heater arrays in order to compensate for this asymmetry. Control of the two heater arrays each directed respectively to the front and back sides of the substrate has to be performed in such a way that the thermal gradient across the thickness of the substrate remains symmetrical during all RTP processing phases. Otherwise the substrate would bend and crack [83]. The total IR power density of the large area RTP reactor is sufficient to allow heating rates of $\sim 4^\circ \text{C}/\text{sec}$ on 3 mm thick sodalime glass substrates. The reaction chamber has a minimized volume to ensure high Se and H_2S partial pressures. CuInS_2 thin films and cells with 11.4% efficiency have been

prepared by sulfurization in S vapor in a rapid thermal process of metallic Cu/In precursors [84]. Cycle-time & thermal-budget minimization would benefit large-scale PV manufacturing.

CHAPTER 3

EXPERIMENTAL TECHNIQUE

3.1 Rapid Thermal Processing (RTP)

3.1.1 Rapid Thermal Processing set-up

A Rapid Thermal Processing (RTP) unit has been designed, constructed and installed for preparation of CIGSeS thin films on 10 cm x 10 cm substrates by selenization/sulfurization of elemental precursors using the vacuum deposited selenium layer and N₂:H₂S atmosphere. Before carrying out CIGS compound formation by RTP, selenium evaporation was carried out by thermal evaporation in another unit.

The RTP configuration and schematic are shown in Figures 17 and 18 respectively. A quartz tube was mounted with a stainless steel flange assembly. Feedthroughs were mounted on the end flange for connection to thermocouples which monitor temperature. Viton rubber 'O' ring in a groove was used to form an air-tight seal between the hard surfaces of the stainless steel flange and quartz glass tube. Two heater arrays of the RTP set-up have to be controlled independently to maintain thermal gradient across the thickness of the substrate symmetrical during all RTP processing phases so as to prevent the substrate from breaking and cracking.

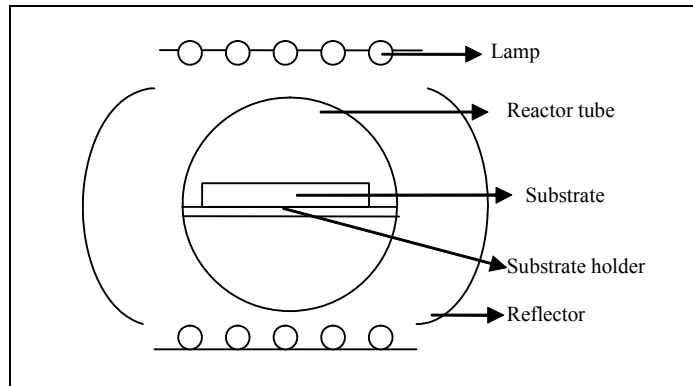


Figure 17: RTP System Configuration

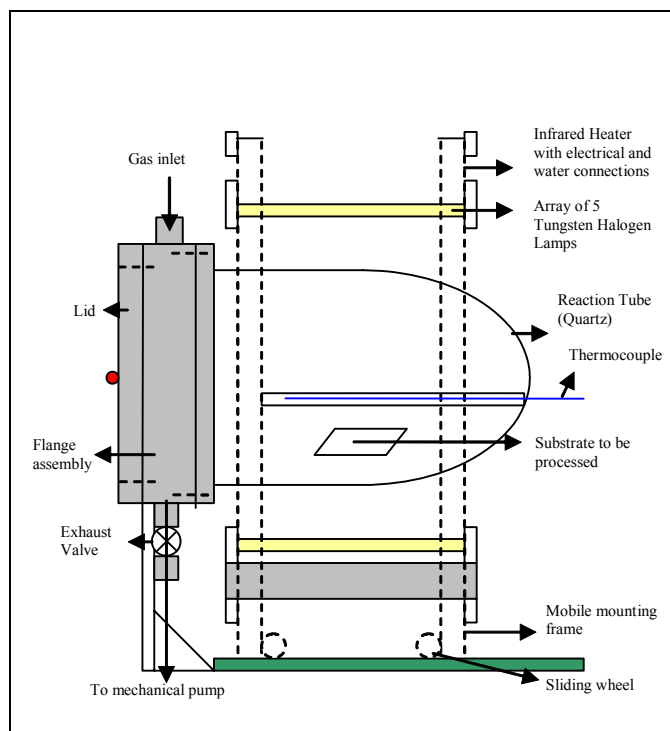


Figure 18: RTP Schematic

Each heater consists of a specular aluminum reflector that directs the infrared energy supplied by the lamps on to the substrate. Cooling water was provided to avoid overheating of the heater assembly. The heaters were mounted on a stand so as to face both the surfaces of the substrate. Cold water at $\sim 13^{\circ}\text{C}$ was circulated through each of the two infrared heaters at a rate of approximately 1.4 liters per minute per heater assembly.

Two aluminum sheets with 95% reflectivity and measuring 30 cm x 30 cm x 0.05 cm were formed into arcs and installed laterally on both sides of the quartz tube to reflect the heat back to the substrate during RTP. Circular reflective stainless steel sheets were placed within the quartz tube at both ends. A sliding mechanism was provided to quickly move the heaters away from the reaction tube after the completion of the process for rapid cooling. Figure 19 shows the RTP set up and Figure 20 shows RTP setup during actual run. This work was done in collaboration with Ms. Jyoti Shirolikar.

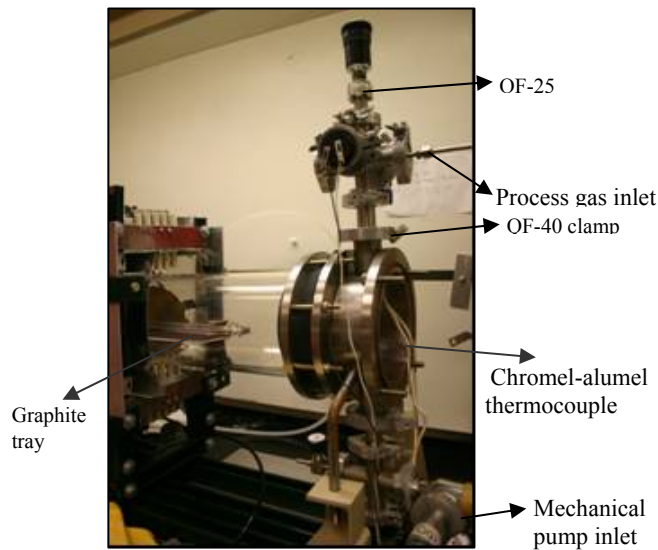


Figure 19: RTP Setup

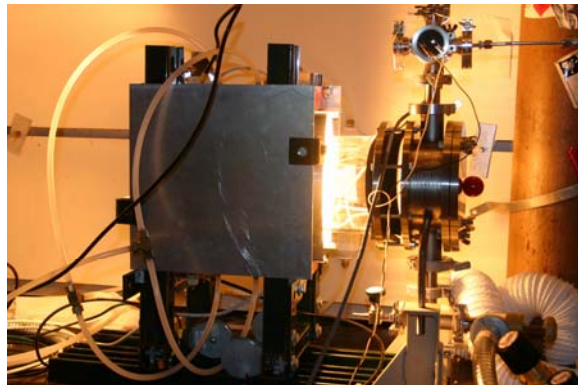


Figure 20: RTP setup during actual run

3.1.2 Flange fabrication

For the RTP chamber, a quartz glass process tube and the stainless steel flange were fabricated elsewhere based on the FSEC designs. The material for the flange was chosen to be 304 grade stainless steel for corrosion resistance at higher temperature for sulfur containing gases.

3.1.3 Vacuum and gas filling

Vacuum in 10^{-2} to 10^{-3} Torr range was obtained in the RTP reaction tube by means of a mechanical pump. The gas flow for both type of gases ultra high purity (UHP) nitrogen and H_2S was controlled using a mass flow controllers (MFC).

3.1.4 Temperature measurements and finalizing RTP ramp-up cycle

Temperature measurement is one of the important things during a RTP run. RTP being a non-equilibrium process, i.e. the substrate, chamber and heaters are at significantly different temperatures; temperature measurement of substrates does have its unique requirements. Following experiments were carried out in order to measure and control the temperatures during the RTP run.

Experiment series 1: Several experiments were carried out during RTP run, to measure the temperature of the substrate by means of a type-K chromel-alumel thermocouple. The tip of this thermocouple was glued to the sodalime glass substrate. The chromel-alumel thermocouple has ceramic beads for insulation, these beads used to break during closing the RTP reaction tube flange and the thermocouple wires were somewhat rigid, hence in further experimental runs they were abandoned and instead other options were sought.

Experiment series 2: Temperature lacquer marking paints having different colors were procured, marks made by these paints change color once the specific temperature for that color is obtained within the RTP reaction chamber. Table 1 shows the temperatures and colors for different inks.

Table 1: Inks colors and temperatures

Ink Color	Temperature
Violet	450°C
Off White	475 °C
Green	500 °C
Carrot	550 °C

Several experiments were carried out to check during what time different temperatures were reached, i.e. when the color change occurs. Even though the color changing inks at specific temperatures gave a fairly accurate estimation of the temperatures reached during specific time at given power; it could not be used during actual RTP runs due to contamination concerns. Also the thermocouples could not be used during actual RTP runs due to the shortcomings mentioned earlier. Therefore, new specially designed thermocouples were procured, having required flexibility, high temperature corrosion resistance in sulfur containing atmosphere, and instead of ceramic beads the insulation was provided in a single shielded wire.

Experimental series 3: Several experiments were conducted using these new thermocouples to find out the time-temperature data. Moreover, these thermocouples

could also be used during the actual RTP runs, and hence were continued for temperature measurements during further experiments.

Experimental series 4: Contactless temperature measurements were also tried using portable IR thermometer in order to reduce the thermocouple wiring inside the RTP process chamber. However, due to reflection from RTP process chamber quartz glass surface, these experiments did have relatively higher margin of error, and hence was not continued for further experiments.

Results and discussion: From all these experiments, it was found out that at 100% power, 150 seconds (i.e. 2 minutes 30 seconds) were required to reach the required process temperature of 550°C and a power setting of 52% was sufficient to maintain the process temperature at 550°C for the required process time.

3.1.5 Temperature uniformity during RTP run.

After finalizing the time and temperature during the RTP run, next step was to control the temperature uniformity during the RTP run for the substrate area of 4" x 4", even though actual experiments were carried on 1" x 4" substrates. As it was planned to prepare cells on 4" x 4" mini-module area after completion of experiments on 1" x 4" area.

Experimental series: Experiments were carried out to measure the temperature uniformity during RTP run, and then further experiments were carried out to obtain better uniformity over the given area by independently adjusting top and bottom array of heaters.

Results and discussion: From these experiments, it was observed that controlling both of the heater assemblies (i.e. the top one and the bottom one) simultaneously, better temperature uniformity was obtained across the substrate. The uniformity achieved was within $\pm 2.5\%$ over the entire area.

3.2 CIGSeS Solar cell preparation by RTP

3.2.1 NaF sequence

As explained in the second chapter, sodium incorporation in the absorber layer is beneficial due to various reasons. This was done by evaporation of NaF compound. Earlier NaF layer was deposited after the copper, indium and gallium layers. However, as sodium is beneficial during the absorber growth process, NaF layer should be deposited before copper-gallium, and indium layer deposition [85] [86]. NaF layers of various thicknesses e.g. 40 Å, 80 Å, 120 Å were deposited.

3.2.2 Deposition of Copper gallium and indium metallic precursors

NaF deposition was followed by deposition of copper, gallium and indium metallic precursors by DC magnetron sputtering and then thermal evaporation of selenium. The deposition parameters for metallic precursors were optimized to obtain an absorber thickness of ~ 2 μm . A precursor film of copper-gallium was sputtered from a copper-gallium alloy target having 22 atomic % gallium. Indium metallic precursors were sputtered from indium target. Metallic precursor deposition was carried out by DC magnetron sputtering. Copper-gallium alloy film was deposited at sputtering power of 350 Watts and argon pressure of 1.5×10^{-3} Torr while indium was deposited at sputtering power of 230 Watts and argon pressure of 7×10^{-4} Torr.

3.2.3 Optimization of selenium quantity

The deposition of metallic precursors was followed by over-stoichiometric Se deposition by thermal evaporation. As no external Se-vapor source was used during the reaction

process, the natural loss of a portion of Se during heating was compensated by an excess of Se deposited onto the precursor stack [87] [88]. The step following the selenium deposition was selenization/sulfurization by RTP using deposited selenium as the selenium source and H₂S as a sulfur source. Various experiments were carried out to optimize the amount of selenium being deposited. As explained in earlier section 3.5, selenium evaporates during RTP, so as to compensate for the loss of selenium, over-stoichiometric selenium was deposited, and the amount of selenium evaporated was minimized by using proprietary design.

3.2.4 CdS deposition

After the CIGSeS layer was completed the next step was deposition of heterojunction partner layer, CdS. The copper-rich phase, if any on CIGSeS surface, was etched away in dilute KCN. CdS heterojunction partner layer was deposited using chemical bath deposition technique. Advantages of using chemical bath deposition have been described in Chapter 2. A new chemical bath deposition setup was designed and built for 10 cm x 10 cm sodalime glass and stainless steel substrates. The chemical bath consisted of required amount of distilled deionized water, 0.015M CdSO₄, ammonium hydroxide (NH₄OH), and 1.5M (NH₂)₂CS. The temperature of water in the outside bath must be controlled carefully to achieve the desired maximum temperature of CdS deposition in the chemical bath. The substrates having CIGSeS absorber were kept inside a beaker containing chemical bath. Then, the beaker containing the substrates and the chemical bath was placed inside another larger beaker containing hot water. This larger beaker having hot water is known as outside beaker. Because of the temperature difference in the chemical bath and outside beaker, temperature in the chemical bath starts increasing and

reaches the desired maximum temperature. The ramp rate to achieve maximum temperature depends on the volume of solution in the chemical bath. Figure 21 shows a photograph of CBD experimental setup.



Figure 21: Chemical Bath Deposition setup

3.2.5 Front contact bilayer deposition

Bilayer of i-ZnO/ZnO:Al was deposited using RF magnetron sputtering. The CIGSeS thin-film solar cells with CdS heterojunction partner layer deposited by chemical bath deposition were mounted into the RF magnetron sputtering chamber and kept overnight in vacuum ($\sim 2 \times 10^{-6}$ Torr). Linear substrate motion mechanism was used to move the substrates at the requisite speed to achieve desired thickness. Earlier series of experiments carried out to optimize the process parameters for deposition of highly transparent and conducting i-ZnO/ZnO:Al bilayer served as a base for this research. A thin layer of ~ 50 nm i-ZnO layer was deposited at RF power of 200 Watt and argon pressure of 1.5 mTorr and ~ 500 nm thick ZnO:Al was deposited at RF power of 425 Watt

and argon pressure of 1.5 mTorr. The sheet resistance of the deposited ZnO:Al films was 40–60 Ω per square and transparency of more than 85% . CIGSeS thin film solar cells were completed by Cr/Ag contact fingers deposition by thermal evaporation through shadow masks.

3.2.6 Antireflection coating process

MgF₂ anti-reflection coating was applied on to high efficiency cells. The MgF₂ coating was calibrated and thickness of ~ 1000 Å was deposited by vacuum evaporation. The final cell structure was as follows: SLG/Mo/graded CIGSeS/CdS/i:ZnO/ZnO:Al/Cr/Ag/MgF₂.

3.3 CIGSeS thin film solar cells testing and characterization

3.3.1 I-V testing

FSEC PV Materials Lab has developed a reliable, fairly accurate and robust current-voltage (I-V) measurement setup. The setup consists of a wooden box where the solar cells were illuminated with AM 1.5 illumination (100 mW/cm^2). High-accuracy power supply and multimeters were procured to forward and reverse bias the solar cell and to measure current readings. A LabVIEW program was developed to measure and plot the I-V characteristics.

I-V measurements were carried out both in the dark and with light. Dark I-V analysis was carried out to obtain values of the fundamental parameters such as reverse saturation current density (J_0) and diode quality factor of the solar cell as a p-n junction or the diode. Analysis of light I-V characteristics of CIGSeS/CdS thin film solar cells was carried out

to obtain the relevant photovoltaic parameters: open circuit voltage (V_{oc}), short circuit current density (J_{sc}), series resistance (R_s), shunt resistance (R_p) and fill factor (FF).

The final and official I-V measurements of CIGSeS/CdS thin film solar cells were carried out at NREL for authentication. The cells that gave >10% efficiency in the lab were sent to NREL for I-V measurements under simulated AM1.5 conditions at 25°C.

3.3.2 Materials and Electrical Characterization

Films were examined visually for their appearance, color and any tendency to peel. Materials characterization of these films was done by optical microscopy, SEM, EDS, XRD, AES, and EPMA. X-ray diffraction (XRD) was used to identify the crystalline phases. Surface morphology was studied using scanning electron microscopy (SEM). Chemical composition was analyzed by electron probe microanalysis (EPMA) and Energy dispersive spectroscopy (EDS). Depth profiling was performed by Auger electron spectroscopy (AES). Thickness was measured using a profilometer.

Extensive electrical characterization was carried out on these CIGSeS thin film solar cells by current-voltage, quantum efficiency and capacitance-voltage measurements and light beam induced current (LBIC) techniques. Short-circuit current density (J_{sc}) versus voltage (V) curves were obtained at various temperatures, and capacitance-voltage analysis was carried out at room temperature.

3.3.3 Diode parameters analysis

An analysis of diode parameters was carried out. Such analysis is very useful in designing future experiments for rapid thermal processing of CIGSeS thin film solar cells.

3.4 Experimental work for CIGS2 cells band-offset measurement

In order to achieve an optimal overlap with the solar spectrum, Cu(In,Ga)S₂ (CIGS2) thin-film solar cells would be more favorable as compared to CIGS cells due to band gap of CIGS2 which is 1.5 eV or higher depending upon gallium content. Efficiencies of cells based on CIGS2 are presently limited to below 13% [99]. The main reason is that the expected linear gain in the open circuit voltage (V_{oc}) compared to that of CIGS could not be achieved so far. The origin of this behavior is not understood. Several models suggest that this is caused by a non-ideal conduction band offset (CBO) at the interface between the CIGS absorber and the commonly used CdS heterojunction partner layer. Therefore, experiments were carried out to obtain band-offset values at CIGS2/CdS interface as explained in the following.

Molybdenum back contact and the metallic precursors of indium and copper–gallium (CuGa) were sputter deposited by DC magnetron sputtering. The metallic precursors were sulfurized at 475°C in 4% H₂S/Nitrogen gas mixture to obtain copper-indium-gallium disulfide (CIGS2) thin films with Cu-excess. For the purpose of analysis samples were categorized according to the treatment. Samples after sulfurization treatment were categorized as unetched (SSUn). Samples that were etched in 10% KCN solution for 3 min were labeled etched (SSE). Samples that were etched and oxidized in 50/50 solution of 5% H₂SO₄ and H₂O₂ [100] were labeled treated (SSEO). CdS layer was deposited over the unetched, etched and treated samples to create an interface. Ultra thin, approximately 5 nm layer of discontinuous CdS layer was deposited using chemical bath deposition. For the band offset measurements, three samples with varying CdS thickness were prepared, ranging from approximately 5 nm to a film thickness as used in real devices (~50 nm).

All samples were investigated by ultraviolet photoelectron spectroscopy (UPS) with He I and He II excitation, by X-ray Photoelectron Spectroscopy (XPS) with a Mg K α X-ray source, and by Inverse Photoemission Spectroscopy (IPES). The Photoemission Spectroscopy (PES) spectra were recorded with a VG CLAM four electron analyzer. For the IPES experiments, a Cicacci type electron gun and a dose-type detector with SrF₂ window and Ar:I₂ filling were used. All experiments were performed in ultra high vacuum with a base pressure below 5×10^{-10} mbar. Initial experiments for achieving thin layer of CdS were carried out on CIGS2 thin films on sodalime glass and as well as on SS substrates. The samples were analyzed with Auger electron spectroscopy. CdS layers of various thicknesses were deposited by starting with the bath at room temperature placed in a heated bath and carrying out chemical bath deposition process for different times reaching different maximum bath temperatures. The AES data presented here is for a sample on which ~ 5 nm CdS was deposited for a period of 3 min and 55 s reaching the maximum bath temperature of 52°C. Thickness of CdS films was measured by Auger electron spectroscopy at the University of Florida, Gainesville while the photoelectron spectroscopies were carried out at the Universität Würzburg, Germany.

CHAPTER 4 RESULTS AND DISCUSSION

4.1 Preparation of CIGSeS thin films of the required composition and semiconducting properties.

4.1.1 Deposition of DC magnetron sputtered copper-gallium and indium metallic precursor films having required thickness and Cu/(In+Ga) ratio

Experimental series: A precursor film of copper gallium was sputtered from a copper-gallium alloy target having 22 atomic % gallium. The sputtering parameters were power of 350 Watt at Ar pressure of 1.5×10^{-3} Torr. Indium was deposited from an indium target at power of 230 Watt at Ar pressure of 7×10^{-4} Torr, on a 10 cm x 10 cm Mo coated sodalime glass substrate. The thickness of these precursors was measured and the sputtering process was calibrated.

Results and discussion: From these experiments the sputtering parameters i.e. power, pressure and timing were determined so as to obtain copper gallium indium metallic precursor films of required Cu/(In+Ga) ratio in the range of 0.85 to 0.95 and a thickness of ~0.7 micron.

4.1.2 Device quality CIGS film formation by RTP

Experimental series I: After depositing metallic precursor films, the next step was compound formation. CIGSeS compound was formed by depositing selenium onto the precursor film by vacuum evaporation through joule heating and then heating the

complete stack of copper gallium indium and selenium films in RTP chamber at 550°C for various timings in the presence of H₂S gas and ultra high purity nitrogen. As the vapor pressure of selenium is high, selenium is lost during compound formation by RTP. Hence an excess of selenium above the stoichiometric quantity was deposited during vacuum evaporation [87]. To begin with 1.4 times the required stoichiometric selenium was deposited. And the films were selenized at 550°C for 6 minutes. The resulting CIGS films were fairly conducting having sheet resistance value in the range of 40-250 Ω per square. The composition of these films was analyzed by EDS, shown in Figure 22. The EDS analysis showed, average atomic concentrations of Cu:In:Se in proportions of 24.18:35.14:40.69. As it can be seen from EDS data, the films were selenium poor having ~40 atomic % selenium.

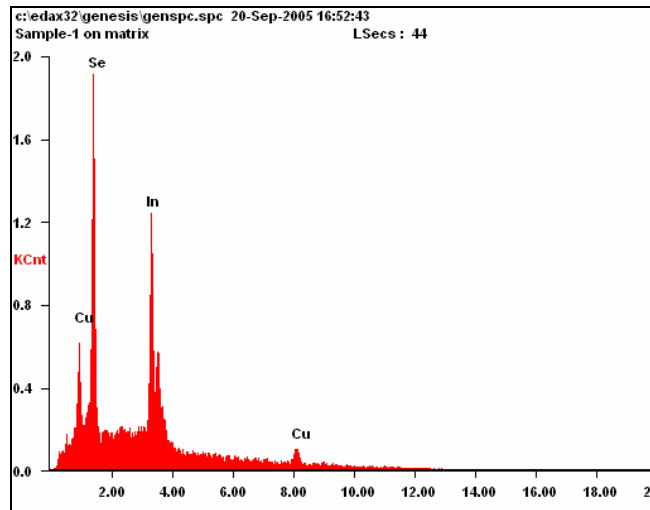


Figure 22: EDS data of CIGS film

It is important to note that there is no gallium is detected in this case and in general there is less gallium detected on the surface of the final reacted compound film. This result is explained by the segregation of Ga to the Mo back contact during the high temperature

reaction process, which results in an underestimation of the gallium amount on the film surface by surface sensitive EDS measurements.

Experimental series II: In the next set of experiments, the amount of selenium was increased to 1.6 times the stoichiometric quantity, and the films were selenized at 550°C for 4 minutes as it was thought that 6 minutes is more than sufficient time for selenization of these films. In the earlier experiments, the sheet resistance of the sample was observed to be very low. It was suspected that there was an extreme loss of Se in the form of In_2Se_3 . In order to ensure proper intermixing of the metallic precursors i.e. CuGa and In, they were deposited in the form of a few alternating layers, which were designed to obtain a Cu/(In+ Ga) ratio of approximately 0.95. It was speculated that due to more time at higher temperature, selenium may evaporate from the films and the resulting films would be selenium deficient. The resulting CIGS films from this experimental series were still conducting even though the conductivity decreased as compared to the earlier CIGS films selenized with 1.4 times stoichiometric selenium. These films showed sheet resistance value in the range of 250-500 Ω per square. The composition of the film was analyzed by EDS. The EDS analysis showed, average atomic concentrations of Cu:In:Ga:Se in proportions of 21.32:28.99:5.06:42.69. As it can be seen from EDS data, the films were selenium poor having ~42.5 atomic % selenium. Even though more than earlier films, selenium quantity is still less than the required value of 50 atomic % selenium. The EDS spectrum is shown in Figure 23.

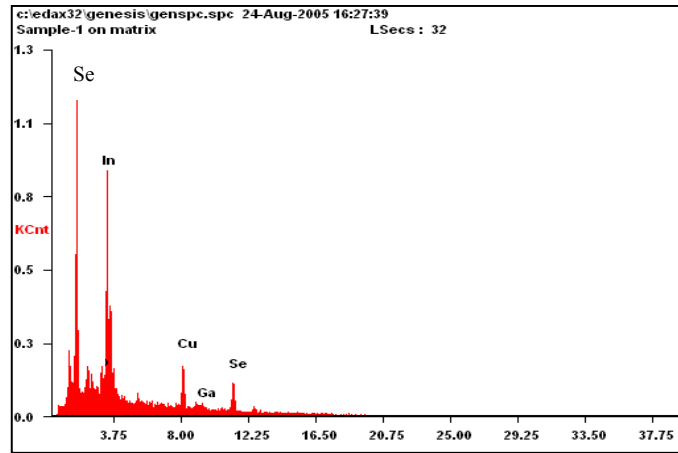


Figure 23: EDS spectra of selenium poor CIGS sample

Scanning electron microscopy was carried out to study the morphology and the results are shown in Figures 24 and 25.

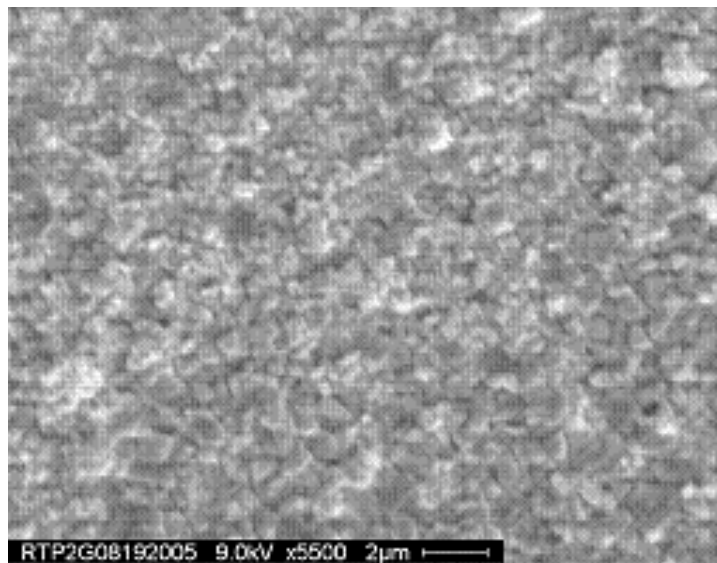


Figure 24: SEM of selenium poor CIGS film

The SEM micrograph in Figure 24 shows that the grains are not clearly distinguished and are not faceted.

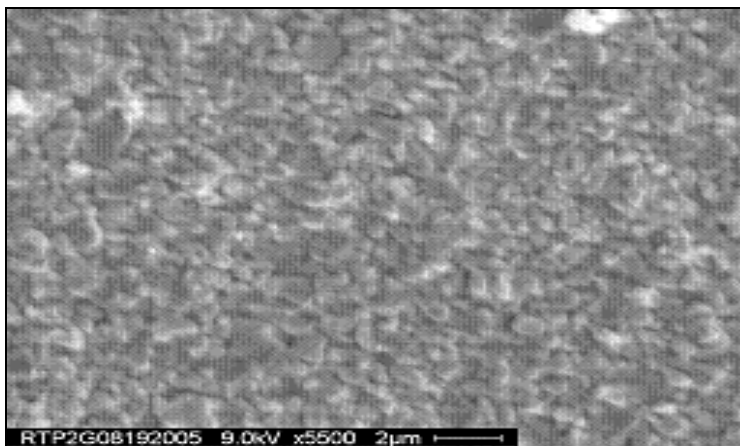


Figure 25: SEM of selenium poor CIGS film

The SEM micrograph in Figure 25 obtained from the same film at a different location shows that the grains can be distinguished better and are partially faceted.

Experimental series III: Based on the results of these experiments, new experiments were designed and carried out to enhance the amount of selenium in the CIGS films. For this purpose, the amount of evaporated selenium was increased to 2 times the stoichiometric composition, and during RTP compound formation step, the time at the maximum temperature was reduced further from 4 minutes to 2 minutes, to reduce amount of selenium loss. The films exhibited sheet resistance value in the range of 10-15 k Ω per square. The composition of the film was analyzed by EDS, shown in Figure 26. The EDS analysis showed, average atomic concentrations of Cu:In:Ga:Se in proportions of 24.46:26.64:3.31:45.59. As it can be seen from EDS data, ~45.5 atomic % selenium was present in the film.

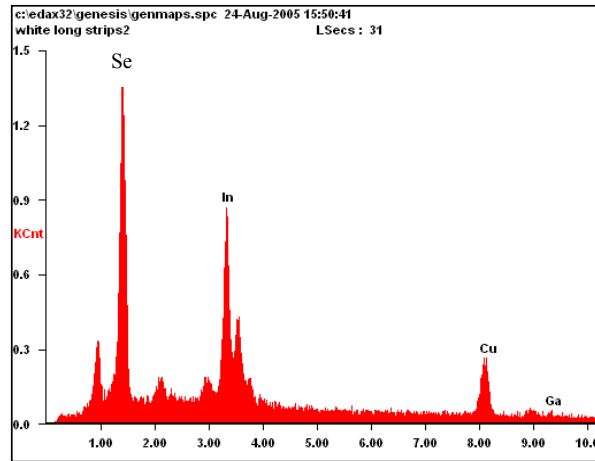


Figure 26: EDS spectra of CIGS film

Even though the amount of selenium observed in this film was less than the ideal stoichiometric composition, it was considered to be adequate as during further steps sulfurization of the films was also planned, and partially selenized films are easier to sulfurize as compared to completely selenized films.

Experimental series IV: The quantity of selenium was further increased by decreasing the selenization time to 1 minute 30 seconds at 550°C instead of 2 minutes used in earlier experimental series so as to enhance the amount of selenium in the CIGS films to 50 atomic % films and these CIGS films were used for completion of cells. The EDS data is provided in Figure 27. XRD analysis was also carried out and the results are shown in Figure 28. The XRD pattern revealed all the main chalcopyrite reflections with no evidence of binary phases, which indicates that a stable fully reacted chalcopyrite structure was formed. The position of the (112) reflection at 26.64° [$d(112) = 0.334$ nm] closely represents the lattice parameter of pure CuInSe_2 . The EDS analysis showed, average atomic concentrations of Cu:In:Se in proportions of 22.92:26.86:50.21. As it can be seen from EDS data, the films had more than 50 atomic % selenium. Cells were

completed on these CIGS films by procedure mentioned in chapter 3 Experimental Technique.

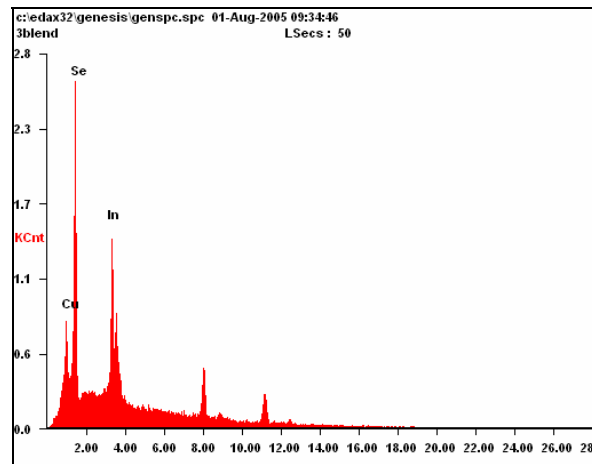


Figure 27: EDS spectra of CIGS film

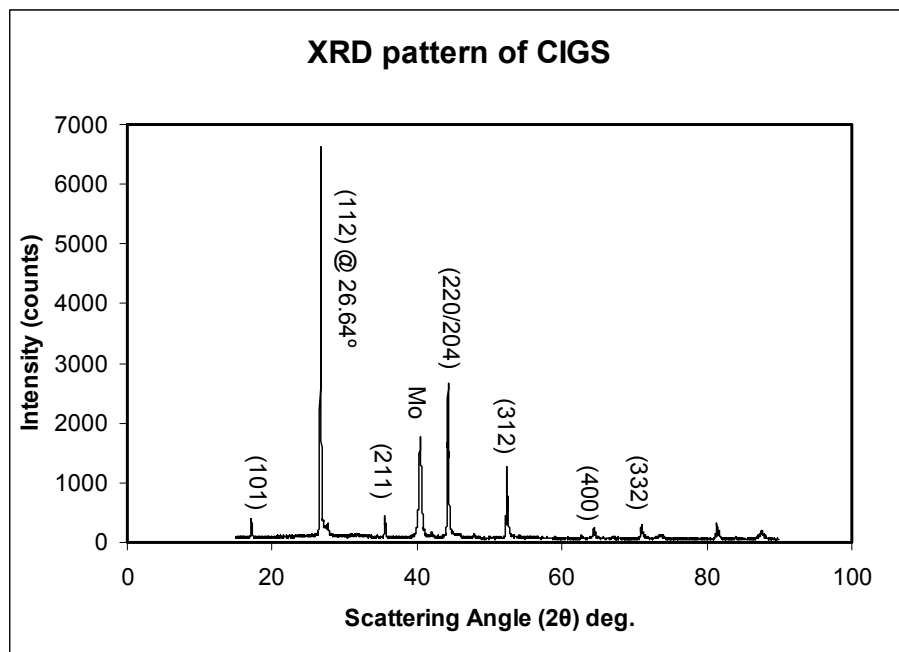


Figure 28: XRD pattern of CIGS

Results and discussion: Cells were completed on these films by deposition of CdS heterojunction partner layer, i-ZnO/ZnO:Al window bilayer, Cr/Ag contact fingers.

These cells were then analyzed for photovoltaic parameters in simulated AM 1.5 spectrum using in house built set-up. The CIGS cells showed current density in the range of 20-30 mA/cm² while the open circuit voltages were lower in the range of 300 to 400 mV and the fill factors were in the range of 40 to 50%, and the overall efficiency was in the range of 3 to 4%. The selenization parameters were thus finalized to deposition of 2 times stoichiometric selenium and 2 minutes at 550°C during RTP for CIGS formation. After obtaining device quality CIGS films by RTP selenization, the next step for enhancing the device performance was sulfurization of the CIGS films.

4.1.3 Sulfur incorporation in CIGS films by RTP to improve the semiconducting properties and device performance.

Experimental series: The objective of this experimental series was to incorporate sulfur into the surface of CIGS film to get CIGSeS films. As explained earlier, in the two stage process most of the gallium diffuses towards the molybdenum back contact and therefore, less amount of gallium is present near the surface of the CIGS film. Due to this, the band gap of the CIGS film reduces near the surface, and thus in the space charge region of the cell. Sulfur incorporation is carried out for the purpose of increasing the band gap near the surface, resulting in a double-graded film. Sulfur also reduces the deep trap states in the absorber [89] and passivates the defects.

For sulfur incorporation in the CIGS absorber surface, a mixture of H₂S and ultra high purity nitrogen is used as a process gas mixture. At high temperature, sulfur is formed due to pyrolysis of H₂S gas and diffuses into the partially selenized CIGS film surface.

Initially, sulfurization time was kept 4 minutes at 550°C. The composition of the films was analyzed by EDS.

Results and discussion: Cells were completed on these films by deposition of CdS heterojunction partner layer, i-ZnO/ZnO:Al window bilayer, Cr/Ag contact fingers. Photovoltaic parameters of these cells were measured under simulated AM 1.5 spectrum using in-house built I-V measurement set-up. The resulting parameters shown in Figure 29 (in fourth quadrant) and Table 2 were as follows: V_{oc} of ~590 mV, J_{sc} of ~16 mA/cm², FF of ~41% and efficiency of ~4%.

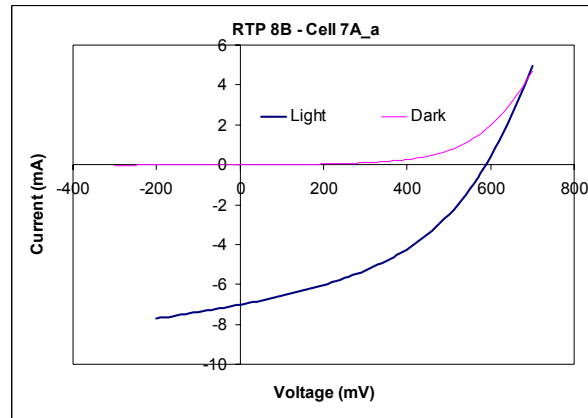


Figure 29: I-V characteristics for CIGSeS solar cell processed by RTP

Table 2: Device parameters for the cell processed by RTP

Parameter	R_{sh}	R_s	Area	J_{sc}	V_{oc}	% FF	% η
Value	279 Ω	32 Ω	0.441 cm ²	16 mA/cm ²	590 mV	41.24	3.87

As can be seen from these results, the open circuit voltage (V_{oc}) of the cells was improved significantly due to incorporation of sulfur. However, the short circuit current density (J_{sc}) value has been reduced as sulfur diffused till significant depth into the film and the overall band gap of the absorber increased, photons below this bandgap are not absorbed into the film reducing the photocurrent. The average atomic composition of these films as analyzed by EPMA was as follows: Cu:In:Ga:Se:S of

24.24:19.28:6.92:27.05:22.48, from the EPMA analysis Cu/(In+Ga) was calculated to be 0.92.

AES Depth profile of these CIGSeS films was also carried out. Composition-depth profile is shown in Figure 30. XRD data of these films is shown in Figure 31.

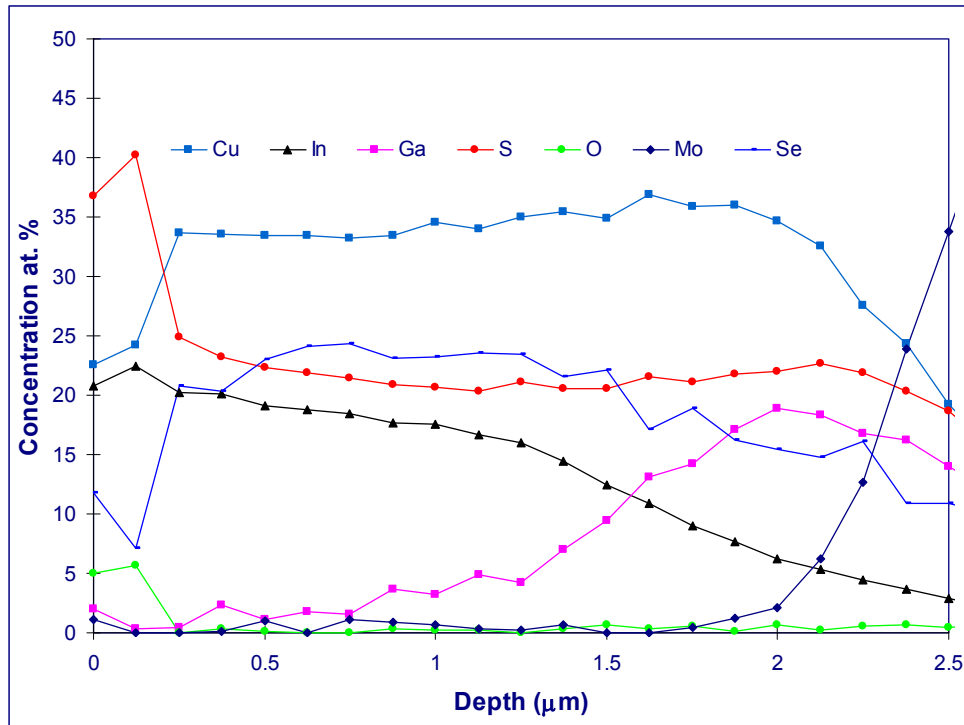


Figure 30: AES depth profile of CIGSeS film

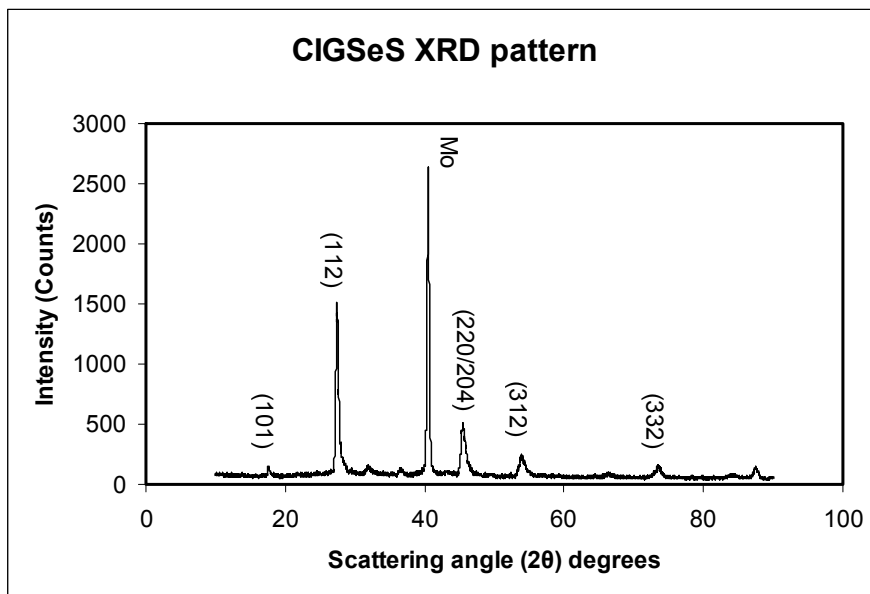


Figure 31: XRD pattern of CIGS showing (112) peak at 2θ angle 27.44 degrees

EPMA data (from NREL) as well as AES depth profile data for this selenized and sulfurized sample showed sulfur content (~ 20 atomic %) which is higher than the desired. Hence the next logical step was to combine selenization and sulfurization to have a better control over CIGSeS film properties and resulting increase in the device performance. XRD pattern of the CIGSeS film shows chalcopyrite structure, with the peak position of (112) shifted to higher angle 27.44° due to higher amount of sulfur incorporation.

4.1.4 Preparation of graded CIGSeS absorber films by selenization/sulfurization in RTP.

Experimental series I: The objective for these experiments was to form a compositionally graded CIGSeS absorber film to ensure band gap grading and improve the device performance, by keeping the short circuit current density (J_{sc}) values high as seen in sub-section 4.1.2 and simultaneously obtaining higher open circuit voltage (V_{oc}) values as seen during the results in sub-section 4.1.3.

Several experiments were carried out by changing the sulfurization times. In an experimental run, selenization time of 2 minutes was used and then the film was sulfurized for 1 minute, thus reducing the sulfurization time of 4 minutes used in earlier experiments to ensure that the surface diffusion is restricted only in the surface region of the absorber film and not in the bulk of the absorber. Films were examined visually for their appearance, color and any tendency to peel. Surface morphology of the CIGSeS thin film was studied using scanning electron microscopy (SEM). Chemical composition was analyzed by electron probe microanalysis (EPMA). Depth profiling was performed by Auger electron spectroscopy (AES). Thicknesses of thin films were measured using a thickness profilometer. Current–voltage (I-V) characteristics of CIGSeS solar cells were measured under AM1.5 spectrum using a set-up developed at the FSEC PV Materials Lab and then a few chosen samples were sent to NREL for I-V and QE analysis.

The SEM image of a near-stoichiometric, etched CIGSeS thin film is shown in Figure 32 and a cross-sectional SEM image of the same thin film is shown in Figure 33. The sample showed well-faceted grains of approximately 1 μm size.

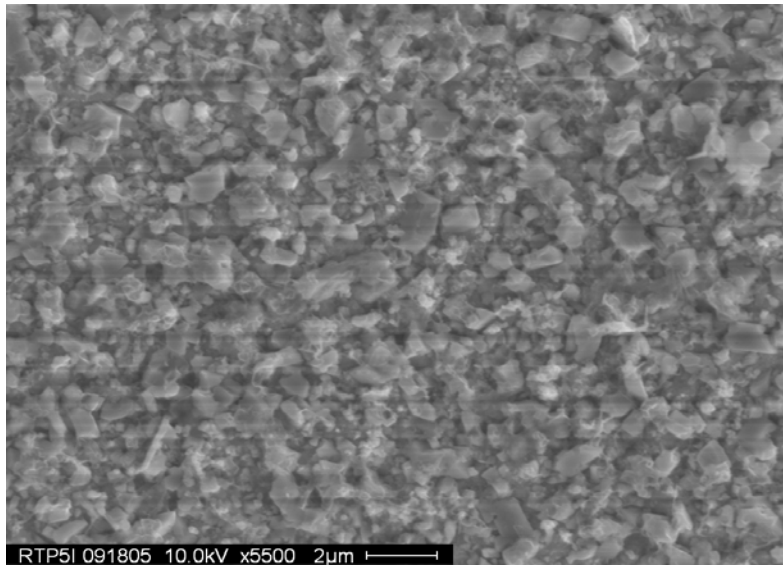


Figure 32: SEM image of a near-stoichiometric, KCN etched CIGSeS thin film at 5500X

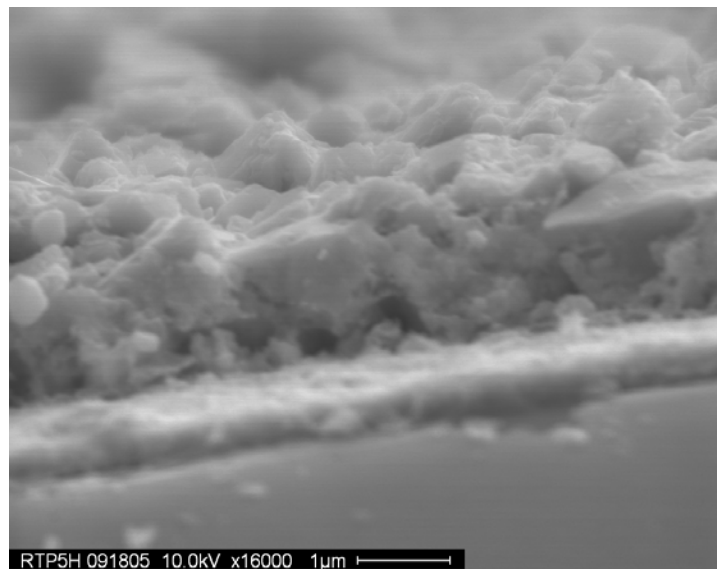


Figure 33: Cross sectional SEM image of a near stoichiometric, etched CIGSeS thin film at 16000X

Atomic force microscopy of CIGSeS films has been carried out. Figures 34 and 35 show AFM analysis of CIGSeS films fabricated by RTP.

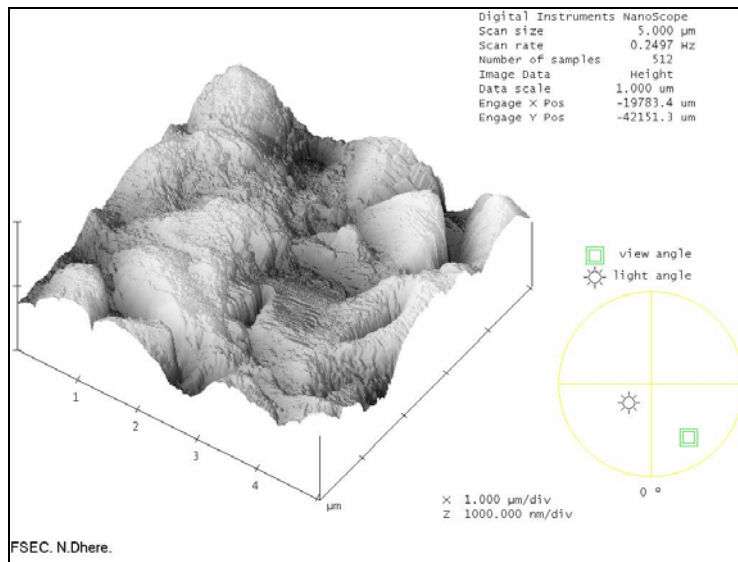


Figure 34: AFM three dimensional profile of CIGSeS sample fabricated by RTP.

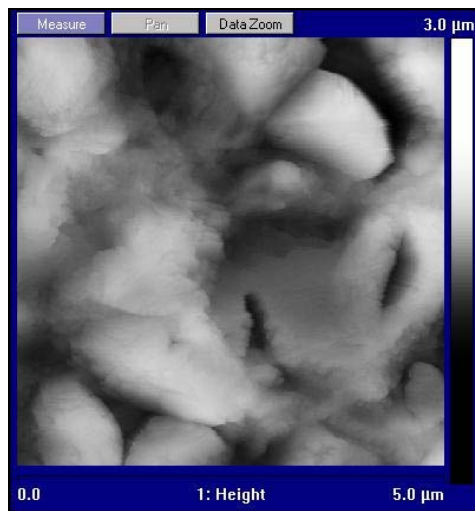


Figure 35: AFM surface image of the surface of CIGSeS sample fabricated by RTP.

Surface topography of CIGSeS films is revealed by the AFM image. Grain size of ~1 to 2 microns can be seen. Relatively rough surface, typical of two-stage processed films, can be seen from the three dimensional AFM profile.

Results and discussion: Cells were completed on these films by deposition of CdS heterojunction partner layer, i-ZnO/ZnO:Al window bilayer, Cr/Ag contact fingers. The current-voltage characteristics were measured under simulated AM 1.5 spectrum using a I-V setup built in-house at the FSEC PV Materials Lab. Efficiencies of ~ 9% (total area efficiency) were observed. These efficiency results were without the application of anti-reflection coating. Current-voltage curve is shown in fourth quadrant in Figure 36 and Table 3.

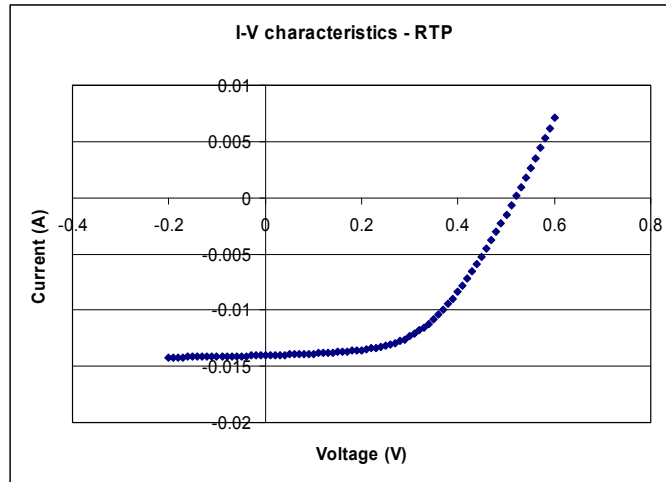


Figure 36: Current-Voltage characteristics of CIGSeS solar cell prepared by RTP

Table 3: I-V data of CIGSeS absorber from RTP process

Parameter	R_{sh}	R_s	Area	J_{sc}	V_{oc}	% FF	% η
Value	694 Ω	13.41 Ω	0.441 cm^2	31.81 mA/cm^2	520 mV	52.2	8.63

Additional experiments were carried out for the preparation of CIGSeS absorbers. MgF_2 anti-reflection coatings were applied to cells with comparatively higher efficiencies. These cells were then sent to NREL for I-V and QE measurements. Encouraging results

were obtained surpassing the 10% efficiency for these cells. The current-voltage and quantum efficiency measurements are shown in Figures 37 and 38.

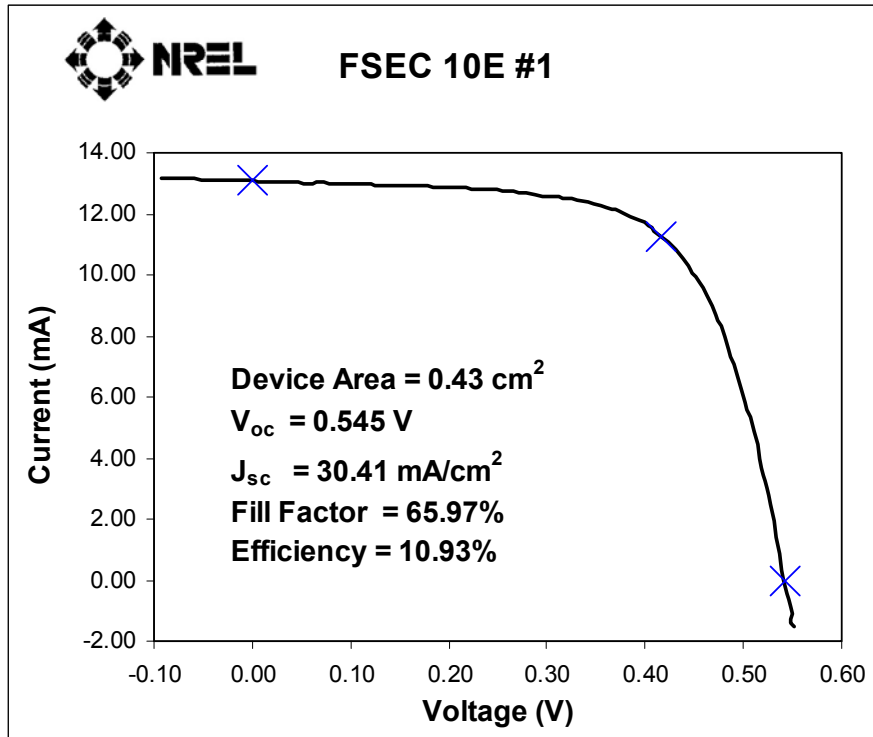


Figure 37: IV Characteristics of cell 10E#1

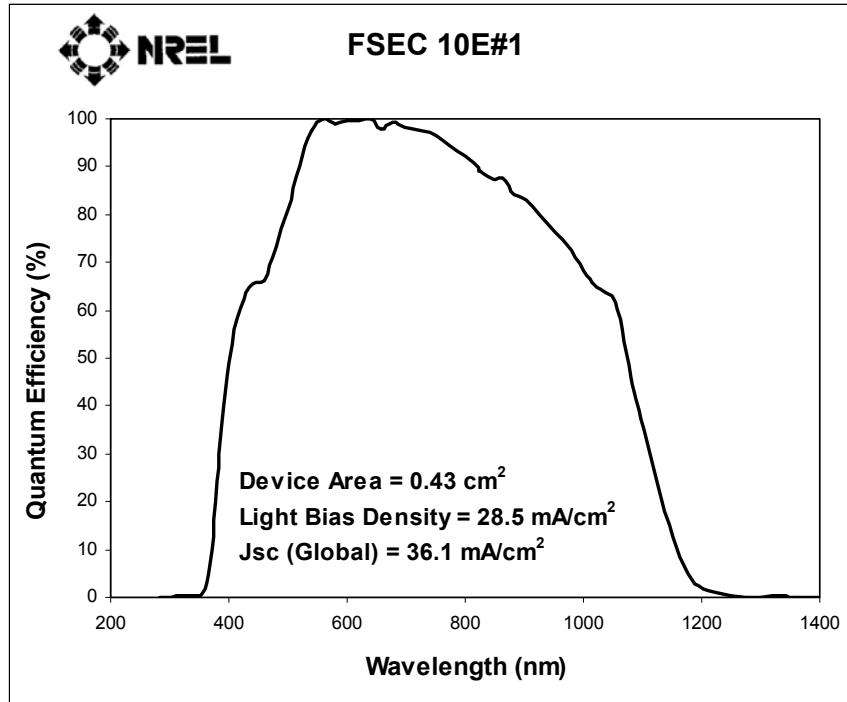


Figure 38: QE analysis of cell 10E

The cell parameters were as follows, $V_{oc} = 545$ mV, $J_{sc} = 30.41$ mA/cm², $FF = 65.97\%$ and $\eta = 10.93\%$, as can be seen from these results open circuit voltage (V_{oc}) value has improved keeping the photocurrent value also relatively high. Efficiency of CIS is known to be improved by bandgap widening through addition of Ga and S. Gallium improves open circuit voltage (V_{oc}). However, Ga is not found in the depletion region at the front. The accumulation of Ga at the back creates a back surface field [90]. The back surface field helps in improving solar cell performance. Sulfur is present at the surface and near the molybdenum contact. I-V data shows open circuit voltage (V_{oc}) of 544 mV, through the increase of bandgap in the depletion region and the passivation of defects [90]. Thus the RTP process results in double bandgap grading. The QE of the cell shows that the higher energy photons are contributing more effectively to light generated current as compared to lower energy photons. This shows that the electron-hole pairs generated

deep in the absorber, i.e. bulk of the absorber are not getting separated effectively by the electric field. This effect can be attributed to relatively small grain size near the molybdenum contact, reducing the diffusion length. The QE response to lower energy photons can be improved by improving the quality of the absorber, i.e. by increasing the grain size near the molybdenum back contact, and by passivating the defects.

From these results it was felt that open circuit voltage (V_{oc}) values can be improved further, and so additional experiments were designed to optimize the sulfurization time.

Experimental series II: After getting encouraging results i.e. efficiencies above 10%, these experiments were designed to optimize sulfur diffusion into the CIGSeS absorber surface to increase open circuit voltage (V_{oc}) values. Several experiments were carried out with selenization time of 2 minutes and sulfurization time of 2 minutes, instead of one minute sulfurization time used in earlier experimental series. Cells were completed from these CIGSeS films and tested under simulated AM 1.5 spectrum at NREL.

Results and discussion:

The current-voltage and quantum efficiency measurements are shown in Figures 39 and 40.

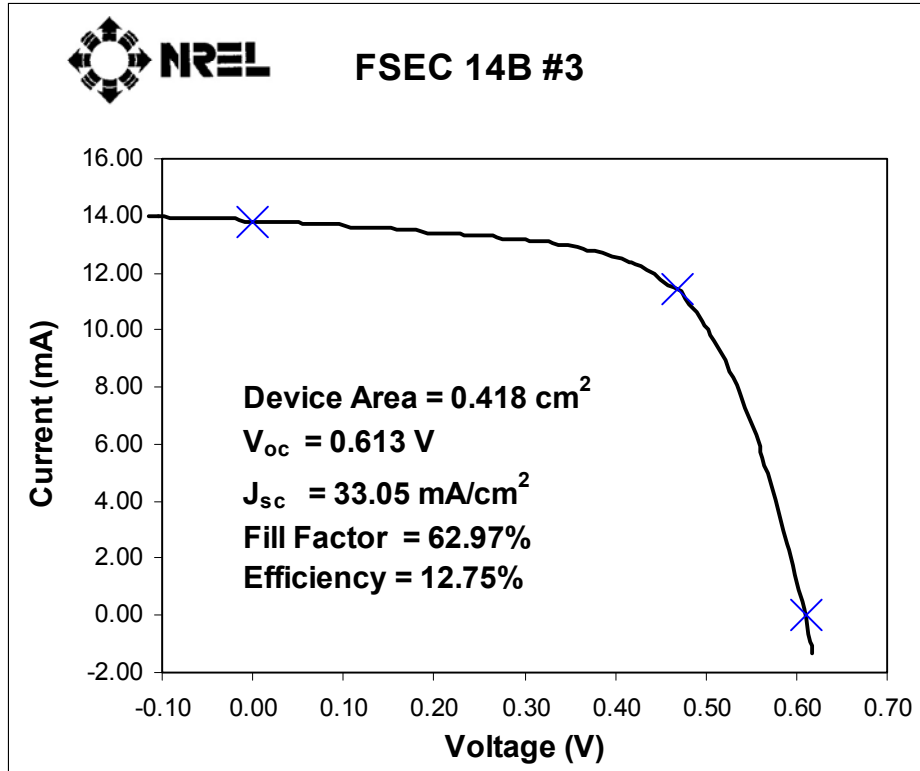


Figure 39: IV Characteristics of cell 14B#3

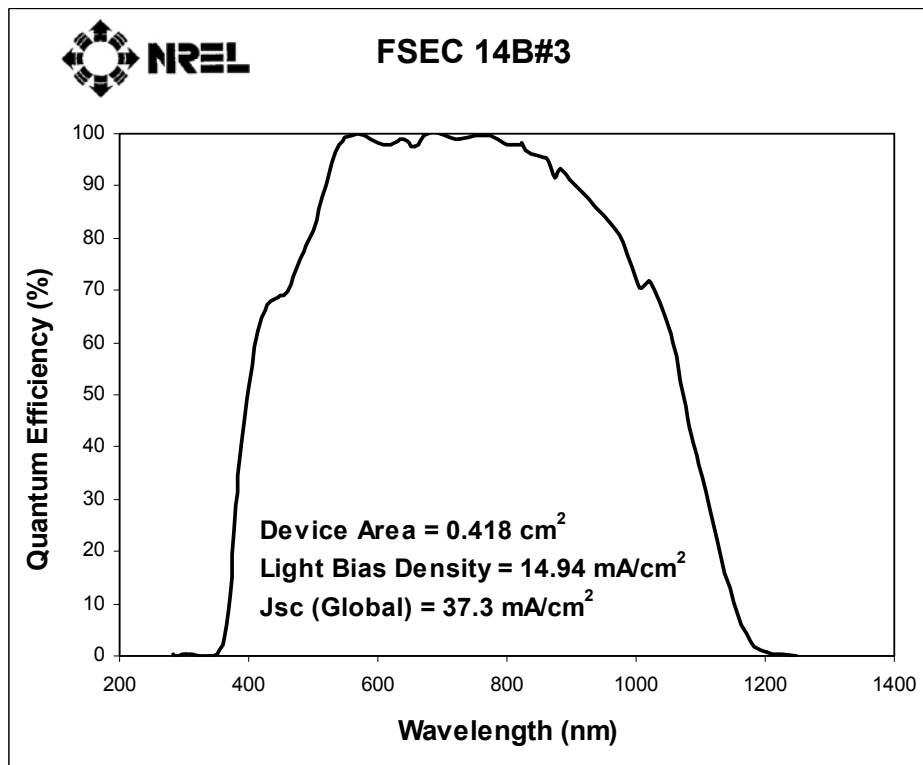


Figure 40: QE analysis of cell 14B

The results confirmed that the approach of using higher sulfurization time is working and the cell parameters were as follows, $V_{oc} = 613$ mV, $J_{sc} = 33.05$ mA/cm², FF = 62.97% and $\eta = 12.75\%$, as can be seen from these results open circuit voltage (V_{oc}) value has been further improved and short circuit current density (J_{sc}) value has also been improved simultaneously. Thus it was confirmed that the sulfur incorporation approach is working and films with better properties can be synthesized. Another interesting observation in the results is the reduction of fill factor from $\sim 66\%$ to 63% in these cells.

The AES depth profile analysis of these films was carried out and the results are as shown in Figure 41.

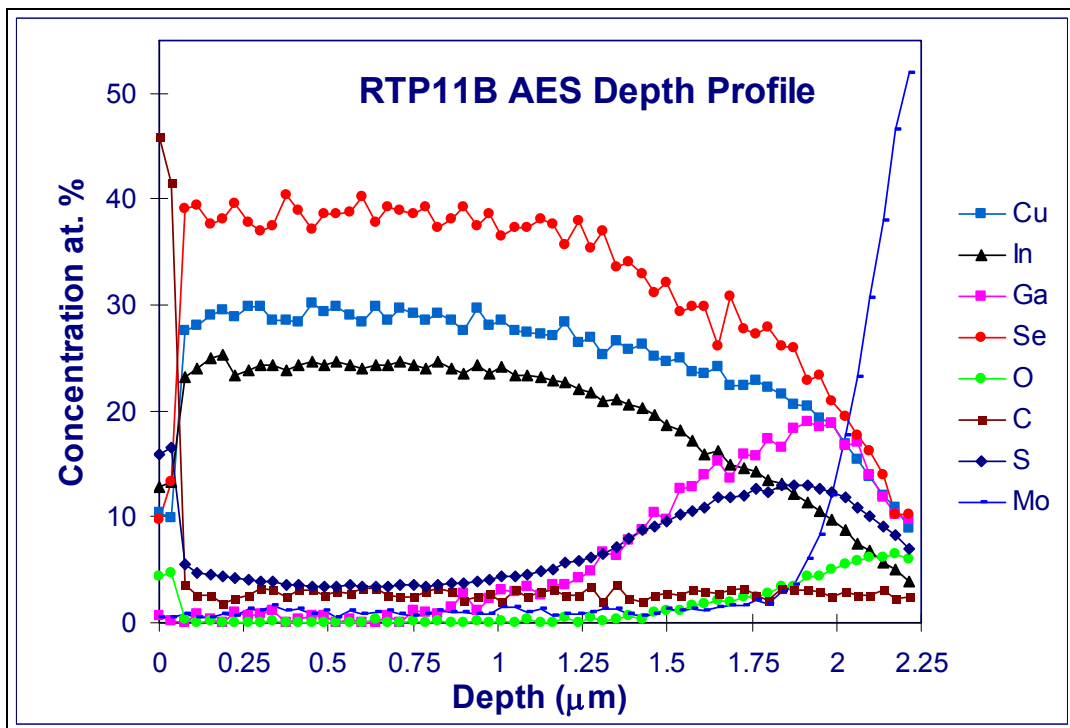


Figure 41: AES depth profile of near-stoichiometric, etched CIGSeS thin film

An AES survey (Figure 41) of a near-stoichiometric, etched CIGSeS thin-film sample was performed using a primary electron beam of energy 20 keV. The AES depth profile was obtained by sputtering with energetic argon ions at a rate of 500Å/min. The depth profile showed that gallium concentration increases towards the back contact while that of indium decreases.

These results confirmed a non-uniform distribution of elements within CIGSeS thin films, i.e. an enrichment of sulfur towards the surface and gallium/sulfur towards the Mo back contact.

Post sulfurization reduces defects and increases the bandgap at the junction. Sulfur diffusion through grain boundaries is higher as compared to sulfur diffusion through grains; therefore, higher concentration of sulfur was observed near the surface and at Mo back contact interface where the grain size is smaller [91]. Small grains at Mo interface are also evident in the cross-sectional SEM image (Figure 33). After analysis of the AES depth profiles of these films it was noticed that sulfur concentration near the molybdenum back contact is relatively high. The sulfur rich region in the back of the film has a lower valence band as compared to the region in the bulk having relatively less sulfur. The lowering of the valence band into this region near the molybdenum back contact can create a barrier to the hole diffusion at the interface of back contact. This can explain the slightly reduced fill factor of these cells, even though they are having comparatively higher open circuit voltage (V_{oc}) and short circuit current density (J_{sc}). So the next series of experiments was designed to reduce this impact of sulfur near the molybdenum back contact, and regain the fill factor values.

At high temperature, reaction of sulfur with molybdenum to form MoS₂ is enhanced, leading to formation of more MoS₂. MoS₂ has higher resistivity as compared to that of MoSe₂. This may also one of the reasons of increase in the series resistance of the cell and reduction of the fill factor [92].

4.1.5 Fine tuning the graded CIGSeS absorber film properties for improving the optoelectronic device performance

Experimental series: These experiments were carried out to fine tune the quantity of sulfur near the back contact. This is done by slightly reducing the sulfurization time. Experiments were carried out with selenization time of 2 minutes and sulfurization time of one minute and 30 seconds, instead of two minutes sulfurization time as done in the earlier experimental series. Cells were completed from these CIGSeS films and tested under simulated AM 1.5 spectrum at NREL.

Results and discussion:

Figure 42 shows energy dispersive spectroscopy (EDS) spectra of the CIGSeS film surface at 20 KV. The EDS analysis showed, average atomic concentrations of Cu:In:Se:S in proportions of 23.11:26.44:80:5.77. As can be seen from the EDS data the Cu/In ratios is 0.88 and S/(Se+S) ratio is approximately 0.11.

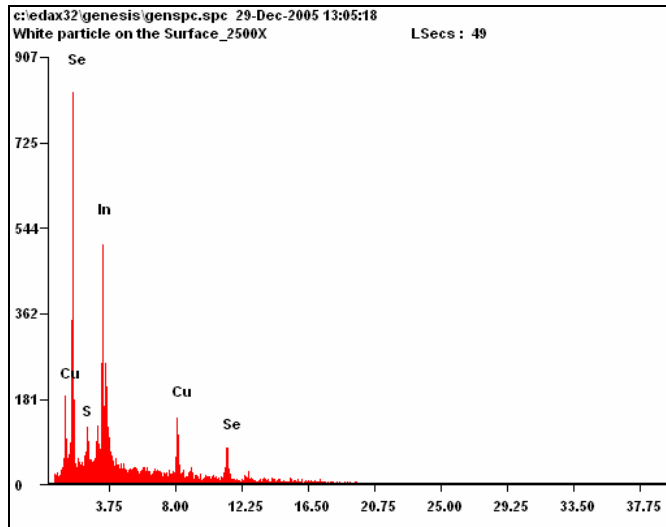


Figure 42: EDS spectra of CIGSeS thin film surface at 20KV

The chemical composition of CIGSeS films was analyzed by EPMA. Average atomic concentrations of Cu:In:Ga:Se:S measured at 20 kV for an etched sample was Cu:In:Ga:Se:S to be in proportion of 22.97:24.90:2.41:43.57:5.4 This data showed Cu/(In+Ga) ratio to be approximately 0.84 and S/(Se+S) ratio to be approximately 0.11. It is important to note that the measured gallium mole fraction of the final reacted pentenary alloy [$x = \text{Ga}/(\text{In}+\text{Ga})=0.08$] is well below that of the expected precursor value in the range of ~ 0.18 to 0.22 . This result is explained by the segregation of Ga to the Mo back contact during the high temperature reaction process, which results in an underestimation of the Ga/(In+Ga) molar fraction by surface sensitive EDS measurements.

AES depth profile was carried on these CIGSeS films and the results are shown in Figure 43.

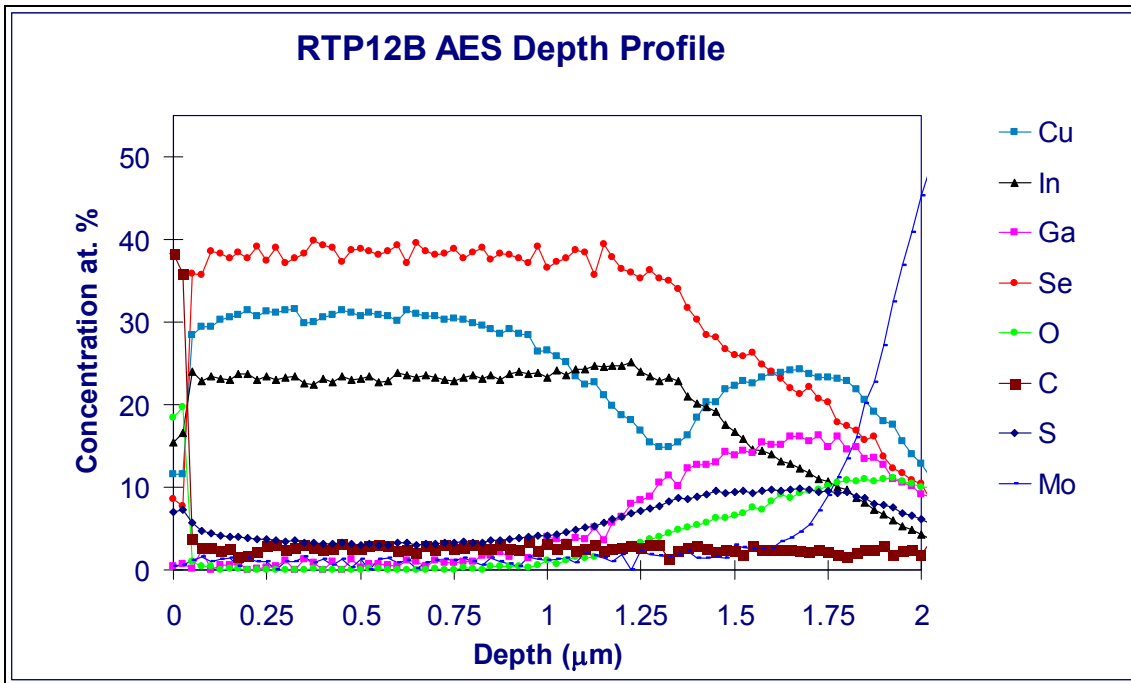


Figure 43: AES depth profile of a CIGSeS film

From the analysis of the AES depth profiles of these films it was noticed that sulfur concentration near the molybdenum back contact as well as at the surface is reduced as compared to earlier AES depth profile in Figure 41, as the sulfurization time was reduced. XRD data of these films is shown in Figure 44.

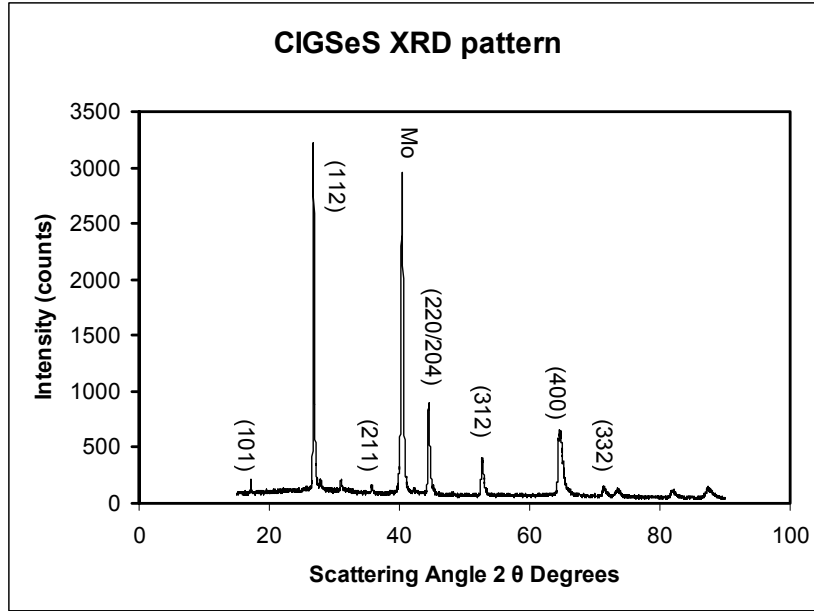


Figure 44: XRD of selenized/sulfurized film

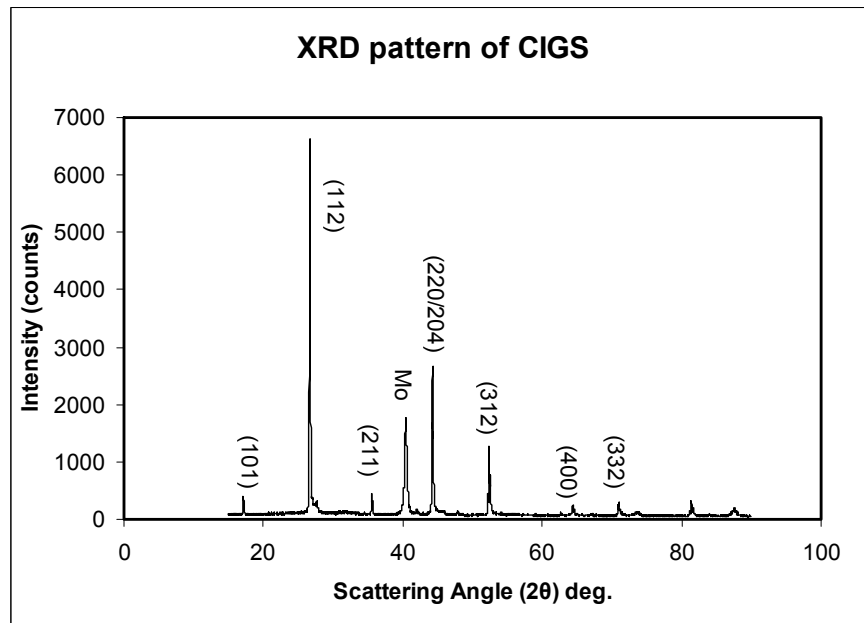


Figure 45: XRD of selenized (CIGS) film

XRD profile of only selenized film is shown in Figure 45, assuming gallium profile remains the same, 112 peak at 2θ scattering angle of 26.8 corresponds to 6 atomic % sulfur [93] [94], which confirms well with the EPMA and EDS data.

From the XRD analysis following parameters were calculated: lattice parameter $a = 5.758$ Å and $c = 11.516$ Å of the chalcopyrite phase of CIGSeS, giving c/a ratio of 2.000. Intensity ratio of (112) peak to (220/204) peak is ~ 3.3 , indicating (112) preferred orientation.

Figure 44 depicts XRD pattern (Cu $K\alpha$ radiation) of the CIGSeS film. The XRD pattern taken from the film after the selenization step (Figure 45) revealed all the main chalcopyrite reflections with no evidence of binary phases, which indicates that a stable fully reacted chalcopyrite structure was formed. The position of the (112) reflection at 26.64° [$d(112) = 0.334$ nm] closely represents the lattice parameter of pure CuInSe_2 . After sulfurization, the (112) reflection shifted to slightly higher angles around 26.8° [$d(112) = 0.328$ nm], most probably due to a shrinkage of the lattice after Ga and/or S incorporation into the bulk of the alloy. It is also important to note the compositional broadening of the characteristic peaks due to the grading of Ga and/or S through the absorber thickness after the high temperature reaction steps. The in-depth compositional uniformity of the samples was assessed in more detail by grazing incidence X-ray diffraction (GIXRD). Figure 46 and 47 show GIXRD pattern at 0.5° and 1° respectively, for resulting compositionally graded CIGSeS sample. In GIXRD, a decrease in the x-ray incidence angle results in a decrease in the penetration depth of the x-rays and hence scattering volume. Low diffracted beam angles thus represent information from the top surface region of the alloy, while higher angles represent the information of the bulk film. It is important to note from Figure 46 and 47, that incidence angles of 0.5° and 1° revealed shifts in the position of the (112) diffraction line, which in turn imply variations in the lattice parameters, a and c , between the near-surface and bulk regions of the alloy.

In this regard, it is important to note that the position of the (112) diffraction line for surface sensitive scans at 0.5 ° and 1 ° is 26.94°. In the case of regular XRD analysis of the film, which represent information from the bulk material, the position of the (112) diffraction line decreased to approximately 26.8°. This confirms higher amount of sulfur at the CIGSeS absorber layer surface.

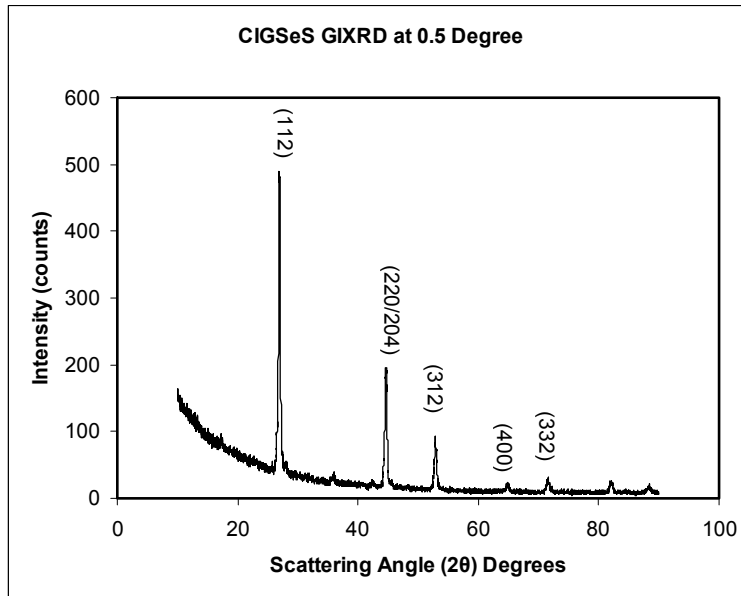


Figure 46: XRD pattern of CIGSeS showing (112) peak at 2θ angle 26.94 degrees

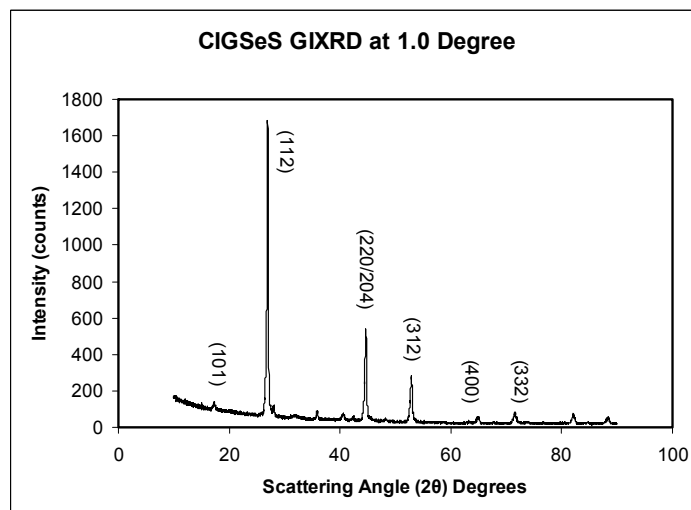


Figure 47: XRD pattern of CIGSeS showing (112) peak at 2θ angle 26.94 degrees

The current-voltage and quantum efficiency measurements are shown in Figures 48 and 49.

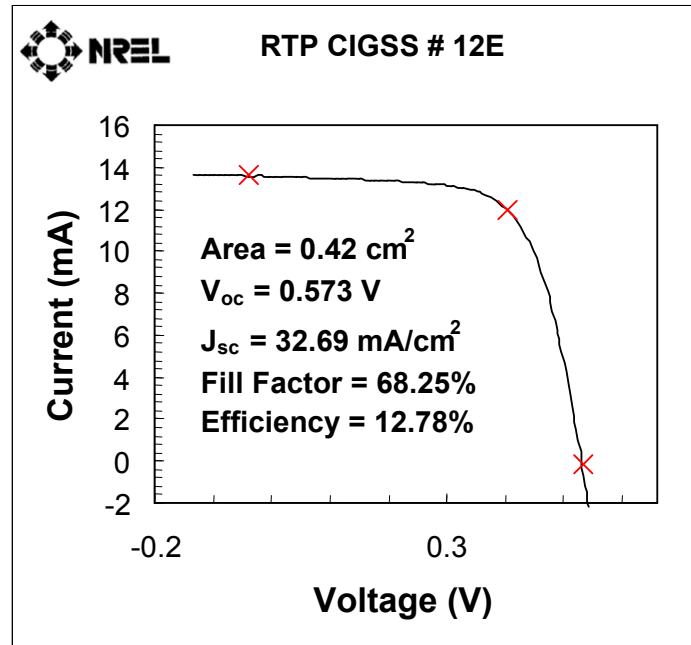


Figure 48: IV Characteristics of cell 12E

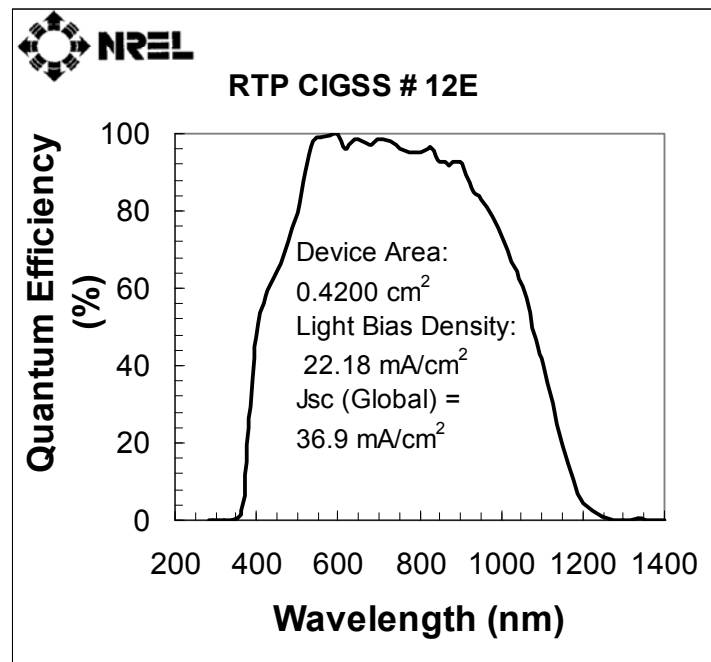


Figure 49: QE analysis of cell 12E

The detailed photovoltaic parameters were as follows, $V_{oc} = 573$ mV, $J_{sc} = 32.69$ mA/cm², FF = 68.25% and $\eta = 12.78\%$. The results showed that fine-tuning the sulfurization time has indeed improved the fill factor. Although the open circuit voltage (V_{oc}) values are lower from earlier experimental series of 613 mV to 573 mV. As the sulfurization time was reduced from 2 minutes at process temperature of 550°C to 1 minute and 30 seconds, the amount of sulfur diffused at the surface has also reduced along with the amount of sulfur near the molybdenum back contact. However, the trade-off is favorable in this case, due to fill factor improvements from 62.97% to 68.25% increasing the photovoltaic conversion efficiency from 12.75% to 12.78% even though the open circuit voltages have gone down from 613 mV to 573 mV, a difference of 40 mV. Although the improvement in the conversion efficiency is modest, 0.03% it demonstrates how the compositional gradients in the CIGSeS absorber layer affect the device parameters leading to changes in photovoltaic conversion efficiency.

This experimental series can now be used as a base for design of future experiments by optimizing the material properties by compositional gradients leading to even higher efficiencies. There are multiple approaches for obtaining this goal. One of them is changing the Cu/(In+Ga) ratio in the film, as sulfur diffuses faster in copper rich films than copper-poor ones [95], Cu/(In+Ga) ratio can be kept at the lowest possible value, e.g. 0.7 instead of in the present range of 0.82 to 0.85. It has been observed that efficiencies exceeding 19% have been obtained for devices having Cu/(In+Ga) of 0.69 [97]. This is one of the ways to reduce sulfur diffusion near the molybdenum back contact. Simultaneously increasing the amount of sulfur near the surface to increase the open circuit voltages can be achieved by increasing amount of time at the process

temperature. For example, if an open circuit voltage value of earlier experimental series can be obtained keeping the current density and fill factor the same as obtained during this experimental series, a photovoltaic conversion efficiency of 15.44 % and higher could be obtained.

Thus the hypothesis of optimizing sulfur near the back contact and its impact on reducing the fill factor values was correct as explained by these results.

Conclusion: Improvement in current-voltage characteristics for CIGSeS thin-film solar cells, is shown in Table 4.

Table 4: Improvement in current-voltage characteristics for CIGSeS thin-film solar cells

Cell #	V_{oc} (mV)	J_{sc}	% FF	% η
10E	545	30.41	65.97	10.93
14B	613	33.05	62.97	12.75
12E	573	32.69	68.25	12.78

Thus during the research carried out so far on rapid thermal processing for the formation of CIGSeS thin film solar cells, high efficiencies were obtained and it was demonstrated that good solar cell efficiencies (approaching 13%) can be achieved with relatively shorter cycle times, lower thermal budgets and without using toxic gases. The efficiency obtained here is the highest obtained by any University or National Lab for copper chalcopyrite solar cells by RTP.

The effect of material properties viz. composition, structure and morphology of CIGSeS absorber film on solar cell efficiency has been clearly demonstrated.

4.2 Electrical characterization of CIGSeS thin films.

External quantum efficiency (QE), Light Beam Induced Current (LBIC) and capacitance-voltage (C-V) analysis was carried out on the 12.78% efficient cell at the Colorado State University (CSU), and the results are provided in the following.

Results of external QE measurement are shown in the following Figure 50.

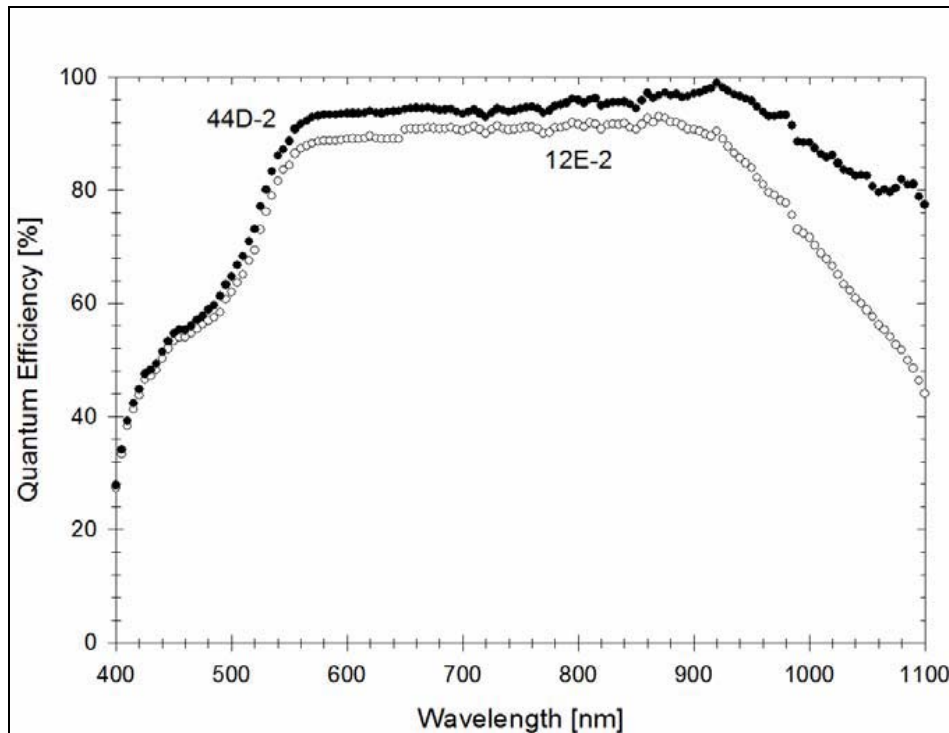


Figure 50: External QE analysis

External QE analysis of 12E RTP shows a band gap ~ 1.1 eV

Results of C-V analysis on the 12.78% efficient cell are provided in the following.

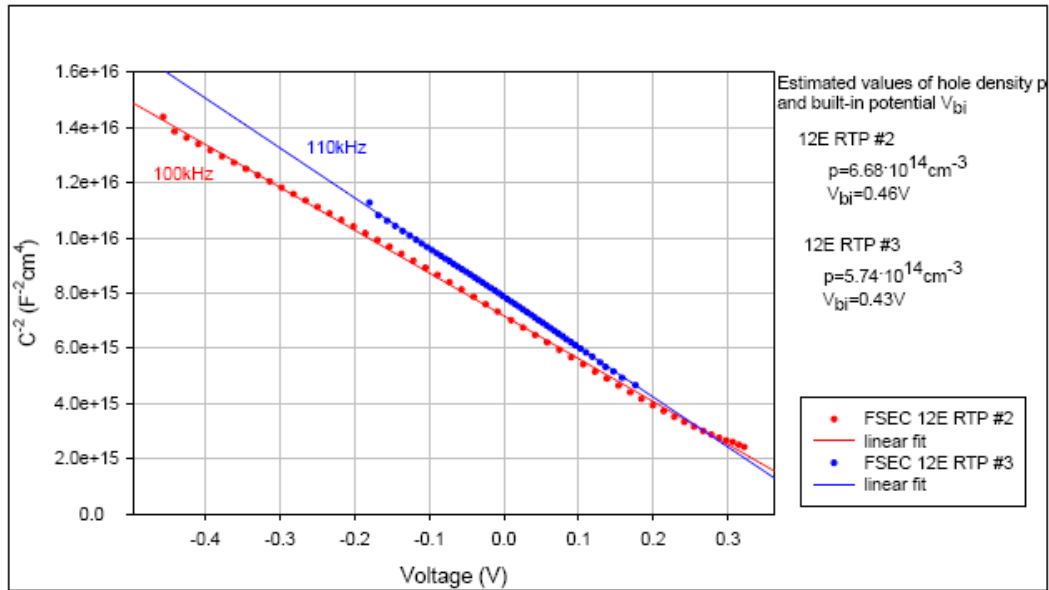


Figure 51: C-V Plot for RTP 12E

Figure 51 shows C-V measurements from substrate 12E RTP. The doping density in the n-type CdS heterojunction partner layer is much higher as compared to the p-type CIGSeS absorber layer. This enables the formation of n^+p diode; therefore most of the depletion layer is in the CIGSeS p-type layer. The data is fairly clean, and the C^{-2} vs. V plots are reasonably linear with plausible voltage intercepts. The inferred hole densities are all in the higher mid- 10^{14} range with modest variation between cells on the same substrate. The fairly linear curve suggests a uniform carrier density in the bulk of the material.

Light Beam Induced Current: Light Beam Induced Current (LBIC) is a reliable tool for investigating a variety of solar cell non-uniformities. Figure 52 shows the LBIC photoresponse (QE) maps for a non-shunted cell and Figure 53 shows the LBIC photoresponse (QE) maps for a shunted cell. Part of the dark area at the top is the probe shadow. The absolute QE is not calibrated, but it is clearly a factor of 10 to 20 less for the

shunted cells. The shunted pattern spreads gradually over the entire cell. The variation in the QE is in the range of 14-15% for the shunted cell and for the non-shunted it is in the range of 0-2%.

Three standard resolutions have been used for LBIC measurements (Figure 54). The lowest resolution has a 5 mm by 10 mm field with a 100 μm spot (A). This resolution covers the whole portion of the cell. The small square (A) in this view is magnified ten times for 500 by 500 μm field and a 10 μm spot. The area shown in a small square (1) of that map is multiplied 10 times more for the 50 by 50 μm field with a 1 μm spot for the high resolution map. The probe intensity is held near one sun for all of the LBIC measurements. This process makes it straightforward to zoom in on a small area of particular interest and to return to the same area even after the cell has been removed from the apparatus for other measurements. A quantum-efficiency change of $\pm 1\%$ (83-85%) is observed.

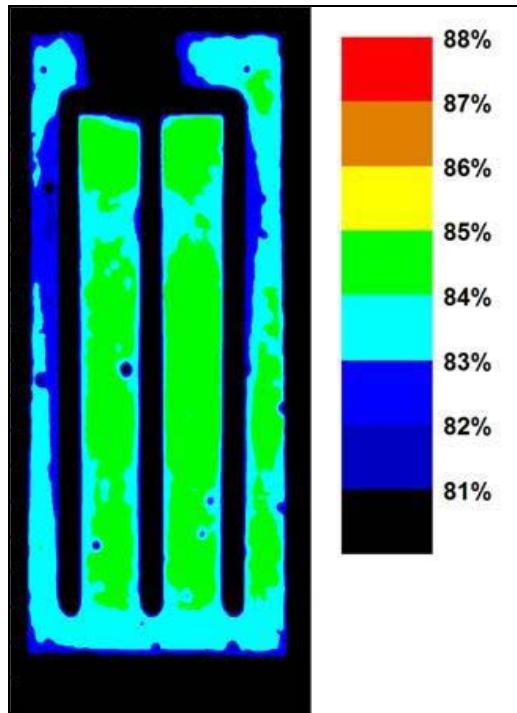


Figure 52: LBIC photoresponse map of non-shunted cell: RTP 12E-2

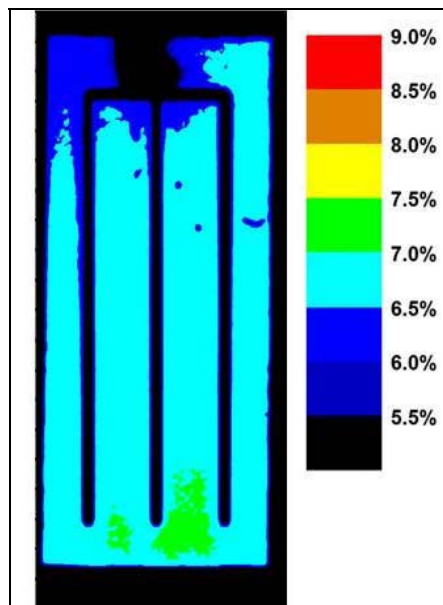


Figure 53: LBIC photoresponse map of shunted cell: RTP 12E-7

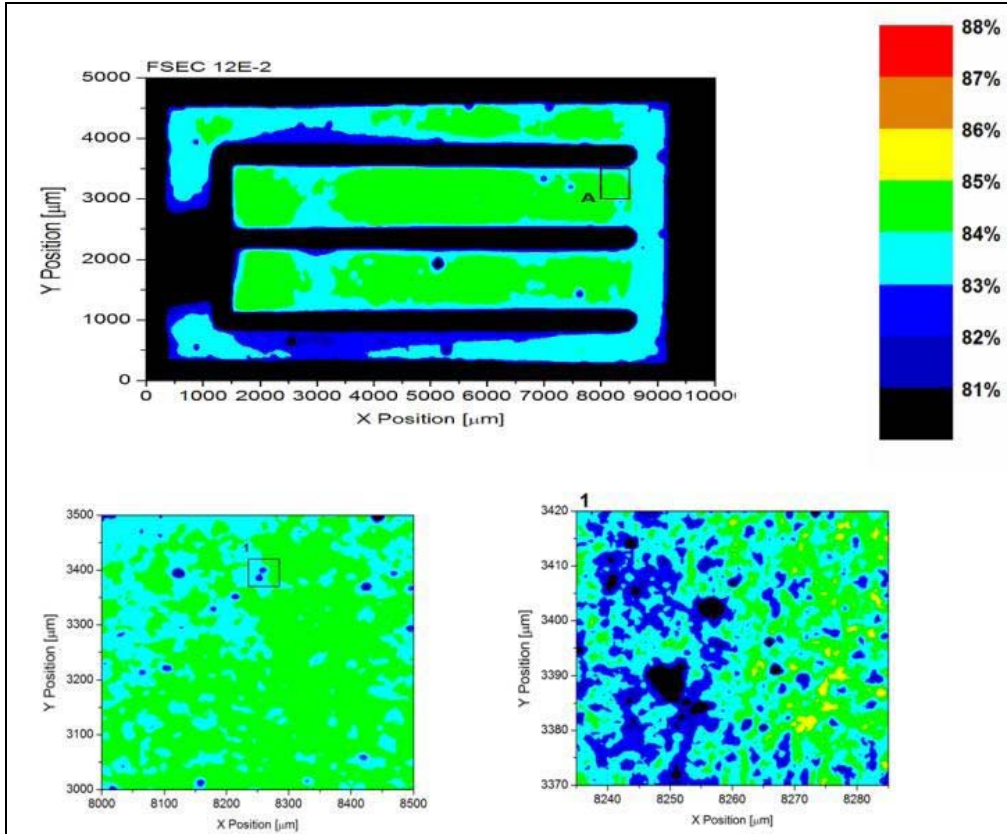


Figure 54: LBIC photoresponse map of non-shunted cell: RTP 12E-2

Figure 55 shows the general JV characteristics. The values obtained are as follows: efficiency 11%, fill factor 58%, $J_{sc} = 35.0 \text{ mA/cm}^2$, $V_{oc} = 540 \text{ mV}$. The efficiency is comparatively lower as the measured cell is not the same cell with 12.78% efficiency, but an adjoining cell. The cells were also handled considerably before measurements.

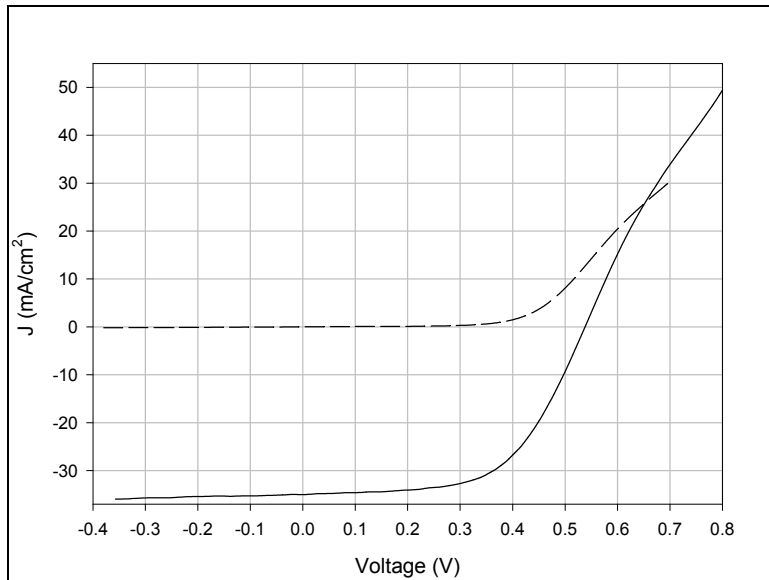


Figure 55: Dark and light JV characteristics

Figure 56 shows experimental JV curves at different temperatures from 238K to 303K with increments of 5K. From Figure 56, the effect of current limitation in forward bias also known as the rollover effect, can be clearly seen, which is presumed to be due to the presence of a back contact barrier. The rollover effect is very pronounced at low temperatures and disappears as temperature increases. The open circuit voltage increases as temperature is reduced and the short circuit current stays almost unchanged on average at 35.0 mA/cm².

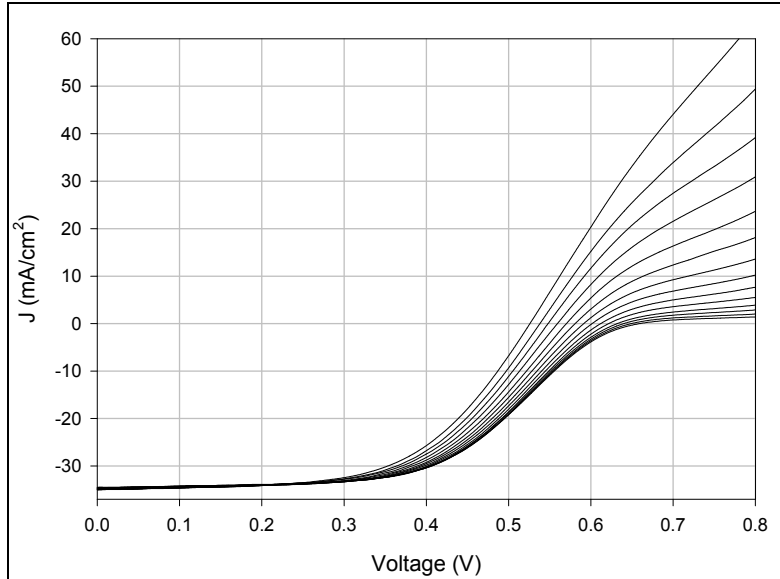


Figure 56: Temperature scan

Figure 57 shows dependence of the open circuit voltage on temperature. Intercept of the linear extrapolation with the $V_{oc}(T)$ axis gives the band-gap value of the absorber. It is in the 1.1-1.2 eV range, as expected for a CIGSeS device [96]. This result adds credibility to the obtained experimental data.

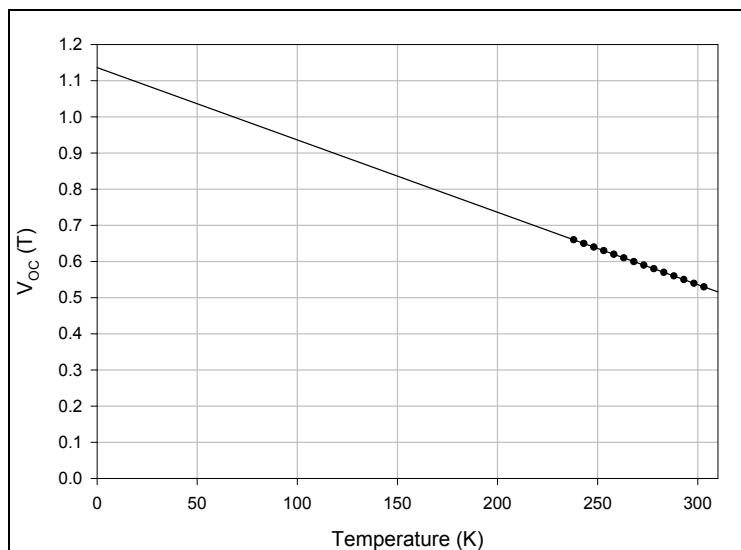


Figure 57: Dependence of the open circuit voltage on temperature

Figure 58 shows dependence of quantum efficiency and reflection on the wavelength. The quantum efficiency measurement was performed under approximately 30 mW/cm^2 white-light bias. Integrated product of quantum efficiency and solar spectrum results in short circuit current density (J_{sc}) of 35.0 mA/cm^2 and matches with the value obtained from J-V measurements, which supports the earlier findings based on the experimental data. From the part of the quantum efficiency curve between 450 and 550 nm, the thickness of the CdS layer can be estimated to be $\sim 50 \text{ nm}$.

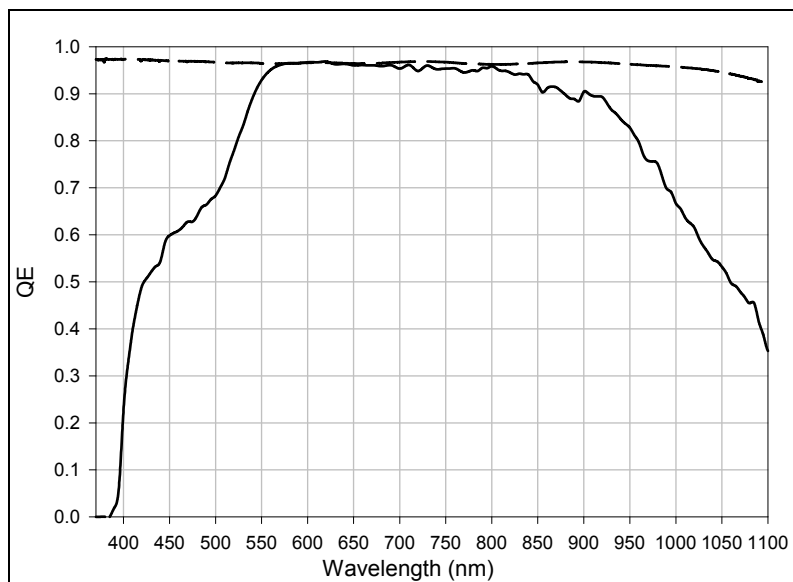


Figure 58: External Quantum efficiency –solid line, reflection – dashed line

Figure 59 shows dependence of the fill factor (FF) on temperature. The fill factor grows steadily from 53 to 58% as temperature increases from $\sim 240\text{K}$ to 280K and levels off at $\sim 280\text{K}$, where the rollover effect starts to disappear. Thus, the rollover effect does not affect fill factor for temperatures higher than 280K .

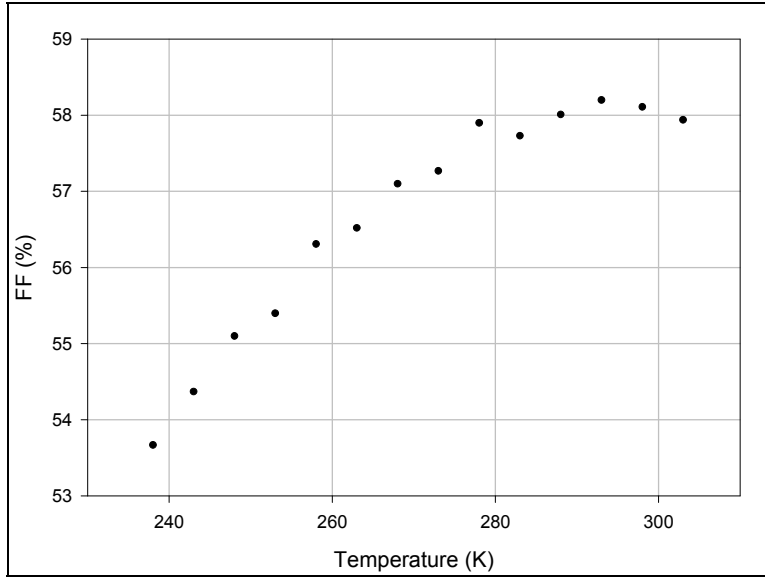


Figure 59: Dependence of the fill factor (FF) on temperature

The current at which the effect of rollover takes place, called a turning current, is given by the following expression:

$$J_t = A^* T^2 e^{-\frac{q\Phi_b}{kT}},$$

Where, A^* is the Richardson constant, Φ_b is the back contact barrier height, T is temperature, k is Boltzmann constant and q is elementary charge. The back contact barrier height is defined as the difference between the Fermi level in the bulk of the absorber and the valence band at the metal-semiconductor interface.

To find the turning current one has to take a J-V curve and make two linear fits to the data points just before the rollover and right after the rollover. The intersection of these two straight lines gives a turning point and the current at that point is the turning current. Solid lines in the Figure 60 represent calculated curves of the turning current at different values of the back contact barrier height ranging from 0.40 eV to 0.50 eV with increments of 0.02 eV, and dots are experimental data points found from J-V curves at

various temperatures. Figure 60 clearly illustrates that the back contact barrier height for the RTP device is approximately 0.44 eV. The reason for this can be higher sulfur near molybdenum back contact as discussed earlier in section 4.1.4. The last two points at two highest temperatures show slight deviation from the general trend, because as temperature increases, the rollover effect gets weaker and makes it more difficult to find the turning point.

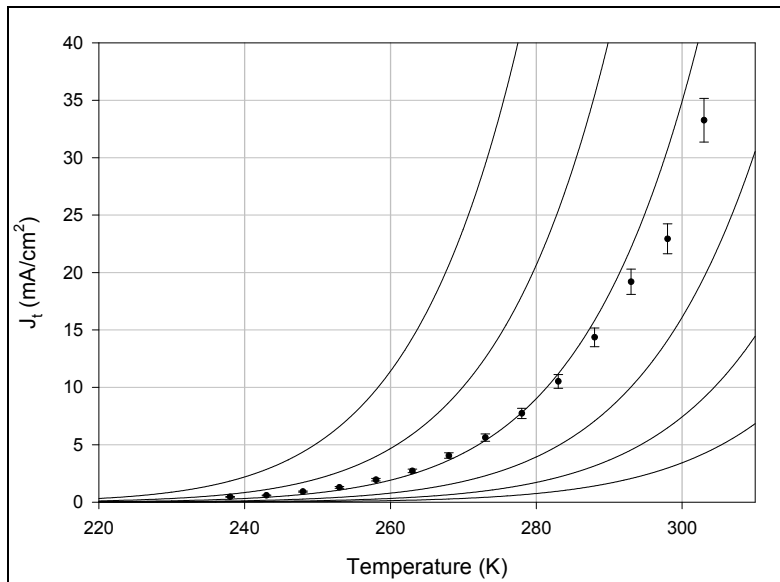


Figure 60: Back contact barrier height for cells prepared by RTP

Figure 61 is a semi-log version of Figure 60. From Figure 61, one can see that experimental data points deviate slightly from the 0.44 eV curve for lower temperatures, as well as for higher temperatures, and agree fairly closely for intermediate temperatures.

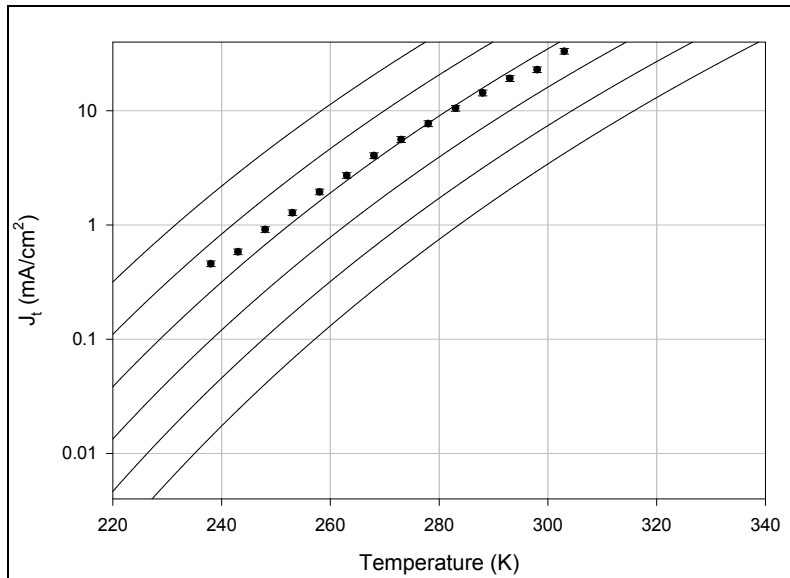


Figure 61: Semi log version of Back contact barrier height for cells prepared by RTP

Figure 62 shows C^{-2} dependence on voltage. The data is quite linear on this scale, and the slope gives a carrier density of $4.0 \times 10^{15} \text{ cm}^{-3}$. The capacitance-voltage analysis presented here is carried out for films prepared using 120 \AA NaF layer, this may be the reason for the enhanced carrier density observed in these films, compared to earlier films, where the carrier density was in the range of mid to higher 10^{14} cm^{-3} . Again it should be noted that due to asymmetric junction due to difference in doping densities, most of the depletion layer resides in CIGSeS p-type layer.

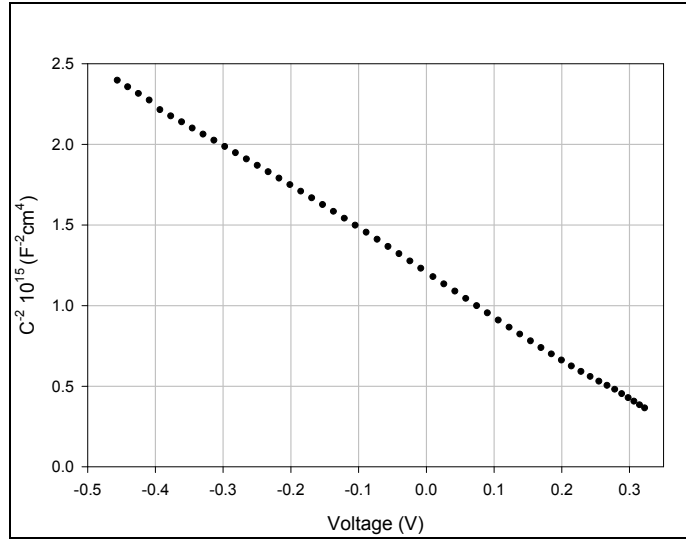


Figure 62: Capacitance voltage measurement and analysis

Figure 63 shows Fermi level relative to the valence band as a function of distance from the p-n junction obtained from capacitance-voltage measurements at room temperature. Figure 63 suggests that the Fermi level relative to the valence band in the bulk is approximately 0.21eV over a reasonable distance. The Fermi level moves to slightly lower values closer to the depletion layer.

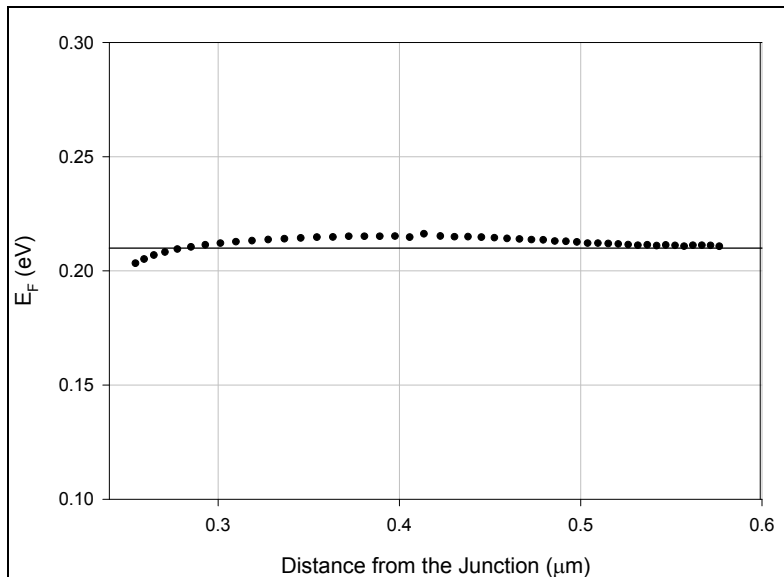


Figure 63: Fermi level relative to the valence band as function of distance from the p-n junction

Figure 64 is a schematic picture of the band diagram which summarizes all information obtained so far. A typical value of $2\ \mu\text{m}$ for the CIGS layer thickness is taken. The thickness of CdS layer is taken to be $50\ \text{nm}$ as it was estimated from the QE plot.

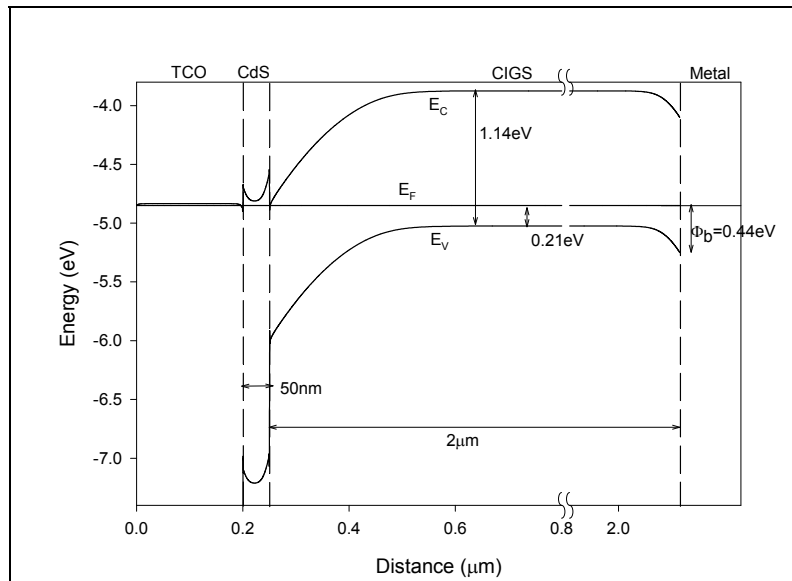


Figure 64: Schematic band diagram of CIGSeS thin-film solar cell

It can be seen in this model that the valence band is going down, near the molybdenum back contact, this can cause the fill factor reduction that was observed due higher amount of diffused sulfur content near the CIGSeS/Mo. This model does consider the Ga segregation to the back and thus does not consider the increase in the conduction band near the Mo interface due to higher gallium content. This analysis will be very useful in designing future experiments on CIGSeS thin film solar cells.

4.3 Performance analysis based on Semiconductor Properties:

CuIn_{1-x}Ga_xSe_{2-y}S_y (CIGSeS) thin films were fabricated by selenization/sulfurization of the sputtered Cu, In and Ga metallic precursors by rapid thermal processing. Solar cells were completed with the following process sequence, sodalime glass/Mo/CIGSeS/CdS/i-ZnO/ZnO:Al/Cr/Ag/MgF₂. A detailed analysis of a cell having an efficiency of 12.78% has been carried out. Device parameters such as series resistance R_s, shunt resistance R_p, diode quality factor A, and reverse saturation current density J₀ were estimated based on this analysis [98].

PV parameters measured under AM1.5 conditions at NREL were as follows: V_{oc} = 573 mV, J_{sc} = 32.69 mA/cm², FF = 68.25% and η = 12.78%. Detailed photovoltaic (PV) characterization of CIGSeS thin film solar cells is carried out. PV parameters of the best cells were measured under AM1.5 conditions at the National Renewable Energy Laboratory (NREL). Detailed analysis of PV characteristics was carried out at FSEC.

The current-voltage (I-V) and quantum efficiency (QE) characteristics of the CIGSeS cell is shown in Figure 48 and 49 respectively. The J-V characteristics in light and dark were compared as shown in Figure 65, to verify if the light characteristic was essentially a translated curve with light short circuit current density, J_{sc} or J_L.

Plot of dJ/dV versus V was plotted from the J-V characteristics are shown in Figure 66. The dJ/dV versus V curve measures the ac conductance around the short circuit current density (J_{sc}) point. The curve gives a shunt resistance R_p of ~510 Ω-cm² under illumination and ~1300 Ω-cm² in dark.

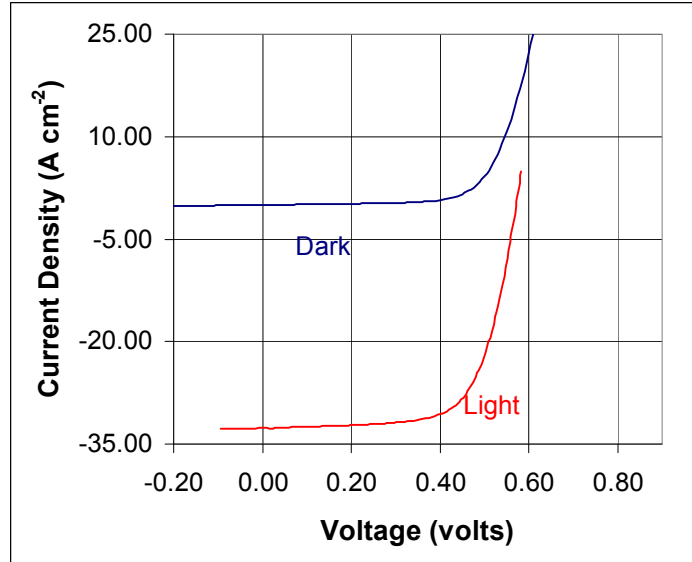


Figure 65: Variation of light and dark current densities with voltage

The dV/dJ versus $[J_0+J_{sc}]$ curve was plotted to estimate ac resistance in forward bias. A plot of dV/dJ versus $1/[J_0+J_{sc}]$ curve is provided in Figure 67. As can be seen from Figure 67, the curve is a linear. The series resistance R_s , can be obtained by extrapolating the curve to infinite current. Series resistance R_s of $\sim 0.8 \Omega\text{-cm}^2$ under illumination and $1.7 \Omega\text{-cm}^2$ in dark was obtained.

Values of the diode quality factor, A and reverse saturation current density, J_0 can be obtained from a plot of natural logarithm of $(J+J_{sc})$ versus corrected voltage V' i.e. $(V-R_s J)$. Figures 68 shows a plot of the diode quality factor, A and reverse saturation current density, J_0 versus $\ln [J \text{ (dark)}]$. The diode quality factor A is calculated to be ~ 1.87 and reverse saturation current density J_0 is $\sim 1.5 \times 10^{-7} \text{ A cm}^{-2}$.

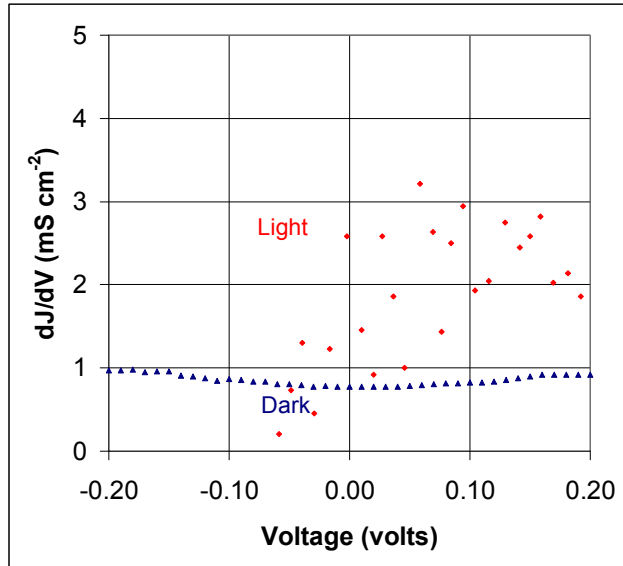


Figure 66: dJ/dV versus voltage characteristics

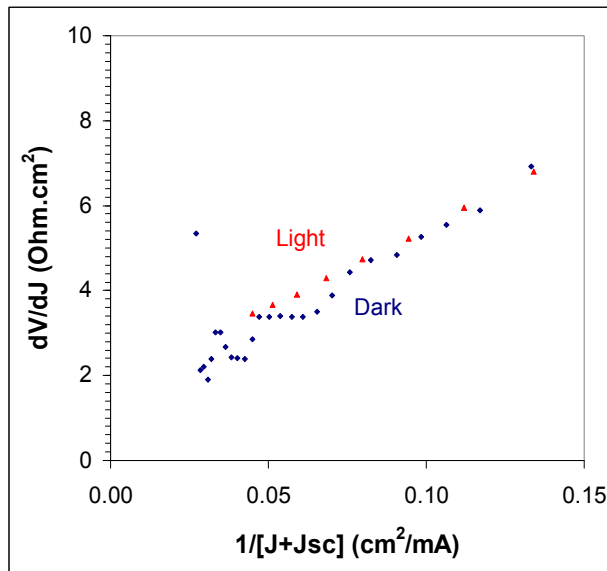


Figure 67: Variation of dV/dJ with $1/[J+J_{sc}]$

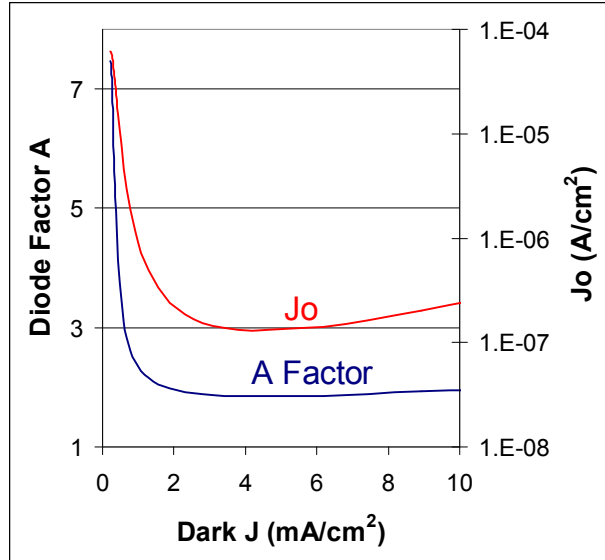


Figure 68: Variation of diode quality factor, A and reverse saturation current density, J_0 with the dark current density, J.

From the above analysis the values of shunt resistance (R_p) of $\sim 510 \Omega\text{-cm}^2$ under illumination and $\sim 1300 \Omega\text{-cm}^2$ in dark, series resistance (R_s) of $\sim 0.8 \Omega\text{-cm}^2$ under illumination and $\sim 1.7 \Omega\text{-cm}^2$ in dark, diode quality factor (A) of 1.87, and reverse saturation current density (J_0) of $1.5 \times 10^{-7} \text{A cm}^{-2}$ were obtained.

This type of analysis is very helpful for obtaining device parameters, their relationship with cell processing parameters and thus to optimize the processing technique for improving the cell performance.

4.4 CIGS2 solar cells band-offset measurements

In order to achieve an optimal overlap with the solar spectrum, Cu(In,Ga)S_2 (CIGS2) would be more favorable as compared to CIGS cells due to band gap of CIGS2 which is 1.5 eV or higher depending upon gallium content. Efficiencies of cells based on CIGS2 are presently limited to below 13% [99]. The main reason is that the expected linear gain

in the open circuit voltage (V_{oc}) compared to that of CIGS could not be achieved so far. The origin of this behavior is not understood. Several models suggest that this is caused by a non-ideal conduction band offset (CBO) at the interface between the CIGS absorber and the commonly used CdS heterojunction partner layer. Therefore, experiments were carried out to obtain band-offset values at the CIGS2/CdS interface as explained in the following.

Molybdenum back contact and the metallic precursors, indium and copper–gallium (CuGa) were sputter deposited by DC magnetron sputtering. The metallic precursors were sulfurized at 475°C in 4% H₂S/Nitrogen gas mixture to obtain copper-indium-gallium disulfide (CIGS2) thin films with Cu-excess. For the purpose of analysis samples were categorized according to the treatment. Samples after sulfurization treatment were categorized as unetched (SSUn). Samples that were etched in 10% KCN solution for 3 min were labeled etched (SSE). Samples that were etched and oxidized in 50/50 solution of 5% H₂SO₄ and H₂O₂ [99] were labeled treated (SSEO). CdS layer was deposited over the unetched, etched and treated samples to create an interface. Ultra thin, approximately 5 nm layer of discontinuous CdS layer was deposited using chemical bath deposition (CBD). For the band offset measurements, three samples with varying CdS thickness were prepared, ranging from approximately 5 nm to a film thickness as used in real devices (~50 nm). All samples were investigated by Auger electron spectroscopy, ultraviolet photoelectron spectroscopy (UPS) with He I and He II excitation, by X-ray Photoelectron Spectroscopy (XPS) with a Mg K α X-ray source, and by Inverse Photoemission Spectroscopy (IPES). CdS layers of various thicknesses were deposited. The AES data presented here is for a sample on which ~5 nm CdS was deposited.

Thickness of CdS films was measured by Auger electron spectroscopy at the University of Florida, Gainesville while the photoelectron spectroscopies were carried out at the Universität Würzburg, Germany.

4.4.1 AES Analysis

The AES surface survey of SS/Cr/Mo/CIGS2 samples provided in Figure 69, showing the presence of Cd, S, Cu, O and C on the surface. Proportions of elements at the surface was as follows, Cu:S:Cd:C:O of, 5.6:41.9:32.7:16.1:3.8.

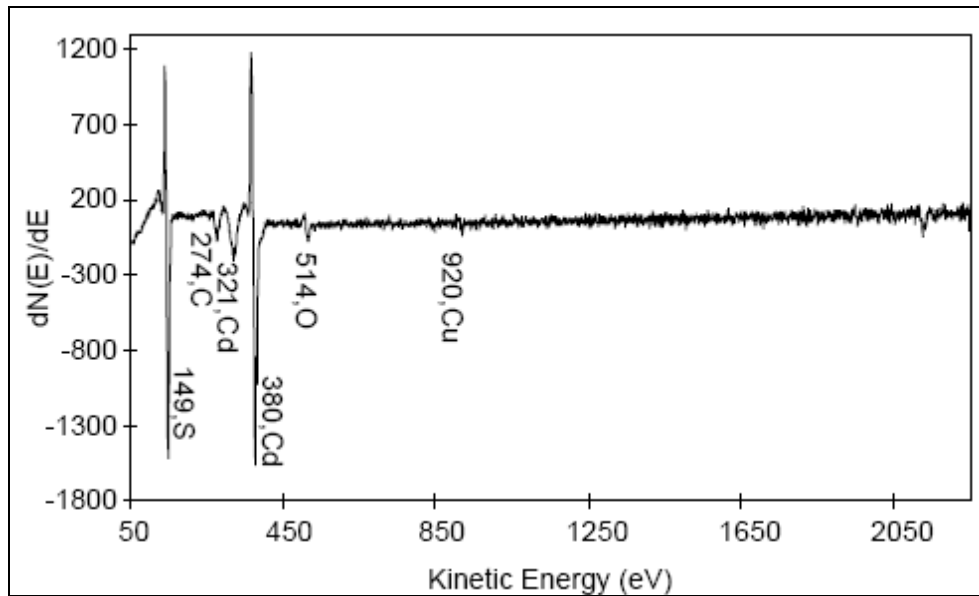


Figure 69: Surface survey showing presence of Cd, S, Mo, C and O.

The CdS layer is known to grow conformally on CIGS and CIGS2 thin films. The exact thickness at each location may be varying. Analysis parameters for AES measurements were 0.1 min etching per cycle at 5 KV. Cadmium was high at the surface and decreased towards the back contact, as shown in Figure 70. The depth profile presented in Figure 71 is from the surface to molybdenum back-contact. As observed, Cu signal remains fairly uniform along the depth of CIGS2. Sulfur was uniformly distributed all along the depth

of CIGS2. From the CIGS2/CdS interface towards the bulk the indium amount was more than the gallium and towards the CIGS2/Mo interface the gallium content increased while that of indium decreased as shown in Figure 71.

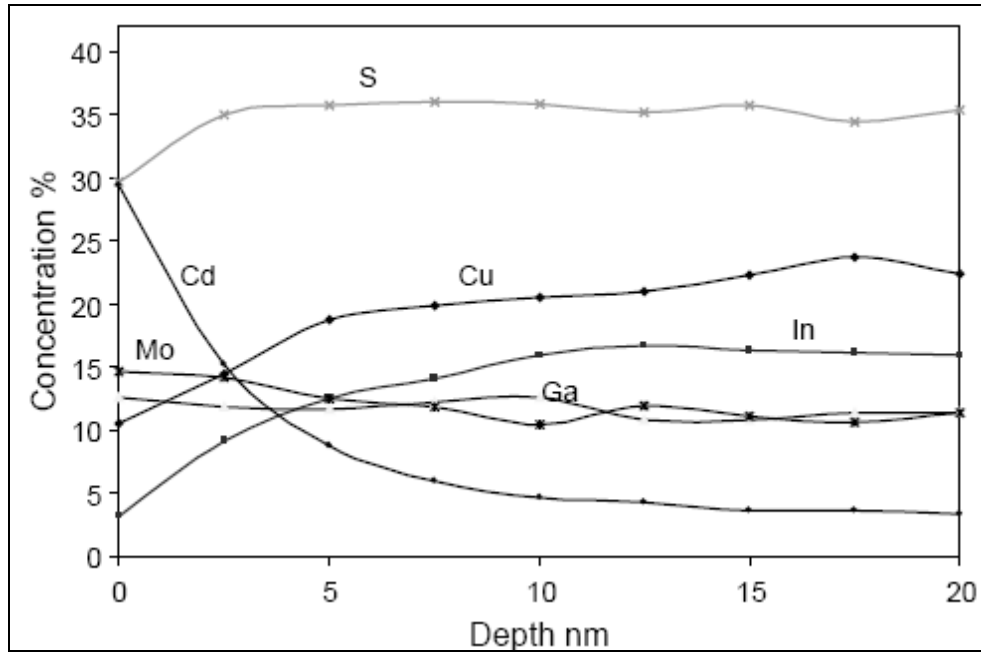


Figure 70: Cadmium depth profile by AES.

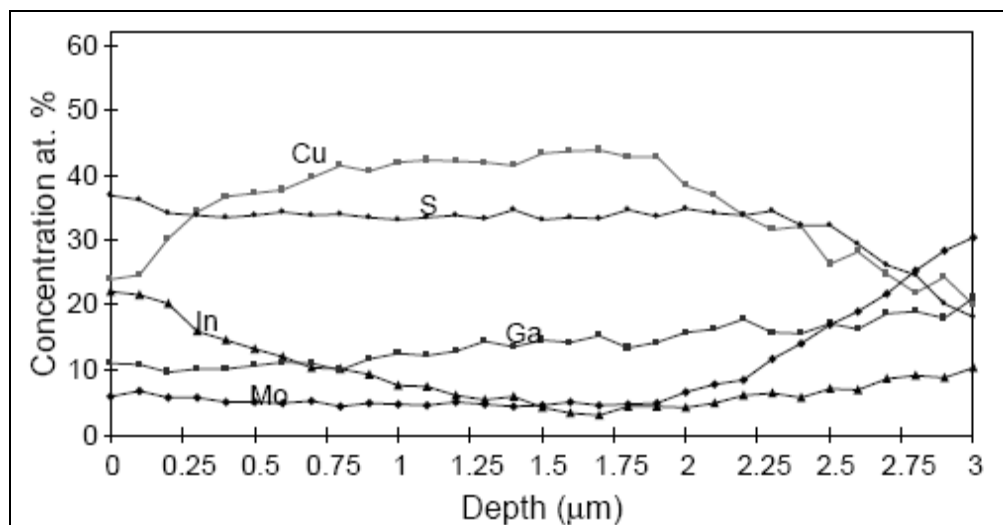


Figure 71: Variation of indium and gallium along the depth

This trend was observed because gallium has a tendency to diffuse towards back contact and since gallium and indium are from group III, they tend to substitute each other. It was observed that the amount of molybdenum appears significant at the surface and throughout the bulk of the absorber layer; also the trend and amount of gallium and indium in the CdS layer are not conclusive. It was noted from the surface survey of the same sample taken at the location where depth profiling was carried out that no traces of Mo, Ga and In exist (Figure 69). The profiles for Ga/In in CdS layer and Mo are believed to be artifact arising from the background noise.

4.4.2 X-ray Photoelectron Spectroscopy (XPS) analysis using Mg K α radiation

4.4.2.1 Unetched absorber (SSUn)

Sulfurization of metallic precursors in H₂S atmosphere creates a copper rich layer of CuS on chalcopyrite CIGS2 film. The film appeared highly oxidized due to atmospheric oxygen during handling. From the In 3d line, thickness of CuS film was approximated (assuming a homogeneous layer) to be roughly around 2–3 nm [99].

4.4.2.2 KCN etched absorber (SSE)

The oxidized CuS layer was removed by the KCN treatment. In addition to Cu and sulfur peaks, indium and gallium elements associated with the absorber layer also appeared.

Furthermore the KCN treatment caused the deposition of K on the surface as shown in Figure 72.

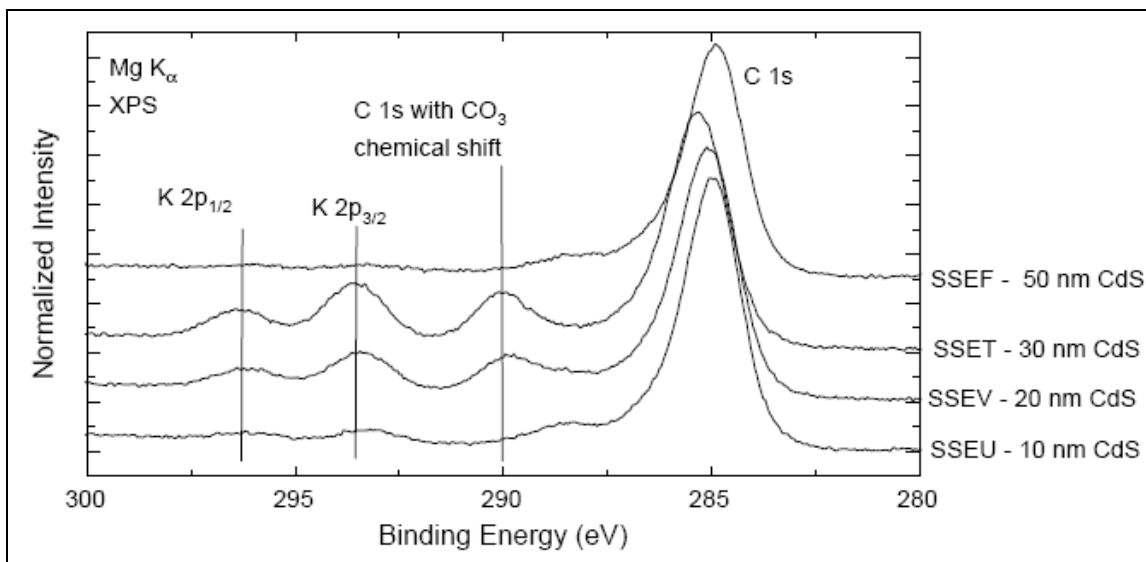


Figure 72: C and K peaks for varied thickness of CdS.

4.4.2.3 Oxidation treatment in H $_2$ O $_2$ /H $_2$ SO $_4$ (SSEO)

Oxidation treatment was carried out for the passivation of the etched surface. Potassium deposited during the KCN etch was removed by this treatment. Furthermore, there was an increase in the Cu amount on the surface whereas the indium and S intensities decrease slightly.

4.4.2.4 Samples with thick CdS layer on top

The survey scans (Figure 72) show a thick (i.e. no residual absorber lines visible, SSEF) CdS layer. Potassium was observed on the surface of thinner CdS layer deposited on

KCN etched absorbers due to diffusion through the CdS layer. The thick CdS layer on etched and oxidized absorbers showed no potassium. On all CdS films that showed potassium on their surface also showed the presence of C species Figure 72, that was identified (by its chemical shift) originating from CO_3 in accordance with strongly increased O1s line for these samples. These observations indicated that the potassium compound on the surface is KCO_3 . It also indicates that CdS thickness of ~ 50 nm is essential to completely eliminate potassium.

4.4.3 Band offset measurements

Accurate measurement of band offset requires a clean surface, which was achieved by removing the adsorbates with mild Ar^+ sputtering. To minimize sputter-induced damage, a very low ion energies (50 eV) and low currents (~ 50 nA/cm²) were used. Furthermore, the surface was closely monitored to observe any changes taking place after each sputter step. While it is well known that prolonged sputtering of CuInSe_2 with 500 eV Ar ions leads to the formation of metallic phases at the surface [100], no such phases were found when sputtering with 50 eV ions.

Bandgaps were determined from UPS spectra of the valence band and the IPES spectra of the conduction band for both, the CIGS2 absorber and the CdS heterojunction partner layer. Bandgap value of $1.76 (\pm 0.15)$ eV was obtained for clean CIGS2 surface. This value is reasonable, taking into account that the bulk band gap value of CuInS_2 of 1.5 eV should be increased due to additional amount of Ga that results in higher bandgap as mentioned above as well as by a copper depletion at the absorber surface. For CdS band gap of $2.47 (\pm 0.15)$ eV, close to the bulk band gap of CdS (2.42 eV [100]) was observed. It is believed that other heterojunction partner such as mixed ZnS/ZnO or InS/InO may be

more appropriate for better match with CIGS2 and thus would result in higher efficiency [99]. The determination of the band alignment was carried out in a two step process. In the first step the CBM (VBM) values of the CIGS2 surface were compared with those of the CdS surface. Second step considered changes in the band bending of CIGS2 due to the interface formation process as well as band bending towards the CdS surface (together henceforth called ‘interface-induced band bending’). Comparing the core level line positions of the clean CIGS2 surface, the CIGS2 interface and the thin CdS layer, and the thick CdS film surface, corrections for the interface-induced band bending was computed.

In the first step the CBM of CIGS2 and that of CdS were compared, which were 0.86 (± 0.10) and 0.46 (± 0.10) eV, respectively, indicating a cliff of ~ 0.4 eV in the conduction band. In the valence band a VBM of -0.90 (± 0.10) eV for CIGS2 and -2.01 (± 0.10) eV for CdS were obtained. These approximate results were corrected for the interface-induced band bending in the second step. For that purpose different combinations of core level lines of the CIGS2 absorber (Ga 2p, Cu 2p, In 3d) and the CdS heterojunction partner (Cd 3d, S 2p) were used. In total 12 different values of band bending were obtained. The mean value of these combinations was -0.05 (± 0.10) eV, indicating that the interface-induced band bending correction, to be very small. Including the correction, the band offset values obtained were -0.45 (± 0.15) eV for the CBO and -1.06 (± 0.15) eV for the VBO [100]. The resulting band alignment at the CdS/CIGS2 interface is shown in Figure 73.

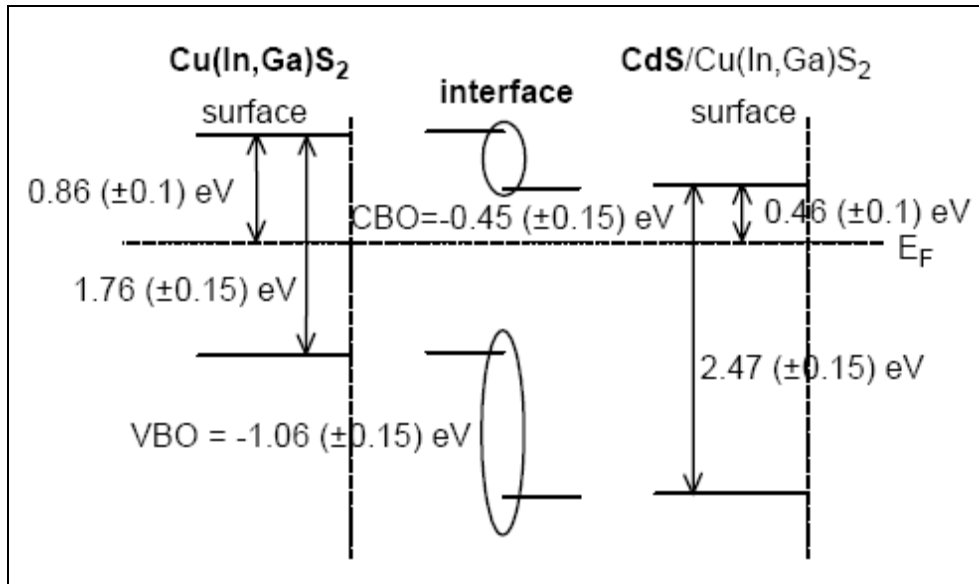


Figure 73: Schematic diagram of the band alignment at the CdS/CIGS2 interface.

CHAPTER 5

SUMMARY AND CONCLUSIONS

A rapid thermal processing (RTP) reactor for the preparation of graded $\text{CuIn}_{1-x}\text{Ga}_x\text{Se}_{2-y}\text{S}_y$ (CIGSeS) thin-film solar cells has been designed, assembled and is being used at the Photovoltaic Materials Laboratory of the Florida Solar Energy Center. This was the first time that the RTP process has been utilized for the preparation of CIGSeS thin-film solar cells by any University or National Laboratory. CIGSeS films having optimum composition, morphology, and semiconducting properties were prepared using RTP. Initially films having various Cu/(In+Ga) ratios were prepared. In the next step selenium incorporation in these films was optimized so as to obtain desired semiconducting properties. Selenium incorporation was increased from ~40 atomic % successively to ~42, 46 and 50 atomic %. This was followed by sulfur incorporation in the surface to increase the bandgap at the surface. The process parameters for the substitution of selenium by sulfur were optimized. Initially the sulfur content was ~20 atomic %. It was reduced systematically the optimum level of ~5 atomic %. In the process, the compositional gradient of sulfur was fine-tuned by decreasing the sulfurization time from 2 minutes to 1 minute 30 seconds. Materials properties of these films were characterized by optical microscopy, SEM, AFM, EDS, XRD, GIXRD, AES, and EPMA. The depth profile by AES confirmed the incorporation of sulfur near the CIGSeS surface and at the CIGSeS/Mo interface. This fact has been verified by GIXRD results. It was found that CIGSeS film composition can be fine tuned by decreasing the quantity of sulfur near the molybdenum back contact. This resulted in a double bandgap graded absorber with photovoltaic conversion efficiency of 12.78%. The grain size of polycrystalline CIGSeS

films is $\sim 1 \mu\text{m}$. The completed cells were extensively studied by electrical characterization. Current-voltage (I-V), external and internal quantum efficiency (EQE and IQE), capacitance-voltage (C-V), and light beam induced current (LBIC) analysis was carried out. The quantum efficiency curve shows the improvement in collection of lower energy photons when sulfur incorporation mainly occurs at the surface and comparatively less near the molybdenum back contact region. Capacitance-voltage analysis gave a carrier density of $4.0 \times 10^{15} \text{ cm}^{-3}$. LBIC analysis shows uniform quantum efficiency of 83-85% over the analyzed area with variation of $\pm 1\%$. J-V curves were obtained at different temperatures. Dependence of the open circuit voltage and fill factor on temperature has been estimated. Bandgap value calculated from the intercept of the linear extrapolation was $\sim 1.1-1.2 \text{ eV}$.

Semiconductor properties analysis of $\text{CuIn}_{1-x}\text{Ga}_x\text{Se}_{2-y}\text{S}_y$ (CIGSeS) thin-film solar cells with an efficiency of 12.78% has been carried out. The values of various PV parameters determined using this analysis were as follows: shunt resistance (R_p) of $\sim 510 \Omega\text{-cm}^2$ under illumination and $\sim 1300 \Omega\text{-cm}^2$ in dark, series resistance (R_s) of $\sim 0.8 \Omega\text{-cm}^2$ under illumination and $\sim 1.7 \Omega\text{-cm}^2$ in dark, diode quality factor (A) of 1.87, and reverse saturation current density (J_0) of $1.5 \times 10^{-7} \text{ A cm}^{-2}$. This type of analysis is very helpful for obtaining device parameters, their relationship with cell processing parameters and thus to optimize the processing technique for improving the cell performance.

CIGS2 cells have a better match to the solar spectrum due to their comparatively higher band-gap as compared to CIGS cells. However, they are presently limited to efficiencies $< 13\%$ which is considerably lower than that of CIGS cells of 19.9%. One of the reasons for this lower efficiency is the conduction band offset between the CIGS2 absorber layer

and the CdS heterojunction partner layer. The value of band offset between the CIGS2 and the CdS measured by a combination of Ultraviolet Photoelectron Spectroscopy (UPS) and Inverse Photoemission Spectroscopy (IPES) was -0.45 eV, i.e. a cliff is present between these two layers. It enhances the recombination at junction; this limits the efficiency of CIGS2 wide-gap chalcopyrite solar cells.

The knowledge gained from this research work can be used to design future experiments by optimizing the material properties by compositional gradients leading to even higher efficiencies. There are multiple approaches for obtaining this goal. One of them is changing the Cu/(In+Ga) ratio in the film, as sulfur diffuses faster in copper rich films than copper-poor ones [95], Cu/(In+Ga) ratio can be kept at the lowest possible value, e.g. 0.7 instead of in the present range of 0.82 to 0.85. It has been observed that efficiencies exceeding 19% have been obtained for devices having Cu/(In+Ga) ratio of 0.69 [97]. This is one of the ways to reduce sulfur diffusion near the molybdenum back contact. Simultaneously, the amount of sulfur incorporation in the CIGSeS surface can be increased to obtain higher open circuit voltages. By applying this technique, present thin-film solar cell open circuit voltage can be increased to already obtained value of 613 mV, assuming other device parameters remaining same as of 12.78% efficient cell, present photovoltaic conversion efficiency can be enhanced to ~15.44% and higher. The rapid thermal processing does have unique advantages related to thin-film solar cell manufacturing; the knowledge acquired through this research work will be useful to thin-film solar cell manufacturing start-ups as well as to the firms already in production using rapid thermal processing.

REFERENCES

- [1] K. Zweibel, "Harnessing Solar Power: The Photovoltaic challenge", Plenum publishing corporation, New York.
- [2] U. Rau and W. Shock, chapter 7 'Clean Electricity From Photovoltaics' edited by Mary Archer and Robert Hill, Imperial college press, vol. 1, ISBN 1-86094-161-3, 2001.
- [3] X. Wu, J. C. Keane, R.G. Dhere, C. DeHart, A. Duda, T.A. Gessert, S. Asher, D.H. Levi, P. Sheldon, "16.5% Efficient CdS/CdTe Polycrystalline Thin-Film Solar Cells", Proceedings of the 17th European Photovoltaic Solar Energy Conference, 995, 2001.
- [4] K. L. Chopra, P. D. Paulson and V. Dutta, "Thin-Film Solar Cells: An Overview", Progress in Photovoltaics: Research and Application; vol. 12, 69, 2004.
- [5] Ingrid Repins, Miguel A. Contreras, Brian Egaas, Clay DeHart, John Scharf, Craig L. Perkins, Bobby To and Rommel Noufi "19.9%-efficient ZnO/CdS/CuInGaSe₂ Solar Cell with 81.2% Fill Factor", Progress in Photovoltaic: Research and Application, vol. 16, 235, 2008.
- [6] M. Archer and R. Hill, "Clean Electricity from Photovoltaic", Series on photo-conversion of solar energy, vol. 1, ISBN 1-86094-161-3, Imperial College Press, 2001.
- [7] R. S. Muller, T. I. Kamins and M. Chan, "Device Electronics for Integrated Circuits", ISBN 0471593982, John Wiley & Sons; 3rd edition, 2002
- [8] S.M. Sze," Physics of Semiconductor Devices," Wiley, New York, 1981.
- [9] A. Luque and S. Hegedus, "Handbook of Photovoltaic Science and Engineering", John Wiley and Sons, ISBN 0-471-49196-9, England, 2003.

- [10] Lindmayer and Wrigley, "Fundamental of Semiconductor Devices", D. Van Nostrand Company, Inc., Princeton, NJ, 1965.
- [11] K. Zweibel, "Harnessing Solar Power: The Photovoltaic challenge", ISBN 0-306-43564-0, Plenum publishing corporation, New York, 1990.
- [12] C. Rinçon and J Gonzalez, "Temperature Dependence of the Bandgap in CuInSe_2 ", Solar Cells, vol.16, 357, 1986.
- [13] L.L. Kazmerski, M. Hallerdt, P.J. Ireland, R.A. Mickelsen and W.S. Chen, "Optical Properties and Grain Boundary Effects in CuInSe_2 ", Journal of Vacuum Science and Technology A, vol. 1, 395, 1983.
- [14] B. Dimmler, H. Dittrich, R. Menner, and H.W. Schock, "Performance and Optimization of Heterojunctions Based on $\text{Cu}(\text{Ga},\text{In})\text{Se}_2$ ", Proceedings of 19th IEEE Photovoltaic Specialist Conference, New York, 1454, 1987.
- [15] A. Jasenek, U. Rau, K. Weinert, I. M. Kötschau, G. Hanna, G. Voorwinden, M. Powalla, H. W. Schock and J. H. Werner, "Radiation Resistance of $\text{Cu}(\text{In},\text{Ga})\text{Se}_2$ Solar Cells Under 1-MeV Electron Irradiation", Thin Solid Films, vol. 387, 228, 2001.
- [16] J.F. Guillemoles, "Stability of $\text{Cu}(\text{In},\text{Ga})\text{Se}_2$ Solar Cells: a Thermodynamic Approach", Thin Solid Films vol. 361-362, 338, 2000.
- [17] W. E. Devaney and R. A. Mickelsen, "Vacuum Deposition Processes for CuInSe_2 and CuInGaSe_2 Based Solar Cells", Solar Cells, vol. 24, 19, 1988.
- [18] R. W. Birkmire, L. C. DiNetta, P. G. Lasswell, J. D. Meakin, and J. E. Phillips, "High Efficiency CuInSe_2 Based Heterojunction Solar Cells: Fabrication and Results", Solar Cells, vol. 16, 419, 1986.

- [19] L. D. Laude, M. C. Joliet, and C. Antoniadis, "Laser-induced Synthesis of Thin CuInSe₂ Films", *Solar Cells*, vol. 16, 199, 1986.
- [20] M. C. Joliet, C. Antoniadis, R. Andrew and L. D. Laude, "Laser-induced synthesis of thin CuInSe₂ films", *Applied Physics Letter*, vol. 46, 266 1985.
- [21] R. D. L. Kristensen, S. N. Sahu, and D. Haneman, "Flash Evaporation of CuInSe₂ Films", *Solar Energy Material*, vol. 17, 329, 1988.
- [22] N. Romeo, V. Canevari, G. Sberveglieri, and A. Bosio, "Growth of Large-grain CuInSe₂ Thin-Films by Flash-Evaporation and Sputtering", *Solar Cells*, vol. 16, 155, 1986.
- [23] T. F. Ciszek, "Growth and Properties of CuInSe₂ Crystals Produced by Chemical Vapor Transport with Iodine", *Journal of Crystal Growth*, vol. 70, 405, 1984.
- [24] C. W. Bates. Jr. K. F. Nelson. S. A. Raza. J. B. Mooney. J. M. Recktenwald, L. Macintosh, and R. Lamorcaux, "Spray Pyrolysis and Heat Treatment of CuInSe₂ for Photovoltaic Applications", *Thin Solid Films*, vol. 88, 279, 1982.
- [25] J. Bougnot, S. Duchemin, and M. Savelli, "Chemical Spray Pyrolysis of CuInSe₂ Thin Films", *Solar Cells*, vol. 16, 221, 1986.
- [26] J. Piekoszewski, J. J. Loferski, R. Beualieu, J. Beall, B. Roessler, and J. Shewchun, "RF-Sputtered CuInSe₂ Thin Films", *Solar Energy Material*, vol. 2, 363, 1980.
- [27] B. Schumann, A. Tempel, and G. Kuhn, "Epitaxial Layers of CuInSe₂", *Solar Cells*, vol. 16, 43, 1986.
- [28] N. Takenoshita, "Liquid Phase Epitaxial Growth and Electrical Characterization of CuInSe₂", *Solar Cells*, vol. 16, 65, 1986.

- [29] Y. Ueno, H. Kawai, T. Sugiura, and H. Minoura, "Electrodeposition of CuInSe₂ Films from a Sulphate Bath", *Thin Solid Films*, vol. 157, 159, 1988.
- [30] V. K. Kapur, B. M. Basol, and E.-S. Tseng, "Low Cost Methods for the Production of Semiconductor Films for CuInSe₂/CdS Solar cells", *Solar Cells*, vol. 21, 65, 1987.
- [31] V. K. Kapur, A. Bansal, P. Le and O. I. Asensio, "Non-vacuum Processing of CuIn_{1-x}Ga_xSe₂ Solar Cells on Rigid and Flexible Substrates using Nano-particle Precursor Inks", *Thin Solid Films*, vol. 431-432, 53, 2003.
- [32] N. G. Dhere, S. R. Ghongadi, M. B. Pandit, A. H. Jahagirdar and D. Scheiman, "CIGS₂ Thin-Film Solar Cells on Flexible Foils for Space Power", *Progress in Photovoltaics: Research and Application*, vol. 10, 407, 2002.
- [33] G.Hades, T. Engelhard, D. Cahen, L. L. Kazmerski, and C. R. Herrington, "Electroplated CuInS₂ and CuInSe₂ Layers: Preparation and Physical and Photovoltaic Characterization", *Thin Solid Films*, vol. 128, 93, 1985.
- [34] B. M. Basol, V. K. Kapur, A. Halani, C. R. Leidholm, J. Sharp, J. R. Sites, A. Swartzlander, R. Matson, and H. Ullal, "Cu(In,Ga)Se₂ Thin Films and Solar Cells Prepared by Selenization of Metallic Precursors", *Journal of Vacuum Science and Technology, A* vol. 14(4), 2251, 1996.
- [35] N. G. Dhere, S. Kuttath and H. R. Moutinho, "Morphology of Precursors and CuInGaSe₂ Thin Films Prepared by a Two-stage Selenization Process", *Journal of Vacuum Science and Technology, A*, vol. 13(3), 1078, 1995.

- [36] N. G. Dhere and K. W. Lynn, "Gallium Content Enhancement In CIGS Thin Films Prepared By Two-Selenization Process Using Se Vapor", 25th Photovoltaic Specialists Conference, 897, 1996.
- [37] T. Yamamoto, M. Nakamura, J. Ishizuki, T. Deguchi, S. Ando, H. Nakanishi and S.F. Chichibu, "Use of Diethylselenide as a Less-hazardous Source for Preparation of CuInSe₂ Thin Films by Selenization of Metal Precursors", Journal of Physics and Chemistry of Solids, vol. 64, 1855, 2003.
- [38] A. H. Jahagirdar, N. G. Dhere, S. S. Kulkarni, A. A. Kadam, J. S. Shirolikar, H. Moutinho and B. To, "Preparation and Properties of CIGS and CIGSeS Thin Films using DESe as a Selenium Source and H₂S as Sulfur Source", Photovoltaic Specialists Conference, Conference Record of the 31st IEEE, 414, 2005.
- [39] A. Kadam, "Preparation of Efficient CIGSS/CdS Thin-Film Solar Cells by Optimizing the Mo Back Contact and using Diethylselenide as Selenium Precursor", Ph.D. thesis, University of Central Florida, 2006.
- [40] A. Jahagirdar, "Solar Driven Photoelectrochemical Water Splitting for Hydrogen Generation using Multiple Bandgap Tandem Of CIGS₂ PV Cells and Thin Film Photocatalyst", Ph.D. thesis, University of Central Florida, 2005.
- [41] H.W. Schock and U.Rau, "The role of structural properties and defects for the performance of Cu-chalcopyrite-based thin-film solar cells" Physica B, 308-310, 1081, 2001
- [42] B. J. Stanbery, "Copper Indium Selenides and Related Materials for Photovoltaic Devices" Critical Reviews in Solid State and Materials Sciences, vol. 27(2), 73, 2002.

- [43] D. K. Suri, K. C. Nagpal and G. K. Chadha, "X-ray Study of $\text{CuGa}_x\text{In}_{1-x}\text{Se}_2$ Solid Solutions", *Journal of Applied Crystallography*, vol. 22, 578, 1989, (JCPDS 40-1487).
- [44] F. B. Dejene and V. Alberts, "Structural and Optical Properties of Homogeneous $\text{Cu}(\text{In,Ga})\text{Se}_2$ Thin Films Prepared by Thermal Reaction of $\text{InSe}/\text{Cu}/\text{GaSe}$ Alloys with Elemental Se Vapour", *Journal of Physics D: Applied Physics*, vol. 38, 22, 2005.
- [45] T. Haalboom, T. Gödecke, F. Ernst, M. Ruhle, R. Herberholz, H.W. Schock, C. Beilharz and K.W. Benz, "Phase Relation and Microstructure in Bulk Materials and Thin Films of the Ternary System Cu-In-Se ", *Proceedings of the 11th International Conference on Ternary and Multinary compounds, ICTMC-11, University of Salford*, 249, 1997.
- [46] D. Schmid, M. Ruckh, F. Grunwald and H.W. Schock, "Chalcopyrite/defect Chalcopyrite Heterojunctions on the Basis of CuInSe_2 ", *Journal of Applied Physics*, vol. 73(6), 2902, 1993.
- [47] A. Niemegeers, M. Burgelman, R. Herberholz, U. Rau, D. Hariskos and H.-W. Schock, "Model for Electronic Transport in $\text{Cu}(\text{In,Ga})\text{Se}_2$ Solar Cells", *Progress in Photovoltaics: Research and Applications*, vol. 6(6), 407, 1998.
- [48] U.Rau, "Role of defects and defect metastabilities for the performance and stability of $\text{Cu}(\text{In,Ga})\text{Se}_2$ based solar cells" *Proceedings of the 12th International Conference on Ternary and Multinary compounds, ICTMC-12, Japanese Journal of Applied Physics*, Vol 39, 389, 2000.
- [49] S.H. Wei, S.B. Zhang and A. Zunger, "Effects of Ga Addition to CuInSe_2 on its Electronic, Structural, and Defect Properties", *Applied Physics Letters*, vol. 72, 3199, 1998.

- [50] P. Migliorato, J.L. Shay, H.M. Kasper and S. Wagner, “Analysis of the Electrical and Luminescent Properties of CuInSe₂”, Journal of Applied Physics, vol. 46, 1777, 1975
- [51] R. Noufi, R. Axton, C. Herrington and S.K. Deb, “Electronic Properties Versus Composition of Thin Films of CuInSe₂”, Applied Physics Letter, vol. 45, 668, 1984.
- [52] R. W. Birkmire and E. Eser, “Polycrystalline Thin Film Solar Cells: Present Status and Future Potential”, Annual Review of Material Science, vol. 27, 625, 1997.
- [53] R.G. Dhere and N.G. Dhere, “Polycrystalline Thin Film Solar Cells-Tutorial” 4th World Conference on Photovoltaic Energy Conversion, WCPEC 4, Hawaii 2006
- [54] C. Persson, A. Zunger, “Compositionally induced valence-band offset at the grain boundary of polycrystalline chalcopyrites creates a hole barrier” Applied Physics Letters, 87, 211904, 2005
- [55] T.Markvart and L. Castaner, “Solar Cells: Materials, Manufacture and Operation” Elsevier Advanced Technology, 2005
- [56] M.I. Alonso, M. Garriga, C.A. Durante Rinçon, E.Hernandez and M. León, “Optical Functions of Chalcopyrite CuGa_xIn_{1-x}Se₂ Alloys”, Applied Physics A: Materials Science & Processing, vol. 74, 659, 2002.
- [57] M. Bär, W. Bohne, J. Röhrich, E. Strub, S. Lindner, M. C. Lux-Steiner, Ch.H. Fischer, T. P. Niesen and F. Karg, “Determination of the band gap depth profile of the pentenary Cu(In_{1-x}Ga_x)(S_ySe_(1-y))₂ chalcopyrite from its composition gradient”, Journal of Applied Physics, 96, 7, 3857, 2004

- [58] T. Dullweber, O. Lundberg, J. Malmstrom, M. Bodegard, L. Stolt, U. Rau, H.W. Schock and J.H. Werner, "Back Surface Band Gap Gradings in Cu(In,Ga)Se₂ Solar Cells", *Thin Solid Films*, vol. 387 (1-2), 11, 2001.
- [59] D. Schroeder and A. Rockett, "Electronic Effects of Sodium in Epitaxial CuIn_{1-x}Ga_xSe₂", *Journal of Applied Physics*, vol. 82, 4982, 1997.
- [60] R. Klenk, U. Blieske, V. Dieterle, K. Ellmer, S. Fiechter, I. Hengel, A. Jiger-Waldau, T. Kampschulte, Ch. Kaufmann, J. Klaer, M.Ch. Lux-Steiner, D. Braunger, D. Hariskos, M. Ruckh and H.W. Schock, "Properties of CuInS₂ Thin Films Grown By a Two-Step Process Without H₂S", *Solar Energy Materials and Solar Cells*, vol. 49, 349, 1997.
- [61] T. Nakada, H. Ohno, T. Watanabe, H. Nakazawa, M. Matsui, and A. Kunioka, "Improved Cu(In,Ga)(S,Se)₂ Thin Film Solar Cells By Surface Sulfurization", *Solar Energy Materials and Solar Cells*, vol. 49, 285, 1997.
- [62] M.A. Contreras, B. Egaas, P. Dippo, J. Webb, J. Granata, K. Ramnathan, S. Asher, A. Swartzlander and R. Noufi, "On the Role of Na and Modifications to Cu(In,Ga)Se₂ Absorber Materials Using Thin-MF (M=Na, K, Cs) Precursor Layers", conference proceedings of 26th IEEE Photovoltaic Specialists Conference, Anaheim, IEEE Press, Piscataway, 359, 1997a.
- [63] D. Braunger, S. Zweigart and S.W. Schock, "The Influence of Na and Ga on the Incorporation of the Chalcogen in Polycrystalline Cu(In,Ga)(S,Se)₂ Thin-Films for Photovoltaic Applications", 2nd World Conference of Photovoltaic Solar Energy Conversion, Vienna, 1113, 1998b.

- [64] S.H. Wei, S.B. Zhang and A. Zunger, "Effects of Na on the Electrical and Structural Properties of CuInSe₂", Journal of Applied Physics, vol. 85, 7214, 1999.
- [65] D. Braunger, D. Hariskos and S.W. Schock, "Polycrystalline Cu(In,Ga)Se₂ Solar Cells", 2nd World Conference of Photovoltaic Solar Energy Conversion, Vienna, 511, 1998a.
- [66] D. Rudmann, G. Bilger, M. Kaelin, F.-J. Haug, H. Zogg, A.N. Tiwari, "Effects of NaF coevaporation on structural properties of Cu(In,Ga)Se₂ thin films" Thin Solid Films 431-432, 37, 2003.
- [67] K. L Chopra and S. R. Das, Ch # 6 "Properties of Thin Films for Solar Cells", Thin Film Solar Cell, Plenum press – New York, Edition, 295, 1983.
- [68] D. Haneman, "Properties and Applications of Copper Indium Diselenide", Critical Reviews in Solid State and Materials Sciences, vol. 14, 377, 1988.
- [69] I. Kaur, D. Pandya and K. Chopra, "Growth Kinetics and Polymorphism of Chemically Deposited CdS Films", Journal of Electrochemical Society, vol. 127, 943, 1980.
- [70] K. Djessas, G. Massé, and M. Ibannaim, "CuInS₂ Thin Films for Solar Cell Applications", Journal of Electrochemical Society, vol. 147, 1235, 2000.
- [71] D.Schmid, M Ruckh, and H. W.Schock, "A Comprehensive Characterization of the Interfaces in Mo/CIS/CdS/ZnO Solar Cell Structures", Solar Energy Materials and Solar cells, vol. 41/42, 281, 1996.

- [72] M.A. Contreras, M.J. Romero, B. To, F. Hasoon, R. Noufi, S. Ward and K. Ramanathan, "Optimization of CBD CdS process in high-efficiency Cu(In,Ga)Se₂-based solar cells", *Thin Solid Films*, vol. 403, 204, 2002.
- [73] S. Ishizuka, K. Sakurai, A. Yamada, K. Matsubara, P. Fons, K. Iwata, S. Nakamura, Y. Kimura, T. Baba, H. Nakanishi, T. Kojima and S. Niki, "Fabrication of Wide-gap Cu(In_{1-x}Ga_x)Se₂ Thin Film Solar Cells: A Study on the Correlation of Cell Performance with Highly Resistive i-ZnO Layer Thickness", *Solar Energy Materials and Solar Cells*, vol. 87, 541, 2005.
- [74] Y. Hagiwara, T. Nakada and A. Kunioka, "Improved J_{sc} in CIGS Thin Film Solar Cells Using a Transparent Conducting ZnO:B Window Layer", *Solar Energy Materials and Solar Cells*, vol. 67, 267, 2001.
- [75] B. Sang, K. Kushiya, D. Okumura and O. Yamase, "Performance Improvement of CIGS-Based Modules by Depositing High-quality Ga-doped ZnO Windows with Magnetron Sputtering", *Solar Energy Materials and Solar Cells*, vol. 67, 237, 2001.
- [76] J. Schoenes, K. Kanazawa, and E. Kay, "Band and Hopping Conduction in High-resistivity ZnO," *Journal of Applied Physics*, vol. 48(6), 2537, 1977.
- [77] G. Neumann, "On the Defect Structure of Zinc Doped Zinc Oxide," *Physica Status Solidi (b)*, vol. 105, 605, 1981.
- [78] T. Tsuji and M. Hirohashi, "Influence of Oxygen Partial Pressure on Transparency and Conductivity of RF Sputtered Al-doped ZnO Thin Films," *Applied Surface Science*, vol. 157, 47, 2000.

- [79] W. J. Jeong and G.C. Park, "Electrical and Optical Properties of ZnO Thin Film as a Function of Deposition Parameters," *Solar Energy Materials and Solar Cells*, vol. 65, 37, 2001.
- [80] T. Minami, H. Sato, T. Tomofuji, and S. Takata, "Conduction Mechanism of Highly Conductive and Transparent Zinc Oxide Thin Films Prepared by Magnetron Sputtering," *Journal of Crystal Growth*, vol. 117, 370, 1992.
- [81] *Rapid Thermal Processing*, Semiconductor International, 2003
- [82] J. Horzel, C. Allebe, J. Szlufcik, S. Sivothythaman, "Development of RTP for industrial solar cell processing" *Solar Energy Materials & Solar Cells* 72, 263, 2002
- [83] V. Probst, W. Stetter, J. Palm, S. Zweigart, M. Wendl, H. Vogt, K. Ufert, H. Calwer, B. Freienstein and F. Karg, "Large Area CIS Formation by Rapid Thermal Processing of Stacked Elemental Layers" 17th EPVSEC, Munich, Germany, 1005, 2001
- [84] K. Siemer, J. Klaer, I. Luck, J. Bruns, R. Klenk, D. Braunig "Efficient CuInS₂ solar cells from a rapid thermal process (RTP)" *Solar Energy Materials & Solar Cells* 67, 159, 2001
- [85] J.Palm, V.Probst, W.Stetter, R.Toelle, S.Visbeck, H.Calwer, T.Niesen, H.Vogt, O.Hernandez, M.Wendl, F. Karg, "CIGSSe thin film PV modules: from fundamental investigations to advanced performance and stability", *Thin Solid Films* 451 –452, 544 2004.
- [86] V. Probst, J. Palm, S. Visbeck, T. Niesen, R. Tolle, A. Lerchenberger, M. Wendl, H. Vogt, H. Calwer, W. Stetter, F. Karg, "New developments in Cu(In,Ga)(S, Se)₂ thin film modules formed by rapid thermal processing of stacked elemental layers", *Solar Energy Materials & Solar Cells* 90, 3115, 2006.

- [87] V. Probst, W. Stetter, W. Riedl, H. Vogt, M. Wendl, H. Calwer, S. Zweigart, K.-D. Ufert, B. Freienstein, H. Cerva, F. Karg, “Rapid CIS-process for high efficiency PV-modules: development towards large area processing”, *Thin Solid Films* 387, 262, 2001.
- [88] S. S. Kulkarni, J. S. Shirolkar, N. G. Dhere, “Preparation of CIGSS Thin-Film Solar Cells by Rapid Thermal Processing”, *Journal of Solar Energy Engineering*, Volume 129, August 2007, pages 323-326.
- [89] U. Rau, M. Schmitt, F. Engelhardt, O. Seifert, J. Parisi, W. Riedl, J. Rimmasch and F. Karg, “Impact of Na And S Incorporation on the Electronic Transport Mechanisms of Cu(In, Ga)Se₂ Solar Cells”, *Solid State Communications*, Vol. 107, No. 2, 59, 1998.
- [90] N.G. Dhere, “Present status and future prospects of CIGSS thin film solar cells”, *Solar Energy Materials & Solar Cells*, 90, 2006, pages 2181-2190
- [91] Institute of Energy Conversion (IEC) August 2005 monthly report to NREL, subcontract number ADJ-1-30630-12
- [92] V. Alberts and F. Dejene, “Material properties of CuIn(Se, S)₂ thin films prepared by the thermal diffusion of sulfur into CuInSe₂”, *Journal of Physics D: Applied Physics*, 35, pages 2021–2025, 2002
- [93] V. Alberts, J. Titus, R. Birkmire, “Material and device properties of single-phase Cu(In,Ga)(Se,S)₂ alloys prepared by selenization/sulfurization of metallic alloys” *Thin Solid Films* 451–452 (2004) 207–211
- [94] V. Alberts, “A comparison of the material and device properties of homogeneous and compositional-graded Cu(In,Ga)(Se,S)₂ chalcopyrite thin films” *Semiconductor Science and Technology*, 22 (2007) 585–592

- [95] B. M. Basol, A. Halani, C. Leidholm, G. Norsworthy, V. K. Kapur, A. Swartzlander and R. Matson, "Studies on Sulfur Diffusion into Cu(In,Ga)Se₂ Thin Films" Progress in Photovoltaics: Research and Applications, 2000; 8, 227-235.
- [96] S. S. Kulkarni, G. T Koishiyev and N. G. Dhere, "Preparation and characterization of CuIn_{1-x}Ga_xSe_{2-y}S_y thin film solar cells by rapid thermal processing", Thin Solid Films, In press, accepted manuscript, 2008.
- [97] P. Jackson, R. Wurz, U. Rau, J. Mattheis, M. Kurth, T. Schlotzer, G. Bilger and J. Werner, "High Quality Baseline for High Efficiency Cu(In_{1-x},Ga_x)Se₂ solar cells", Prog. Photovolt. Res. Appl.15:507–519, 2007.
- [98] S. S. Kulkarni and N. G. Dhere "Performance analysis of CuIn_{1-x}Ga_xSe_{2-y}S_y (CIGSeS) Thin Film Solar Cells Based on Semiconductor Properties" 18th International Photovoltaic Science and Engineering Conference and Exhibition, Kolkata, India, January 2009
- [99] N.G. Dhere, A.A. Kadam, A.H. Jahagirdar, S.S. Kulkarni, L. Weinhardt, D. Groß, C. Heske, and E. Umbach, "Spectroscopic analysis of CIGS₂/CdS thin film solar cell heterojunctions on stainless steel foil", Journal of Physics and Chemistry of Solids, 66, 2005, pages 1872-1875.
- [100] L. Weinhardt, O. Fuchs, D. Groß, G. Storch, E. Umbach, N.G. Dhere, A.A. Kadam, S.S. Kulkarni, and C. Heske, "Band alignment at the CdS/Cu(In,Ga)S₂ interface in thin film solar cells", Applied Physics Letters, 86, 2005, pages 062109-1 to 062109-3.